JAERI-Review
2001-005

PROGRESS REPORT ON NEUTRON SCATTERING RESEARCH
(APRIL 1, 1999 - MARCH 31, 2000)

March 2001

(Eds.) Satoru FUJIWARA, Kazuya AIZAWA and Susumu KATANO

日本原子力研究所
Japan Atomic Energy Research Institute

編集兼発行　　日本原子力研究所

JAERI-Review 2001-005

Progress Report on Neutron Scattering Research
(April 1, 1999 - March 31, 2000)

(Eds.) Satoru FUJIWARA, Kazuya AIZAWA and Susumu KATANO

Advanced Science Research Center
(Tokai site)
Japan Atomic Energy Research Institute
Tokai-mura, Naka-gun, Ibaraki-ken

(Received January 31, 2001)

This issue summarizes research progress in neutron scattering at Japan Atomic Energy Research Institute (JAERI) by utilizing the research reactor (JRR-3M) during the period between April 1, 1999 and March 31, 2000.

Keywords : Neutron Scattering, JRR-3M

JAERI-Review 2001-005

中性子散乱研究成果報告集
(1999年度次報告)

日本原子力研究所先端基礎研究センター
(編) 藤原　悟・相澤　一也・片野　進

(2001年 1月 31日 受理)

本報告書は、日本原子力研究所の先端基礎研究センターに所属する中性子散乱研究グループの研究を中心に、改３号炉（JRR-3M）を利用した所内の中性子散乱研究、所外との協力研究および共同研究の１９９９年４月～２０００年３月の期間における成果をまとめたものである。

Contents

This is a blank page.

Members of Neutron Scattering Groups in JAERI

This is a blank page.

List of JAERI Instruments

A. Neutron Scattering Instruments

Beam Port	Instrument	Moderator	Instrument Staff
1G	High Resolution Powder Diffractometer (HRPD)	Thermal(H_2O)	Yoshinobu Ishii, Yukio Morii, Yutaka Shimojo
1G-A	Diffratometer for Biological Crystallography-III (BIX-III)	Thermal(H_2O)	Ichiro Tanaka, Nobuo Niimura
2G	Triple-Axis Spectrometer (TAS-1)	Thermal(H_2O)	Toyotaka Osakabe, Susumu Katano
3G	Apparatus for Precise Neutron Optics and Neutron Diffraction Topography (PNO)	Thermal(H_2O)	Hiroshi Tomimitsu, Kazuya Aizawa
T2-1	Diffractometer for the residual stress analysis (RESA)	Thermal(H_2O)	Nobuaki Minakawa
T2-3	Diffractometer for Biological Crystallography-II (BIX-II)	Thermal(H_2O)	Satoru Fujiwara, Nobuo Niimura
T2-4	Triple-Axis Spectrometer (TAS-2)	Thermal(H_2O)	Masaaki Matsuda
C2-1	Low energy Triple-Axis Spectrometer (LTAS)	Cold(Liquid H_2)	Naoto Metoki, Yoshihiro Koike
C3-2	Small-Angle Neutron Scattering Instrument (SANS-J)	Cold(Liquid H_2)	Jun-ichi Suzuki, Satoshi Koizumi

B. Special Accessories

B-1. Cryostats, Magnets and Furnaces

Accessory	Number	Performance	Instrument Staff
Dilution Refrigerator	1	T_{min}= 10mK,H_{max} = 5T (Vertical)	N. Metoki, Y. Koike
Dilution Refrigerator (Liquid-^{4}He-Free)	2	T_{min}= 50mK	Y. Koike, Y. Morii
10T Magnet (Liquid^{4}He-Free)	1	T_{min}= 100mK,H_{max} 10T (Vertical)	S. Katano
^{3}HeCryostat	1	T_{min}= 0.3K,H_{max}6T (Vertical)	N. Metoki
Orange Cryostat	1	T_{min} = 1.5K	T. Osakabe
Horizontal Magnet	1	T_{min} = 1.5K,H_{max}=5T (Horizontal)	J. Suzuki
4K Cryostat	2	T_{min} = 4K	Y. Shimojo
10K Cryostat	6	T_{min} = 10K	Y. Shimojo
Furnace for Soft Matter	1	T = 0 – 300℃	S. Koizumi
Furnace	2	T_{max} = 1100K	Y. Shimojo
Furnace	1	T_{max} = 1600K	Y. Ishii

B-2. Pressure Devices

McWhan Cell	3	P_{max} = 2.5GPa	T. Osakabe
Sapphire Anvil Cell (under development)	several	P_{max} = 5GPa	T. Osakabe
Oscillatory Shear Machine	1	T=RT – 200℃, Amplitude = 0.01 - 2mm, Frequency = 0.1 - 100Hz	S. Koizumi
Tension Testing Machine	1	Tensil Speed= 0 - 0.01mm/sec, Range of Load= 50 - 1000kgf±1%	N. Minakawa

B-3. Detectors

Neutron Imaging Plate	several	Resolution = 100 μm	N. Minakawa

1. Research Activities in JFY 1999 and Recent Trends of Neutron Scattering at JAERI

1. JRR-3M and Neutron Scattering Instruments

In Japanese fiscal year (JFY) 1997, JRR-3M was operated at 30 MW thermal power for 186 days, and provided thermal and cold neutrons for the neutron scattering research. Nine neutron scattering instruments were used very efficiently for the study of solid state physics, chemistry and polymer science, biology, materials science, industrial applications and other sciences. As shown in Table 1, there was almost no beam loss at the nine instruments with the exceptions of 9 days at HRPD, 3 days at TAS-1 and 8 days at SANS-J. No major modifications were made at the nine instruments in this fiscal year.

2. Research group and research category at JAERI

Advanced Science Research Center (ASRC) of JAERI has four research groups for neutron scattering, namely, for the research on strongly correlated electron systems conducted by Y. Yamada, ultralow temperatures by Y. Morii, quantum condensed matter by M. Tachiki and structural biology by N. Niimura. In the four groups seventeen staff members and eleven postdoc members were assigned in JFY 1999. Besides the four groups, JRR-3M was used by the other JAERI members of the other departments, namely, Department of Research Reactor, Center for Neutron Science, Department of Materials Science, Synchrotron Radiation Research Center and Department of Fusion Engineering Research.

To pursue the JAERI research projects, fifty nine experimental proposals were submitted and carried out at JRR-3M. The utilized machine time for the projects is shown in the row of JAERI project of Table 1.

In addition to the JAERI projects and instrument maintenance, machine time was awarded to three funded seed research projects, seven cooperative research projects with national laboratory and private enterprises, and twenty four cooperative research projects with

Table 1. Machine time distribution of JAERI instruments in JFY 1999

	BIX-3	BIX-2	HRPD	PNO	TAS-1	TAS-2	LTAS	SANS-J	RESA
JAERI Project	154	185	103	144	112	121	129	103	114
Instrument maintenance	22	1	15	0	8	11	6	18	22
Funded seed research	0	0	0	0	0	10	0	4	0
Collaboration with National Lab. and Industry	0	0	0	0	10	0	10	27	19
Collaboration with University	10	0	59	42	53	44	41	26	31
Total utilization days	186	186	177	186	183	186	186	178	186
JRR-3M operation days	186	186	186	186	186	186	186	186	186
Operation efficiency	100%	100%	95%	100%	98%	100%	100%	96%	100%

ıote: Unit of the number is day unless otherwise specified.

university, which are also listed in Table 1. These researches are based on an open proposal system. In the Appendix B and C of this progress report listed are the themes in the cooperative research projects in JFY 1999 which were authorized by the Program Committee for Neutron Beam Utilization of the Advisory Council for JAERI's Research Facilities. (Appendix A)

3. Research on strongly correlated electron systems in JFY 1999

In the research for neutron scattering on strongly correlated electron systems, magnetism of novel materials was studied. An oxide high-T_c superconductor $La_{2-x}Sr_xCuO_4$ at around x=0.12 showed a peculiar coexistent state of the superconductivity and the antiferromagnetism (M. Sato et al. 2.3.4). Under the magnetic field of 10 T the intensity of the antiferromagnetic peak increased as much as 25 % of that of 0 T at 4 K. This indicated that spin fluctuations in the superconducting state were strongly suppressed by the magnetic field (M. Sato et al. 2.3.3). The metamagnetic state of a heavy fermion system $CeRu_2Si_2$ was also studied under high magnetic fields. At around 7.7 T, where the metamagnetism appears, a significant enhancement of ferromagnetic fluctuations was observed for the first time (M. Sato et al. 2.3.2). On the colossal magnetoresistance materials, $La_{1-x}Sr_xMnO_3$, $Pr_{1-x}Ca_xMnO_3$ and Sr_2MoFeO_6, large ferromagnetic fluctuations were observed by small-angle scattering experiments (M. Watahiki et al. 2.3.11). The response of these magnetic fluctuations under magnetic fields can be an origin of the unusually large magnetoresistance. A new high pressure cell using sapphire anvils was developed for neutron scattering experiments, and the maximum pressure of 6 GPa was achieved. Using this pressure cell, complex magnetic phase transitions were clarified under high pressures (T. Osakabe et al. 2.4.1, 2.4.2).

4. Research on ultralow temperatures in JFY 1999

In the research for neutron scattering at ultralow temperatures, an automatic cooling of the liquid-helium-free dilution refrigerator named "mK cryocooler" was developed and an easy access to neutron scattering experiments at mK temperatures became available. To eliminate mechanical vibrations of the 4K cryocooler which would be a source of heat leak to the dilution refrigerator, a prototype model of two-staged pulse tube refrigerator was made.

Applications of neutron scattering to the residual stress analysis were developed. Studies of residual stress of a jacket material, INCOLOY908, of ITER SC coil, a high pressure cell, welded materials and others were successfully carried out (Y. Tsuchiya et al. 2.6.3, A. Moriai et al. 2.6.14, and others). The apparatus for precise neutron optics, PNO, was used for interferometry experiments and very small-angle neutron scattering (H. Tomimitsu et al. 2.7.1, K. Aizawa et al. 2.8.2).

5. Research on quantum condensed matter in JFY 1999

In the studies on quantum condensed matter systems, we discovered a clear enhancement of in the weak antiferromagnetic ordering of the heavy fermion superconductor URu_2Si_2 under hydrostatic pressure (H. Amitsuka et al. 2.3.5). We found a strong jump in the size of the magnetic moment at the uranium site from 0.02 μ_B/U at ambient pressure up to 0.4 μ_B/U at the critical pressure 1 GPa. We also found a sudden disappearance of the magnetic excitation above the critical pressure. We have observed disappearance of the singlet-triplet magnetic excitation in the Haldane system under magnetic field above the critical field (Y. Koike et al. 2.3.1). We observed so called the resonance peak at 34 meV in the under-doped Bi2212 high-T_c compound with T_c = 70 K. High pressure neutron scattering experiments revealed that the weak itinerant magnetic ordering does not exist near quantum critical point of the Mott transition in V_2O_3.

6. Research on structural biology in JFY 1999

In the research group for hydration of functional biological macromolecules, the method of shielding of neutron imaging plate (NIP) from γ-rays has been developed and it became possible to use the NIP in the reactor site. A neutron diffractometer (BIX-3) with high resolution and high quality equipped with NIP dedicated to biological macromolecules has been successfully constructed by adapting the above method (I. Tanaka et al. 2.8.1). The BIX-3 has enabled that it takes two or three weeks to collect 1.5 Å resolution data from the typical proteins, which is a world record in the field of neutron structural biology. The 1.5 Å resolution data collection from a rubredoxin protein related to electron transfer and a myoglobin protein related to oxygen storage has been completed and their structure analyses have been started (K. Kurihara et al. 2.1.2, A. Ostermann et al. 2.1.1).

The 1st International Symposium on "Development of New Structural Biology Including Hydrogen and Hydration" in Organized Research Combination System was held from March 27 to 29, 2000.

7. Demand for Neutron Scattering Machine

The requested machine time for the JAERI's four research projects, seed research and two collaborative researches in JFY 1999 was 2,702 days for the nine instruments, which was 1.6 times bigger than the given machine time. The numbers are listed in Table 2 as well as those for the other thirteen instruments operated by universities. Table 2 also shows the trends of the demand for neutron scattering machine time for recent several years. Competition for beam time of JAERI machines varied between 1.5 and 1.7 except that in JFY 1998 which was caused by a long term shutdown of JRR-3M. While competition for beam time of university machines was higher by 0.2 at most, since there were so many users in universities. The overall competition for neutron beam at JRR-3M was between 1.7 and 1.9.

Figure 1 shows utilization of neutron beam instruments (The shaded column is for JAERI's neutron scattering, radiography and PGA, and the open column for university's neutron scattering.) at JRR-3M for the past ten years. In JFY 1999 JAERI instruments had utilization of 6,646 man-day, while university instruments had 10,427 man-day. It is clearly shown that the

Table 2. Demand for Neutron Scattering Machine Time at JRR-3M

	JFY1994			JFY1995			JFY1996			JFY1997			JFY1998			JFY1999			JFY2000		
	requested time(days)	given time (days)	ratio of r/g	requested time(days)	given time (days)	ratio of r/g	requested time(days)	given time (days)	ratio of r/g	requested time(days)	given time (days)	ratio of r/g	requested time(days)	given time (days)	ratio of r/g	requested time(days)	given time (days)	ratio of r/g	requested time(days)	planned time(days)	ratio of r/g
JAERI	1587	1050	1.5	1704	1032	1.7	1809	1068	1.7	2117	1362	1.6	2133	855	2.5	2702	1674	1.6	2324	1575	1.5
University	2929	1575	1.9	4051	2100	1.9	3479	1782	2	4147	2100*	2	3926	1235	3.2	4209	2418	1.7	4558	2275	2.0
Total	4516	2625	1.7	5755	3132	1.8	5288	2850	1.9	6264	3462*	1.8	6059	2090	2.9	6911	4092	1.7	6882	3850	1.8

total utilization of neutron beam increased from the level of 1,000 man-day at JRR-2 just before 1990 to 17,073 man-day at JRR-3M in 1999.

8. International collaborations

Under the US-Japan collaboration, several experiments were carried out using the new WAND detector which had been developed for several years, and clearly illustrated the superior performance of this unique detector. Among the experiments, the short-range polaron correlations in the ferromagnetic manganites and $La_{1-x}Ca_xMnO_3$, the polaron ordering in $Pr_{0.7}Ca_{0.3}MnO_3$, and the incommensurate charge ordering in $LuFe_2O_4$ were highlighted. Five JAERI researchers visited ORNL for 9 man-week totally.

The cooperative research program was also carried out between JAERI and BATAN, National Atomic Energy Agency of Indonesia. Two scientists and one engineer of BATAN stayed at JAERI for 4.5 man-month totally. Six researchers of JAERI made their visits to BATAN for 8.5 man-week totally.

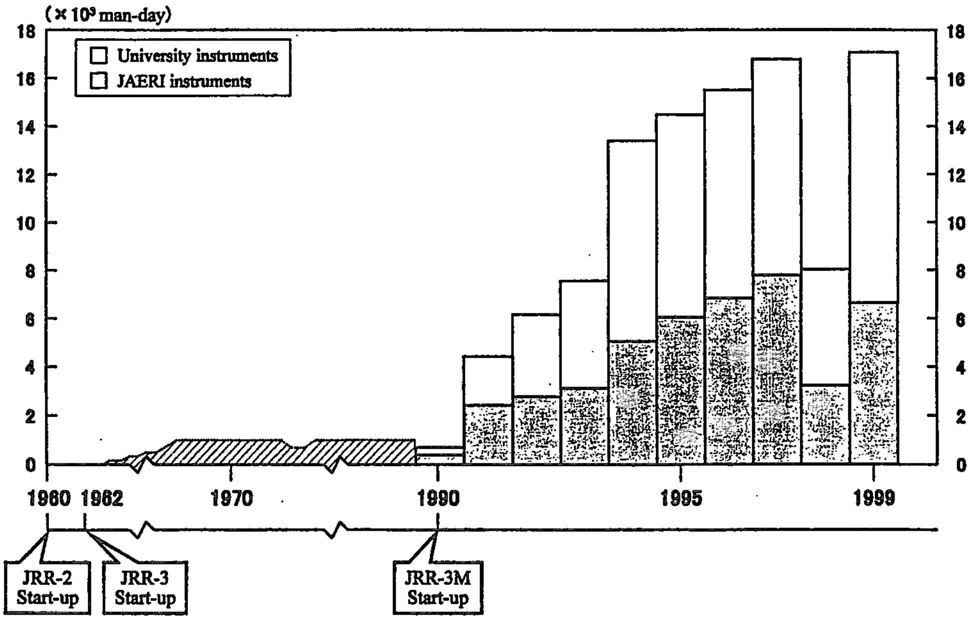

Fig. 1. Utilization of Neutron Beam Instruments at JRR-3M

2. Research Reports

2.1 Biology

2.1.1 A NEUTRON DIFFRACTION ANALYSIS OF MET-MYOGLOBIN AT 1.5Å

A. Ostermann[1], I. Tanaka[2], N. Niimura[2], F.G. Parak[1]

[1]Physik-Department E17, Technische Universität München, 85747 Garching, Germany
[2]Advanced Science Research Center, JAERI, Tokai, Ibaraki 319-1195, Japan

Hydrogen bonds are essential interactions for stabilizing the 3-dimensional structures of proteins and thus play an essential role for protein dynamics. So far, there exists only a small number of structures determined by neutron crystallography to high resolution with a satisfying completeness and redundancy. A high resolution and data completeness are needed because the number of free parameters in the crystallographic refinement is approximately twice as high as in a conventional X-ray structure determination due to the visibility of deuterium and hydrogen atoms. In this study we used the respiratory heme protein myoglobin from sperm whale. Myoglobin consists of 153 amino acids which form 8 α-helices. Myoglobin serves as a „model-protein“ in biophysics. It is investigated by many research groups with a wide range of physical and biochemical methods. Thus much complementary information is available. We determined the neutron structure of met-myoglobin up to 1.5Å resolution. The myoglobin crystal (2.5 x 2.5 x 1.0 mm^3) used in this study was soaked in deuterated mother liquor for years. The space group is $P2_1$ with the lattice constants a = 64.8Å, b = 31.1Å, c = 35.0Å and β = 105.8°. Neutron diffraction data were collected at room temperature at the neutron single crystal diffractometer BIX3 at the JAERI equipped with a neutron imaging plate.[1)] The following values refer to a resolution range from 10.0 – 1.5Å. The values in parentheses refer to the highest resolution shell (1.55-1.50Å). 88.6% (67.7%) of the possible reflections have been collected with an overall redundancy of 3.1 (2.3). The overall R_{merge} value of the data set is 10.2% (24.7%) with an overall $\langle I\rangle/\langle\sigma(I)\rangle$ of 6.9 (3.0). At the present refinement stage 62 of the exchangeable back bone hydrogen atoms (amid protons) were assigned as deuterium atoms. 9 exchangeable back bone hydrogen atoms were assigned as hydrogen atoms. Fig.1 shows an example for a strong deuterium position as well as for a strong hydrogen position in the back bone hydrogen bonds. Up to now 31 water molecules are included in the model whereas 13 of this water molecules show distinct deuterium positions. This high resolution data set provides the possibility to analyze hydrogen bridges as well as the extent of exchange of hydrogen atoms by deuterium within the protein. The obtained patterns can be interpreted in terms of different degrees of flexibility in the different parts of the protein structure.

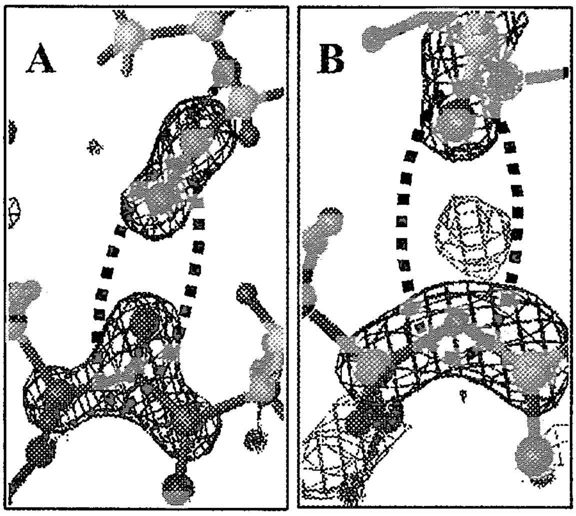

Fig.1 **(A)** Deuterium position in a back bone hydrogen bond. F_o-F_c-omit-map at $+3\sigma$ in black. Omitted atoms: C_α-N-C and D of amino acid #71 (C of #70) and carbonyl C and O of #67. **(B)** Hydrogen position in a back bone hydrogen bond. F_o-F_c-omit-map at $+3\sigma$ in black and -3σ in gray. Omitted atoms: C_α-N-C, H and the C_α-hydrogen of #76 (C of #75) and carbonyl C and O of #62. The dotted area marks the hydrogen bond atoms N-D···O and N-H···O.

References

[1] I. Tanaka, K. Kurihara, Y. Haga, Y. Minezaki, S. Fujiwara, S. Kumazawa, and N. Niimura, J. Phys. & Chem. Solids **60** (1999) 1623.

2.1.2 Neutron crystallography of rubredoxin.

K. Kurihara, I. Tanaka, M.W.W. Adams[a], N.Moiseeva[b], R. Bau[b], N. Niimura

Advanced Science Research Center, Japan Atomic Energy Research Institute, Tokai, Ibaraki 319-1195
[a] University of Georgia, Athens, GA 30602, USA
[b] University of Southern California, Los Angels, CA 90089, USA

A single-crystal diffractometer (BIX-3) dedicated to neutron protein crystallography has been successfully constructed at JRR-3M reactor of JAERI. This instrument features a new type of elastically-bent perfect-Si crystal (EBP-Si) monochromator and neutron imaging plates (NIP).

With this BIX-3 a single-crystal neutron diffraction analysis of the structure of small protein rubredoxin from the hyperthermophile *Pyrococcus furiosus* is currently under way. Rubredoxins are small protein containing an iron atom coordinated by sulfur atoms of four cysteine side chains. Although the physiological role for rubredoxins have not been definitively established, it is likely that they function as electron transfer proteins. Despite the uncertainty of its function in most species, rubredoxins from different organisms have been extensively studied by structural and spectroscopic methodologies, owing to their small size, stability, and ease of isolation.

Data are being collected at room temperature up to a resolution of 1.5 Å (so far the highest resolution neutron data set), using wavelength λ=2.35 Å. A single crystal of dimension 2 x 2 x 1 mm, grown via vapor diffusion from 3.6 M NaK phosphate, is being used in this project. Two sets of data from the same crystal, roughly corresponding to the crystal being mounted along the a and c axes, are being collected and merged. Data collection is by the step-scan method, with 0.3° intervals in φ and exposure times ranging from 60 to 75 minutes per frame. The completeness factor of the 1.5- Å resolution data set is currently at 78.2%. 301 hydrogen atoms and 49 deuterium atoms are included in the refinement of the structure of rubredoxin. 26 water molecules are also identified. In the present model R factor and R-free are 0.254 and 0.279, respectively.

Table 1 Data collection statistics.

Space group	$P2_12_12_1$ (Z=4)
Unit cell parameters	
a(Å)	34.3
b(Å)	35.3
c(Å)	44.2
Resolution	1.5 Å
Observed reflections	17,432
Unique reflections	7,297
Overall completeness	78.2 %

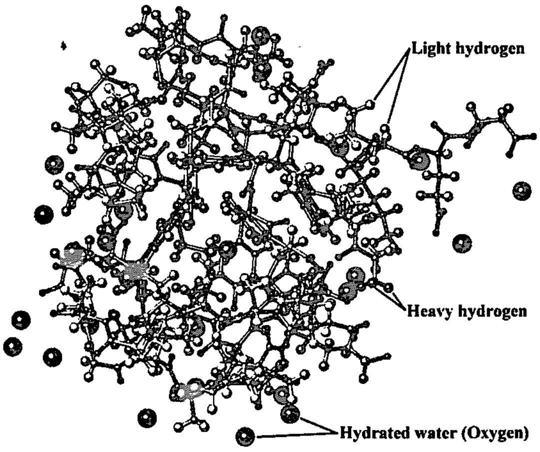

Figure 1 3-dimensional structure of rubredoxin determined by neutron diffraction.

2.1.3

Neutron Diffraction Measurements of Single Crystals of Hen Egg-White Lysozyme Grown under Different pH Conditions

S. Fujiwara, M. Maeda, Y. Yonezawa[1], and N. Niimura

Japan Atomic Energy Research Institute, Tokai, Ibaraki 319-1195, Japan
[1]Tsukuba College of Technology, Tsukuba, Ibaraki 305-0821, Japan

In various aspects of functions of proteins, hydrogen atoms play essential roles. Moreover, hydrogen bonds between the atoms in the protein as well as hydration are important in the stability of the protein. Locating the positions of hydrogens and hydrated water is therefore important in considering the molecular mechanism of the protein function and the stability of the proteins. Neutron crystallography, which can locate the hydrogens, is one of the important methods to investigate these problems. We have started a project which explore the protonation state of amino acid residues in the protein at various pH, since the charge distribution of the protein, which can be different in different pH, may have important effect on thermodynamic characterization of the protein. As a first step, we had been collecting the neutron diffraction data of the single crystal of hen egg-white (HEW) lysozyme grown in pH 4.9(1-2).

We finished collecting the data of the crystal under this condition in this fiscal year (1999). The space group of the crystals was $P4_32_12$, and the cell parameters were a=b=7.91 nm, c=3.66 nm. After data reduction by MAC-DENZO and SCALEPACK(3) was done, the obtained number of independent reflections ($I/\sigma>1$) was 5692, completeness of the data was 74.3% at 0.2 nm resolution, and the overall R_{merge} was 0.228. We have started structure analysis using X-plor(4). Figure 1 shows a density map around Lys33 obtained by the structure analysis. Although the analysis is preliminary, hydrated waters around the residue are clearly detected.

In parallel with the structure analysis, we have started collecting the data from the crystal grown in different pH. Crystals of HEW lysozyme were grown in D_2O at pH 3.4. The crystals with the same space group and the same cell parameters as those at pH 4.9 were obtained. Neutron diffraction patterns of the crystal have been measured with BIX-II(5). The oscillation method of 0.4 degrees has been employed. Exposure time per one frame has been 11 hours. Diffraction spots of at least 0.2 nm resolution have been observed. So far, the crystal has been rotated about 60 degrees.

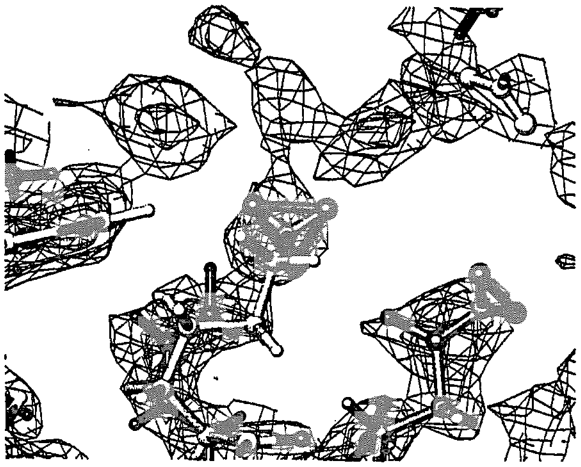

Figure 1. An example of the neutron density map of HEW lysozyme at pH 4.9

References

[1] S. Fujiwara et al.: JAERI Review **99-003** (1999) 13.
[2] S. Fujiwara et al.: JAERI Review **2000-005** (2000) 7.
[3] Z. Otwinowski and W. Minor: Methods Enzym. **276** (1997) 307-326
[4] A. T. Brünger: X-PLOR Version 3.1 (1993) (Yale Univ., New Haven, CT)
[5] S. Fujiwara et al.: Physica B **241-243** (1998) 207-209.

2.1.4

Neutron Diffraction Measurements of Live Frog Muscle Using the Contrast Variation Method

S. Fujiwara, Y. Takezawa[1], Y. Sugimoto[1], and K. Wakabayashi[1]

Japan Atomic Energy Research Institute, Tokai, Ibaraki 319-1195, Japan
[1]Grad. School of Engineering Science, Osaka University, Toyonaka, Osaka 560-8531, Japan

Neutron scattering/diffraction has a unique ability that information on the internal structure of a particle can be obtained with contrast variation measurements. This type of measurements is widely used in the area of solution scattering[1)]. This method is, however, not restricted to solution scattering, but applicable to all type of low-resolution measurements. Low-resolution neutron crystallography has been, for example, successfully applied to extract information on the detergent region in single crystals of membrane protein-detergent complexes[2)]. Here we applied this method to neutron fiber diffraction.

Sartorius muscle, dissected from a live frog, was perfused with Ringer's solution containing 115 mM NaCl, 2.5 mM KCl, 1.8 mM $CaCl_2$, 3 mM HEPES/NaOH (pH 7.2) in various D_2O concentrations (0%, 18.7%, 57.7%, 72.3%, and 92.9%). The neutron fiber diffraction patterns of these samples were measured with the Small-Angle Neutron Scattering Instrument (SANS-J) at the guide hall of the reactor JRR-3M in Japan Atomic Energy Research Institute. Neutrons with the wavelength of 0.653 nm ($\Delta\lambda/\lambda$=13.8%) were employed.

Figure 1 shows the neutron diffraction patterns of muscle in 92.9% D_2O and 0% D_2O (H_2O). In these measurements, the fiber axis of the muscles was set horizontally. Reflections on the equator and the meridian were clearly observed. The off-meridional myosin first layer line was also observed. Analysis of the contrast dependence of the scattering amplitudes of these reflections showed that there were reflections with the different contrast-matching points. This indicated that there was localization of the distribution of the scattering length density in the unit cell of the muscle. The detailed analysis using Fourier synthesis is in progress.

References

[1] L. A. Feigin and D. I. Svergun: Structure Analysis by Small-Angle X-Ray and Neutron Scattering (1987) Plenum Press, New York.

[2] E. Pebay-Peyroula et al.: Structure **3** (1995) 1051-1059.

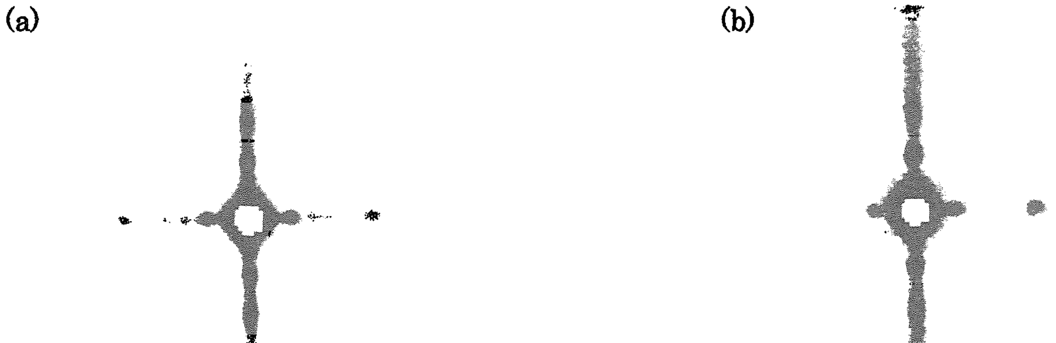

Figure 1. Neutron fiber diffraction patterns of the frog sartorius muscle (a) in D_2O, and (b) in H_2O.

2.1.5

Orientational behavior of biological super-macromolecules under high magnetic field

M. Hirai,[1] T. Hayakawa,[1] H. Iwase,[1] Y. Sano,[2] and J. Suzuki.[3]

[1] *Department of Physics, Gunma University, Maebashi 371, Japan.*
[2] *Department of Pharmacy, Setsunan University, Maikata 573-1010, Japan.*
[3] *Japan Atomic Energy Reseach Institute, Tokai, Ibaraki 319-1195, Japan.*

Introduction The behavior of a biological supermacromolecular suspension under magnetic field is a very attractive scientific concern from the viewpoint relating to cooperative phenomena in liquid crystal phase transition. Many theoretical works have been done to predict and explain the self-ordering mechanism of liquid crystals rod-shaped colloidal particles by assuming some repulsive or attractive interaction between them. Tobacco mosaic virus (TMV) is a rod-shaped virus that consists of coat protein subunits and RNA (180Å in diameter and 3000 Å in height). Previously, by using synchrotron radiation SAXS method we showed the presence of critical magnetic-field strength and the phase diagram of TMV liquid crystal depending on both magnetic-field strength (up to 1.8 tesla) and molecular concentration [1]. In the present study using SANS method we measured the phase behabior and the orientational processes of TMV under a hgih magnetic field strength.

Experimental The sample was TMV from Japanese common strain OM. The virus was suspended in 10 mM sodium phosphate buffer adjusted at pH 7.2, and the concentrations of the TMV suspensions were 25-176 mg/ml, respectively. SANS experiments were carried out by using a small-angle neutron scattering spectrometer called SANS-J at JRR-3M, Tokai, Japan. The wave length was 10 Å and the sample-to-detector distances were 10 m and 1.5 m. The exposure time for one time frame was 50 minutes. A helium-free super-conducting magnet HF10-100VT-20H-1 by SUMITOMO Heavy Ind.was used. The applied magnetic field strength was varied from 2.5 tesla to 10 tesla.

Results In the previous studies we found that the TMV suspensions under magnetic field of 1.8 tesla do not show an evidential orientational behavior at lower concentration below the isotropic-to-nematic lyotropic phase transition concentration of ~67 mg/ml. Fig. 1(a) and (b) show the 2-D scattering patterns of 25 mg/ml TMV isotropic phase suspensions under magnetic field of 0 tesla, and 10 tesla, respectively. The inserts show the 2-D contour maps of those scattering patterns. Fig. 1 (a) and (b) show a partial orientation of the long axis of TMV particle along the magnetic field. In comparison with the scattering pattern and contour map of 110 mg/ml TMV nematic phase suspension under magnetic field 10 tesla in Fig. 1 (c), the observed orientation of 25 mg/ml TMV suspension can be understood as a creation of small polynematic domains in isotropic phase induced by high-magnetic field. Further experiments and analyses are in progress.

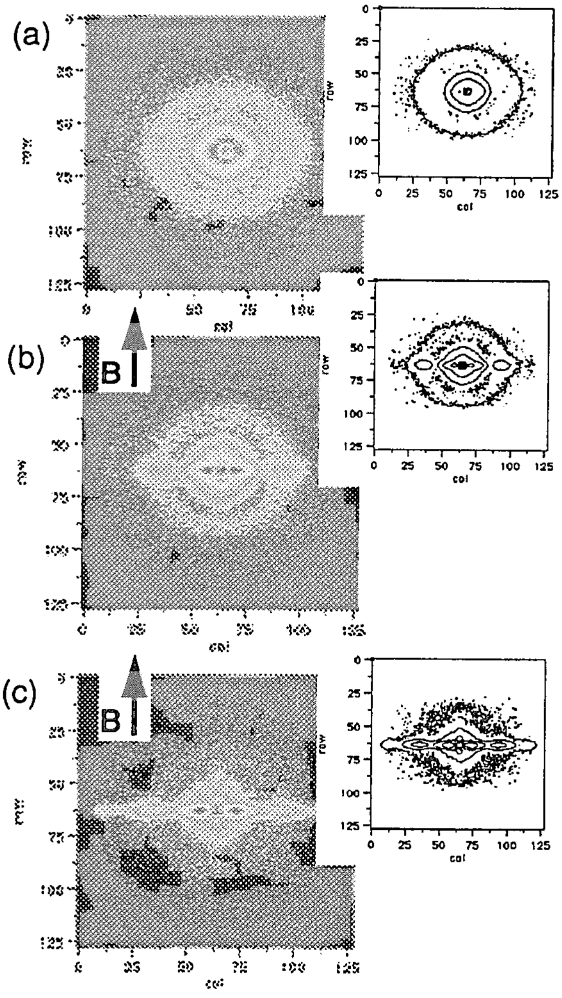

Fig. 1. 2-D scattering patterns and contour maps of TMV suspensions in log-scale. (a), 25 mg/ml, B = 0; (b), 25 mg/ml, B = 10 tesla; (c), 110 mg/ml, B = 10 tesla.

Reference
M. Hirai et. al., Phys. Rev. B, 1997, 3490.

2.1.6 Neutron scattering study on self-assembly of keratin molecules in water

Sachio Naito, Fumiyoshi Ikkai , Takeshi Karino[1], Michihiro Furusaka[1], Satoru Fujiwara[2], and Nobuo Niimura[2],

The Institute of Advanced Science Research, L'ORÉAL Tsukuba Center, Tsukuba, Ibaraki 300-2635, Japan
[1]High Energy Accelerator Research Organization, Tsukuba, Ibaraki 305-0801, Japan
[2] Japan Atomic Energy Research Institute, Ibaraki 319-11, Japan

The aim of this study is to clarify structural changes of proteins in apoptosis. Once apoptotic trigger is pulled in a hair cell, the cell begins to produce enormous amount of keratin proteins (Figure 1). Then, SS cross-linking is induced between the molecules and keratin proteins are finally gelated. This type of apoptosis is unusual in normal body but often occurs in cancer, AIDS, etc,. In this study, we have employed small-angle neutron scattering (SANS) and static light scattering (SLS) techniques for characterizing the early organization process of hair formation as a model of abnormal apoptosis.

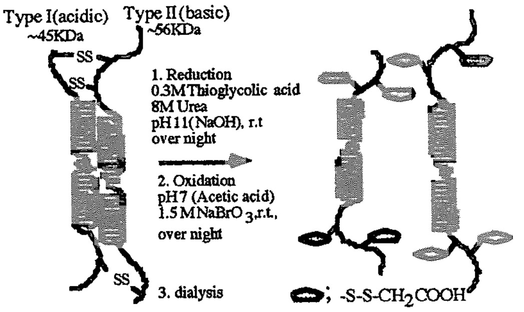

Figure 1. Structure of keratin (protofibril) and preparation of water soluble S-carbomymethyl alanyl disulfide keratin (CMADK).[1]

Protofibril consist of a pair of type I(acidic) and type II(basic). We have estimated the cross-sectional dimensions of CMADK in D_2O by wide-angle neutron scattering measurement (WINK). The radius of CMADK_{monome} and CMADK_{dimer} are estimated to be 9.6 Å for monomer and 20.4 Å for dimer, respectively. We confirmed the scattering profile corresponding to the $\mathrm{CMADK}_{\mathrm{dimer}}$ disappeared in 8 M urea solution. Figure 2 shows the least-squares fitting by Guinier equation (1) to the scaled SLS and SANS (by SANS-J, PSD located $L = 7$ m) data of 0.75 % CMADK in the buffer (pH 7) and pH11 D_2O in the q range 0.00068 – 0.0027 Å^{-1}.

$$I(q) = I(0)_{\mathrm{monomer}} \exp(-q^2 <Rg_{\mathrm{monomer}}>^{2/\beta}) + I(0)_{\mathrm{dimer}} \exp(-q^2 <Rg_{\mathrm{dimer}}>^{2/\beta}) \qquad (1)$$

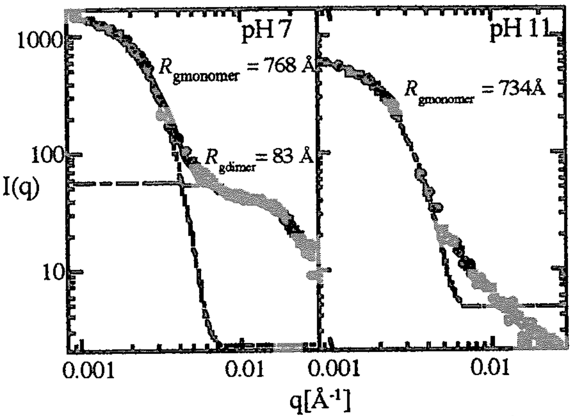

Figure 2. Least-squares fitting of eq (1) to the SANS and and scaled SLS $I(q)$ vs q curves.

The theoretical curve for scattering profile of whole CMADK particles reproduces well the experimental data. It is clearly shown two kinds of CMADK particles whose sizes are quite different disperse in the buffer (pH 7). In the q range 0.01 - 0.02 Å^{-1}, however, a shoulder profile observed on the scattering curve in the buffer (pH7) disappears in the pH 11 solution. We confirmed that about 40% of α-helical structure remained in CMADK even in the pH 11 solution. On the base of the CMADK molecular weight, $<R_{\mathrm{gmonomer}} = 768$ Å> is too large for a monomeric $\mathrm{CMADK}_{\mathrm{monomer}}$. It is suggested that two $\mathrm{CMADK}_{\mathrm{monomer}}$ molecules exist as a long rod-like complex by head (N-terminal)-to-tail (C-terminal) overlap mode. This like decomposition of $\mathrm{CMADK}_{\mathrm{dimer}}$ could be observed in 0.8 M urea solution. These results suggest that the $\mathrm{CMADK}_{\mathrm{dimer}}$ structure is stabilized by very weak inter-molecular hydrophobic interaction. Consequently, in the early organization process, type I and II keratin molecules recognizes each other, and self-assembles without SS cross-linking formation. Then, the assembly forms parallel or anti-parallel dimer but not coiled-coil.

Reference

[1] Y. Miyauchi, S. Naito, K. Kurita, and M. Furusaka, KENS Report-XI, 107 (1997).

2.1.7

Powder Neutron Diffraction Study of the Crystalline-State 3-1 Photoisomerization of the 3-Cyanopropyl Cobaloxime Complex

T. Ohhara, H. Uekusa, T. Ozeki, Y. Ohashi, K. Oikawa[1], Y. Morii[1]

Dept. of Chemistry and Materials Science, Tokyo Inst. of Tech., Meguro-ku, Tokyo 152-8551, Japan
[1]Japan Atomic Energy Research Institute, Tokai, Ibaraki 319-1195, Japan

In recently works[1-3], we showed that single crystal neutron diffraction became a powerful method to clarify the mechanism of crystalline-state reactions because the migration of deuterium atoms, which were introduced into the reactive part as markers, according to the crystalline-state reaction can be observed. However, a large single crystal (~2mm) is required for single crystal neutron diffraction. It is usually difficult to prepare such a large single crystal and to penetrate the light into the crystal. On the other hand, powder neutron diffraction can be carried out with small crystals, which is easier to prepare and penetrate the light. In this work, the migration of deuterium atoms according to the 3-1 photoisomerization of (3-cyanopropyl-$d_2^{\alpha,\alpha}$)[(*R*)-1-phenylethylamine-d_{11}]cobaloxime-d_{14} (*1* : Fig. 1) was studied by powder neutron diffraction.

In compound *1*, two deuterium atoms were introduced to the α-carbon of 3-cyanopropyl group as markers, and other deuterium atoms were in order to prevent the incoherent neutron scattering by hydrogen atoms. Two powder neutron diffraction measurements were carried out by HRPD at the 1G port of JRR-3M reactor. One was the compound *1* before irradiation (*1-ini*) and another was the *1* after 20 days exposure of visible light (*1-end*). The wavelength was 1.823Å, the temperature was 90K and the $2\theta_{max}$ was 162.5°.

The rietveld structure refinement was carried out for the *1-ini* with the initial model structure precedently determined by single crystal X-ray diffraction. The result of rietveld profile fitting is shown in Fig. 2. The positions of hydrogen and deuterium atoms in the obtained structure was consistent with the molecular structure of *1*, and there was no irregular bond lengths and angles. The structure of *1-end* is now under investigation.

References

[1] Y. Ohgo et al., Enantiomer **2** (1997) 241-248
[2] T. Ohhara et al., Chem. Lett. (1998) 365-366
[3] T. Ohhara et al., Acta. Cryst. B56 (2000) 245-253.

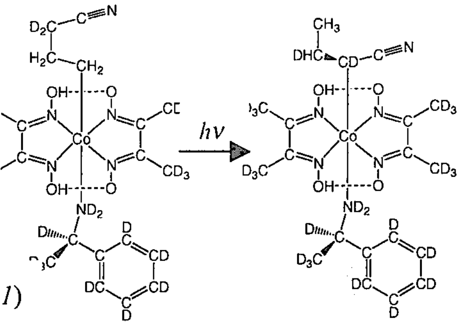

(*1*)

Fig. 1 Crystalline-state 3-1 photoisomerization of compound *1*.

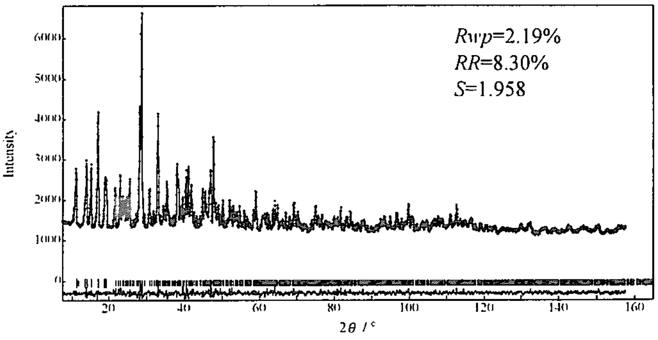

Fig.2 Result of the rietvled rifinement of *1-ini*.

2.2 Soft Matter

2.2.1 Development of Neutron Reflectometer for Air/Water Interface with Imaging Plate

H.Matsuoka, E.Mouri, R.Yoshitome, K.Kago, H.Yamaoka and K.Soyama[1]

Department of Polymer Chemistry, Kyoto University, Kyoto 606-8501, Japan
[1]Japan Atomic Energy Research Institute, Tokai, Ibaraki 319-1195, Japan

Reflectivity measurement is a powerful tool for the structural study of surfaces and interfaces in nanometer scale. X-ray and neutron reflectivity (XR, NR) measurements have been applied to solid surfaces and thin films on solid substrates, and significant information has been coming out. One of the recent hot topic in surface and interface science is the structure of monolayers on water surface. Such a system is quite important for novel functional devices and also biological point of view. The structure of monolayer has been investigated by XR, NR and atomic force microscope (AFM) *after* deposited on solid substrate in dried state. However, it has been found that the nanostructure of monolayer after deposition is largely different from that on water surface.1 The horizontal type XR and NR are the only the technique to investigate the monolayer structure on water directly.

In this study, we have developed the horizontal type NR instrument. In addition to 1D PSD, the imaging plate(IP) was also used as a detector. By IP, the off-specular reflection and in-plane information can be obtained in addition to depth-profile.

The C2-1 port (LTAS) in JRR-3M, Tokai was used. The have developed a new device to control the tilting angle of the monochrometer of LTAS. By this mechanism, the incident angle of neutron to water surface can be changed. For the water surface measurement, the specially designed Langmuir-Brodgett (LB) rough was constructed. By the position of the barrier of the LB trough, the surface pressure of the monolayer on water can be controlled.

Figure 1 shows the NR profile for pure water surface and DPPC (a kind of lipid) monolayer on water. The intensity of reflected neutron can be clearly detected as a function of incident/reflection angle (specular reflection). This is the first NR data for water surface in Japan. The detailed analysis is now in progress.

Figure 2 shows the IP image. The off-specular reflection is excellently observed. Modification and improvement of this NR apparatus is now going on.

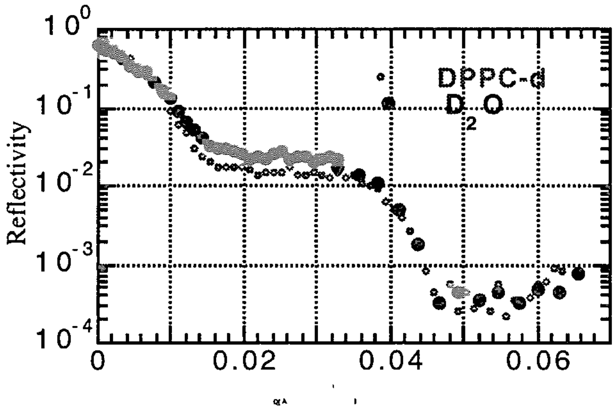

Figure 1 NR profiles for pure D_2O surface and DPPC monolayer on D_2O surface.

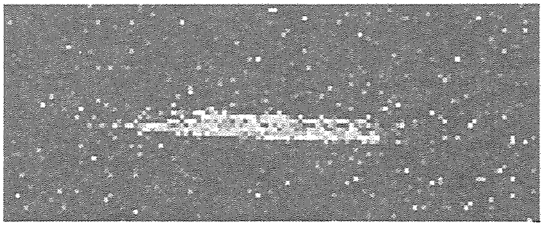

Figure 2 IP image of NR for D_2O surface. θ=0.24 degree.

2.2.2 Scattering Studies on Hierarchical Structures of Rubber/Filler Systems

T.Hashimoto, M.Takenaka, T.Koga[1], and K.Aizawa[2]

Department of Polymer Chemistry, Graduate School of Engineering,
Kyoto University, Kyoto, 606-8501-,Japan
[1]Hashimoto Polymer Phasing Project, Department of Polymer Chemistry,
Graduate School of Engineering,, Kyoto University, Kyoto, 606-8501-,Japan
[2]Japan Atomic Energy Research Institute, Tokai, Ibaraki 319-1195, Japan

The incorporation of fillers, such as carbon black or sillica particles, in rubber imporves the mechnical properties of the rubbers. The inprovement depends on the aggregation structures formed by prticles of the fillers in the rubbers. The aggregation structures is expected to have hierarchical structures so that we have to obsertve the wide range of length scale from 1 nm to 10 μm to explore the structure. In this study, we, thus aim to explore the hierarchical structures of the rubber/carbon black system by combining very small angle neutron scattering (VSANS), ultra small angle small x-ray scattering (USAXS), and small angle x-ray scattering (SAXS).

The rubber used in this study was polyisoprene (PI) and poly(styrene-r-butadiene) (SBR). Carbon black (CB) were used as the fillers. The weight fraction of the fillerss in each system is 0.2. VSANS was performed at PNO (3G) in JRR-3M, Tokai. USAXS, SAXS was performed at Hashimoto Polymer Phasing Project, Kyoto. Figure 1 shows VSANS, USAXS, and SAXS profiles of the PI/CB system. Each profile can be well superimposed so that we obtained the scattered intensity distribution over 4 decade in length scale. This superimposed profile indicates that the PI/CB system ahs the folowing hierarchical structure: (i) the carbon black particle with an averaged diameter 13 nm forms the elipsoidal primary aggregation structure where the length of minor axis and the axis raito are, respectively, 32 nm and 5.3. (ii) the primary aggregation structure forms the mass-fractal sturcture with its exponent being 2.1.

Though we do not show the profiles here, we obateind the well-superimposed VSANS, USAXS, and SAXS profiles for the SBR/CB system. Similar to the PI/CB system, SBR/CB system has the following hierarchical structure: (i) the carbon black forms the elipsoidal primary aggregation structure where the length of minor axis and the axis raito are, respectively, 28 nm and 2.8. (ii) the primary aggregation structure forms the mass-fractal sturcture with its exponent being 2.2 and the upper limit can be observed at q=0.001 nm^{-1}.

Acknowkedgment: We are grateful to the material research department , Yokohama Rubber Co., Ltd. for their help in perparing samples the experimental samples used in this work.

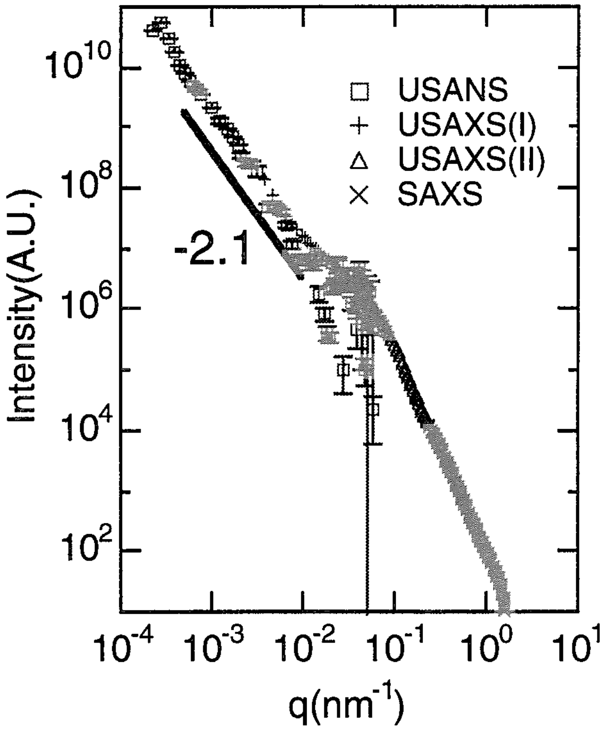

Fig.1 VSANS,USAXS, and SAXS Profiles of PI/CB system

2.2.3 PNO Study on Bovine Serum Albumin Gels 3

Y. IZUMI, Y.JINBO, T.MATSUGI, K.AIZAWA[1] AND H.TOMIMITSU[1]

Graduate School of Science and Engineering, Yamagata University, Yonezawa, Yamagata 992-8510
[1]Advanced Science Research Center, JAERI, Tokai, Ibaraki 319-1195

Globular protein gels have been extensively investigated over many years. Most of the studies concentrated on examining structural and rhelogical properties of fully cured gels. Protein gelation is known to be promoted by several kinds of treatments. Among them, gelation induced by temperature, the so-called heat-induced or thermally induced gelation, has received insufficient attention.

In previous reviews$^{1)}$, we reported the large scale structures of bovine serum albumin (BSA) gel revealed by Precise Neutron Optics (PNO) measurements. The previous results are summarized as follows. The transparent BSA gel (C_p, the concentration of BSA, 15wt% and no added salt) gave too very small excess intensity to detect, indicating a structure with a very small contrast or very small junction point. On the other hand, the opaque gels (C_p= 15wt% and C_s, the concentration of NaCl, 0.05, 0.1, 0.2 and 0.3mol NaCl) gave a clear difference between the intensity of the gel and that of the solvent. The excess intensity for the gel prepared at 0.05M NaCl indicated the exponent value of 4.0 as the fractal dimension. On the other hand, that for the gel prepared at $C_s \geqq 0.1$ indicated the exponent value of 3.0 as the fractral dimension. The crossover between these exponents indicates a change in the surface structure of the gels. The exponent value of 4.0 indicates the smooth surface of the junction zones, while the exponent value of 3.0 indicates a very rough surface. The crossover occurs at a concentration between 0.05M and 0.10M NaCl. Furthermore, the structures of the opaque gels, i.e., the size of the junction zone and the size distribution strongly depend on the gelation temperature. However, it is still unknown whether the exponent-value is continually changing or not at the crossover point.

In present work, we intended to reveal whether the surface structure was continually changing or not at the crossover point. The BSA gel of 20 wt% was prepared to obtain a higher contrast. The measurements have been carried out by PNO spectrometer. The details of measurements and the analysis are described elsewhere$^{2)}$. Four gels with different Cs (0, 0.05, 0.075 and 0.1M NaCl) were prepared by heating during 6min at 70℃.

The results gave very small excess intensities. As the changes of the surface structures of junction zones reflect in the rheological properties, further studies should be needed. As the gels accumulate the influences of many factors which cannot be controlled, it is very difficult to specify the main factor which determins the gel structures. However, the PNO technique is still useful to characterize the surface structure and the size of the junction zone of micron order in fully cured gels and also gels around a crossover point.

References

1) Y.Izumi, K.Soma, K.Aizawa, S.Koizumi, and H.Tomimitsu, JAERI-Rev. 99-003, p.27(1999); ibid., 2000-005, p15(2000).
2) K.Aizawa & H.Tomimitsu, Physica B 213&214(1995)884-886.

2.2.4

Characterization of Asphaltene Micelles and Their Interactions in Vacuum Residue of Crude Oil by Small-Angle Neutron Scattering

S. Kamei, K. Yogo, M. Ishikawa and J. Suzuki[1]

Mitsubishi Research Institute, Inc., 2-3-6 Otemachi Chiyoda-ku Tokyo 100-8141, Japan
[1]Japan Atomic Energy Research Institute, Tokai, Ibaraki 319-1195, Japan

Recently, the development of better refining technology of heavy oil is becoming more important in the field of oil industry, because available crude oils become heavier and more concentrated in sulfur and metals. Asphalten, which is the n-heptane insoluble fraction of petroleum, strongly affects the property of crude oil, though its content is slightly several % in weight.

Experimental study on the micellar structure of asphaltenes and their interaction in Arabian heavy vacuum residue was performed utilizing small-angle neutron scattering (SANS) techniques. Since asphaltenes are mainly composed of poly-condensed aromatics, they intend to form micelles in the heavy oils by interacting each other. It is, therefore, very important to clarify the precise micellar structure of asphalten for the oil industry.

Samples used were Arabian Heavy Vacuum Residue (AH-VR) and VR fractions of the hydrotreated oil from AH atmospheric residue. Asphaltene was prepared from VR with addition of n-heptane. Hydrotreatment was performed in a fixed bed continuos flow reactor system, in which hydrodemetallization (HDM) and hydrodesulfurization (HDS) catalysts were installed, respectively.

SANS was measured as a function of concentration (0.5%, 1.0%, 2.0%) and temperature (13C°, 100C°, 200C°, 250C°). d-toluene was used as a solvent. Fig.1 shows the q-I(q) plot of asphalten. R_G of AR-AH-VR, -HDM and HDS are shown in Table1, respectively. R_G of HDM and HDS were 2times larger than that of VR. This strongly suggests the existence of molecular association of asphalten micelles by hydrodemetallization.

Based on the more precise analysis of SANS, we found that the core of micelles had prelate structure with a 29Å, 7Å and 7Ådiameter and that the thickness of polar region was 8Å.

SANS is very powerful tool to understand the micellar structure of asphaltens.

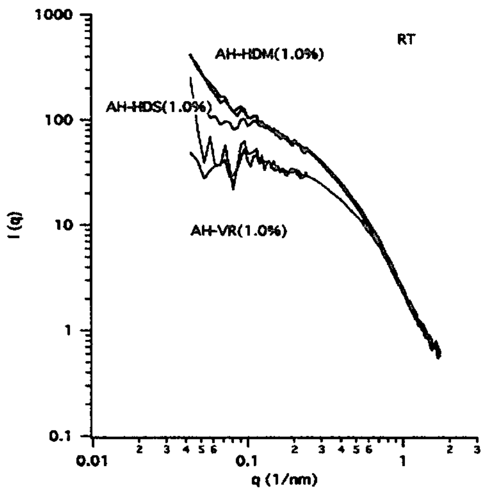

Fig.1 q-1(q) plot of Asphalten

Table1 R_G of Asphalten

	Concentration	R_G(nm)
AR-AH-VR	2.0%	3.728
	1.0%	3.730
	0.5%	3.666
AR-AH-HDM	2.0%	4.428
	1.0%	4.417
	0.5%	4.332
AR-AH-HDS	2.0%	4.494
	1.0%	4.513
	0.5%	4.468

Acknowledgement

We thank Prof. M. Frusaka of KEK and Y. Matsushita of Nagoya Univ. for useful discussion. The samples were provides by Petroleum Energy Center (PEC).

Reference

[1] M.Scarsella, D. Mastorofini, L. Barre, D. Espinat, and D. Fenistein, Energy and Fuels, **13** (1999) 739.
[2] D. A. Storm, E. Y. Sheu, Fuel, **74** (1995) 1140.

2.3 Storonly Correlated Electron Systems and Superconductivity

2.3.1 Neutron Scattering Study of Linear-Chain Haldane Compounds NDMAZ and NDMAP

Y. Koike[a,b], N. Metoki[a], Y. Matsuoka[a],T. Kobayashi[c], M. Yamashita[d]
a- Advanced Science Research Center, Atomic Energy Research Institute, Tokai, Naka, Ibaraki 319-1195, Japan
b- Japan Science and Technology Corporation, Kawaguchi, Saitama 332-0012, Japan
c- KYOKUGEN Osaka University, Toyonaka, Osaka 560-8531, Japan
d- Faculity of Science, Toyko Metroplitan University, Hachioji, Tokyo 192-0397, Japan

The low dimensional quantum spin gap systems attract much interest. Haldane conjectured that one-dimensional Heisenberg antiferromagnet (1D HAF) with an integer spin number has a spin singlet ground state with spin excitation gap (Haldane gap) [1]. Recently the field induced long range order has been reported in new Haldane compounds $Ni(C_5H_{14}N_2)_2N_3(ClO_4)$ (NDMAZ) [2] and $Ni(C_5H_{14}N_2)_2N_3(PF_6)$ (NDMAP) [3]. We carried out neutron scattering experiments in order to investigate the antiferromagnetic (AFM) order and spin excitaion for these new Haldane compounds.

Neutron scattering experiments were carried out using thermal neutron triple-axis spectrometers (TAS1, TAS2) and a cold neutron triple-axis spectrometer (LTAS). Low temperature and high field experiments were carried out by using a liquid-He-free dilution refrigerator and liquid-He-free 10 T split-pair magnet for neutron scattering.

In NDMAZ and NDMAP we observed clear Haldane gap at zero field. Figure 1 shows the constant-Q scan profiles for NDMAZ. Inelastic responses were observed at about 1.7 meV and 3.2 meV. From our systematic measurements we obtained the gap energies Δ_X = 1.61 meV, Δ_Y = 1.76 meV, Δ_Z = 3.2 meV, the intra-chain coupling J = 4.3 meV, and the anisotropy parameters D = 0.76 meV, E = 0.038 meV for NDMAZ. In NDMAP the gap energies were Δ_X = 0.48 meV and Δ_Y = 0.64 meV.

Figure 2 shows the field dependence of the constant-Q profile at Q = (0 0 0.5) for NDMAZ as applying the field parallel to the b-axis (perpendicular to the chain axis). The splitting of the 1.7 meV peak was observed in the magnetic field. The behaviors of these peaks were completely different. With increasing field, 1.6 meV peak shifted to low energy, while we observed no change of the high energy peak at about 1.76 meV. The lowest energy gap decreased to 0.87 meV at H = 10 T. The field dependence of the gaps is well explained by the fermionic field-theory treatment of the 1D HAF Hamiltonian [4] with obtained gap energies and g-value, 2.3.

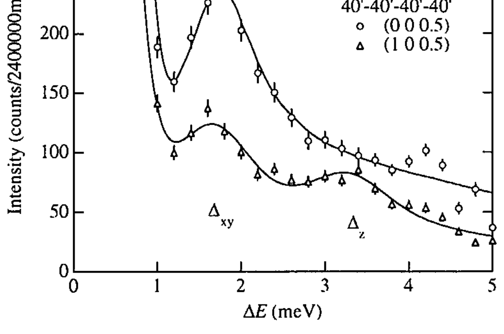

Fig. 1 Constant-Q profiles of NDMAZ measured at Q = (0 0 0.5) and (1 0 0.5).

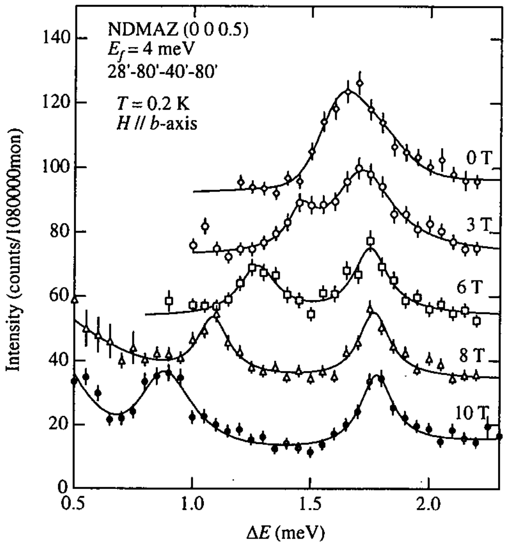

Fig. 2 The external field dependence of the constant-Q profiles at (0 0 0.5). Each profile is shifted by 20 counts in the ordinate.

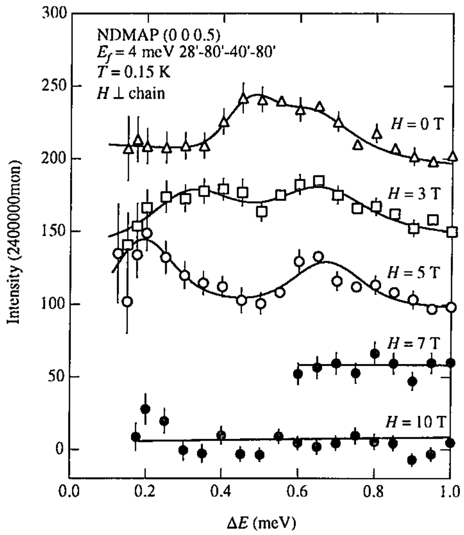

Fig. 3 Field dependence of the constant-Q profiles of NDMAP. Each profile is shifted by 50 counts.

Figure 3 shows the field dependence of the constant-Q profiles for NDMAP. The field was applied perpendicular to the chain direction. In Fig. 3 the data are plotted after the subtraction of the background measured at Q=(0 0 0.56) and T = 0.15 K in zero field. The inelastic signal observed at about 0.55 meV clearly splits into two peaks, and the low energy peak showed remarkable shift with applying field. At H = 5 T, the existence of the Haldane gap becomes unclear from the excitation profile, because the peak maximum would be smaller than 0.13 meV which is comparable to the resolution of our spectrometer. This result indicates that the Haldane gap is almost closed at this field. Above the critical field ~ 6 T, we found drastic change in the scattering profile. The low energy excitation and 0.64 meV peak became unobservably week. This change would be interpreted by the level crossing of this system.

We carried out the elastic neutron scatting experiments for NDMAP at H = 10 T and T = 0.2 K. However so far no trace of the magnetic Bragg peak has been observed around the antiferromagnetic scattering vector, (0 0 0.5), (0 0.5 0.5), (0 1 0.5), (1 0 0.5) beyond the statistical error about 10^{-4} of the (002) nuclear Bragg intensity. The most probable reason for the absence of the Bragg peak is the small magnetic moment induced by magnetic field. Another possibility is that the magnetic peak may appear the different wave vector because of the magnetic structure factor or incommensurate structure under magnetic field.

Further studies using deutrized sample are necessary to understand the nature of the Haldane system under magnetic field.

References

[1] F.D.M. Haldane, Phys. Lett A**93** (1983) 464.
[2] Z. Honda, K. Katsumata, H. Aruga Katori, K. Yamada, T. Ohishi, T. Manabe and M. Yamashita, J. Phys. Condens. Matter. **9** (1997) L83.
[3] Z. Honda, H. Asakawa and K. Katsumata, Phys. Rev. Lett. **81** (1998) 2566.
[4] I. Affleck, Phys. Rev. B**41** (1990) 6697, *ibid.* B**46** (1992) 9002.

2.3.2

Field Induced Ferromagnetic Spin Fluctuation in a Heavy Fermion Compound $CeRu_2Si_2$

M. Sato[A] Y. Koike[AB] S. Katano[A] N. Metoki[A] H. Kadowaki[C] S. Kawarazaki[D]

[A]ASRC, JAERI, Tokai 319-1195
[B]JST Corporation, Kawaguchi, Saitama 332-0012
[C]Department of Physics, Tokyo Metropolitan University, Hachioji, Tokyo 192-0397
[D]Department of Earth and Space Science, Osaka University, Toyonaka, Osaka 560-0043

$CeRu_2Si_2$ is a paramagnetic heavy fermion compound. In this compound, antiferromagnetic (AFM) correlations grow into three dynamical spin fluctuations below 60 K.[1,2] Applying field along its magnetic easy axis, the magnetization jumps up around 7.7 T (=H_m) below 10 K, which is called as the metamagnetic-like-behavior.[3] We investigated the change of the spin fluctuations around H_m by inelastic neutron scattering under high magnetic field. As the result, we have discovered that a ferromagnetic (FM) fluctuation develops around H_m.

In Fig.1 are shown the results of constant E-scans with energy transfer ΔE=0.4 meV along $[h,1,0]$ (in r.l.u.). These scans are carried out at T=0.45 K under H=0, 7.7 and 10 T. (110) is a Brillouin zone center. The peak at (0.7,1,0) under H=0 T corresponds to one of the AFM fluctuations. As applying field, this peak disappears, which is consistent with the previous studies.[4] In addition, the intensity around the zone center grows up at 7.7 T. In Fig.2 is shown the field dependence of the scattering intensity with ΔE=0.4 meV at (0.9,1,0) (T=0.45 K). This point is located near the zone center. As can be seen in this figure, the intensity peaks around H_m. This result indicates that the metamagnetic behavior must be associated with field-induced FM correlation, and this is consistent with the recent theoretical prediction by Satoh and Ohkawa[5] based on the quasi-particle band spectrum considerations.

References

[1]L. P. Regnault et al., Phys. Rev. B **38** (1988) 4481.
[2]M. Sato et al., J. Phys. Chem. Solids **60** (1999) 1203.
[3]P. Haen et al., J. Low Temp. Phys. **67** (1987) 391.
[4]J. Rossat-Mignod et al., J. Magn. Magn. Matter. **76&77** (1988) 376
[5]H. Satoh and F. J. Ohkawa, preprint.

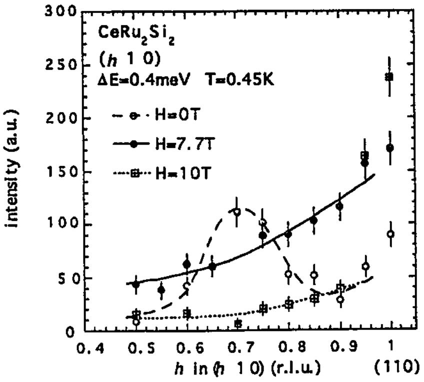

Fig.1. Field dependence of constant E-scans with ΔE=0.4 meV along $[h,1,0]$ (in r.l.u.) at T=0.45 K.

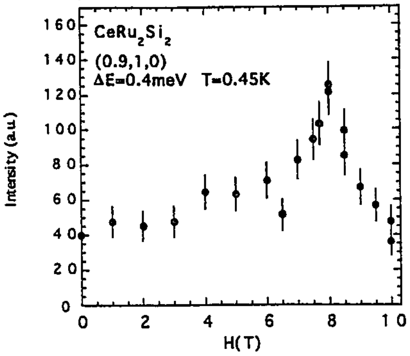

Fig.2. Field dependence of the scattering intensity with ΔE=0.4 meV at (0.9,1,0) (T=0.45 K).

2.3.3

Magnetic Field Effect on the Antiferromagnetic Ordering in $La_{2-x}Sr_xCuO_4$ with x=0.12

M. Sato, S. Katano, K. Yamada[A], T. Suzuki[B,*] and T. Hukase[B]

ASRC, JAERI, Tokai, Ibaraki, 319-1195
[A] Institute for Chemical Research, Kyoto University, Uji, Kyoto, 611-0011
[B] Institute for Materials Research, Tohoku University, Sendai, Miyagi, 980-8577

In the recent studies on the high-T_C superconductor $La_{2-x}Sr_xCuO_4$ (LSCO), it has been discovered that antiferromagentic ordering coexists with the superconductivity in the compounds with x of around 0.12.[1,2] In these compounds, the superconductivity is suppressed, which is related with the "1/8 problem". The relationship between the antiferromagnetic order and the superconductivity is attracting much attention to understand the mechanism of the high-T_C superconductivity. Quite recently, for LSCO with x=0.12, we have grown a sample with T_C=12 K. In this sample, the critical magnetic field H_C of the superconductivity is estimated to be around 8 T. In order to investigate the field-dependence of the antiferromagnetic order in this sample, we carried out neutron diffraction experiments under high magnetic field using Liquid He Free Type 10T Magnet developed by the neutron scattering group of JAERI.

Figure 1 shows the field dependence of the magnetic Bragg peaks around (0.5,0.62,0) and (0.5,0.38,0) at T=4.2 K. As can be seen in this figure, applying filed of 10 T, the integrated intensities of the peaks increase significantly by about 40 % of that under 0 T. This result suggests that the destruction of the superconductivity enhances the antiferromagnetic order.

References

[1] T. Suzuki et al. Phys. Rev. B57,R3229 (1998)

[2] H. Kimura et al. Rhys. Rev. B59, 6517 (1999)

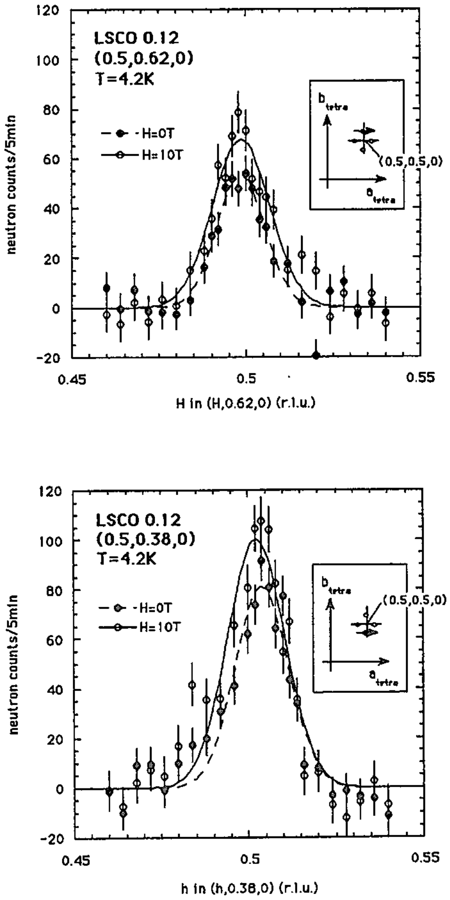

Fig.1 Field dependence of the magnetic Bragg peaks at T=4.2 K.

---

* Present Address : Department of Physics, Sophia University, 7-1 Kioi-cho, Chiyodaku 102-8554

2.3.4

Study of the Magnetic Ordering in $La_{2-x}Sr_xCuO_4$ with x=0.12 by Neutron Diffraction

M. Sato, S. Katano, K. Yamada[A], T. Suzuki[B,*] and T. Hukase[B]

ASRC, JAERI, Tokai, Ibaraki 319-1195
[A]Institute for Chemical Research, Kyoto University, Uji, Kyoto 611-0011
[B]Insititute for Materials Research, Tohoku University, Sendai, Miyagi 980-8577

One of the attractive features of the high-T_C superconductor $La_{2-x}Sr_xCuO_4$ (LSCO) is the suppression of the superconductivity observed in the compounds with x of around 0.12, which is called the 1/8 problem. In the recent neutron diffraction studies on these compounds, it has been discovered that a static antiferromagnetic long range order coexists with the superconductivity.[1,2)] The relationship between this magnetic ordering and the superconductivity is considered to be important to understand the mechanism of the high-T_C superconductivity. For the samples of LSCO with x=0.12, T_C is ordinarily around 32 ~ 34 K, and shows a small dip in the bell-shaped curve which represents T_C vs. x. These samples were grown and annealed at the oxygen atmosphere. Quite recently, we have grown a sample with T_C of 12 K for x=0.12, which was grown under the air and then annealed at the oxygen atmosphere. This T_C is fairly lower than that of the samples described above. In the present work, we investigate the magnetic ordering in this new sample with T_C=12 K and that with T_C=32 K by neutron diffraction.

At first, we compared the magnetic structures in these two compounds. Similar to the previous results [2,3)], the Bragg peaks due to the magnetic ordering are observed at the reciprocal lattice points of $(1/2\pm\varepsilon, 1/2\mp\delta, 0)$ and $(1/2\mp\delta, 1/2\pm\varepsilon, 0)$, as shown schematically in Fig.1. As can be seen in the figure, the direction of the incommensurability is slightly shifted by δ from the direction pararell to the crystal axis for the tetragonal structure in which this compounds crystallize at high temperature. In both samples, ε and δ take almost the same values, respectivly; $\varepsilon=0.12\pm0.002$, $\delta=0.004\pm0.001$.

Secondly, Fig.2 shows the temperature-dependence of the intensity of the magnetic Bragg peaks. In this figure, the intensities are normalized by the value at 10 K. The ordering temperatures T_m are about 25 K for the sample with T_C=12 K, and about 35 K for that with T_C=32 K, respectively. This sample dependence of T_m seems to suggest that T_m has a correlation with T_C. However, in the studies on the x-dependence of the magnetic ordering in $(La_{1-y}Nd_y)_{2-x}Sr_xCuO_4$ with x of around 0.12, a competition between T_m and T_C is clear.

Furthermore, we investigate the temperature-dependence of δ in the sample with T_C=12 K. The results are shown in Fig.3. As shown in this figure, we found that δ decreases above T_C and disappears around T_m. It, however, needs more investigations to clarify whether this phenomenon is related with the superconductivity or not.

*Present Address : Department of Physics, Sophia University, 7-1 Kioi-cho, Chiyodaku 102-8554

Refereces

[1] T. Suzuki et al., Phys. Rev. B57 (1998) R3229

[2] H. Kimura et al., Rhys. Rev. B59 (1999) 6517

[3] Y. S. Lee et al. Phys. Rev. B60 (1999) 3643

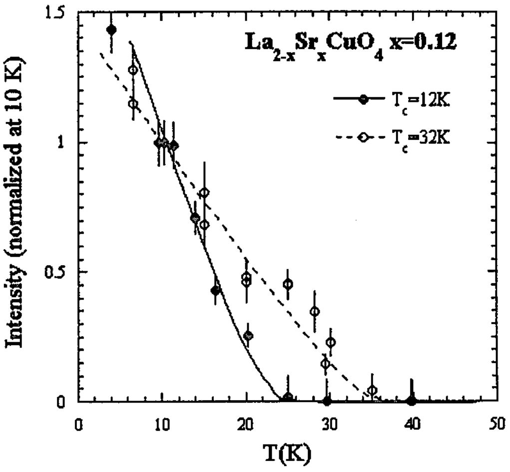

Fig.2 Temperature dependence of the intensity of the magnetic Bragg peaks.

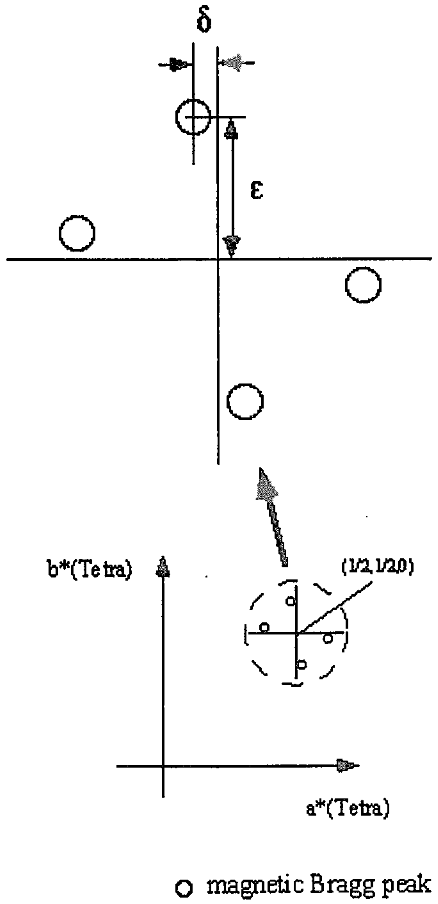

Fig.1 Positions of the magnetic Bragg peaks in the reciprocal lattice space.

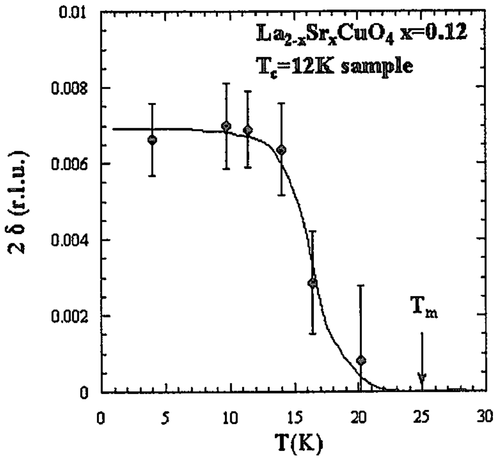

Fig.3 Temperature dependence of δ of the sample with T_C=12 K.

2.3.5

Neutron-Scattering Study of the "17.5 K Transition" in URu_2Si_2

H. Amitsuka, M. Yokoyama, K. Kuwahara[1], M. Sato[2], N. Metoki[2],
S. Kawarazaki[3], Y. Miyako[3], and J.A. Mydosh[4]

Graduate School of Science, Hokkaido University, Sapporo 060-0810, Japan
[1]Department of Physics, Tokyo Metropolitan University, Hachioji, Tokyo 192-0397, Japan
[2]Advanced Science Research Center, JAERI, Ibaraki 319-1195, Japan
[3]Graduate School of Science, Osaka University, Toyonaka 560-0043, Japan
[4]Kamerlingh Onnes Laboratory, Leiden University, 2300 RA Leiden, The Netherlands

A puzzling phase transition at $T_o \sim 17.5$ K of the heavy-electron 5f system URu_2Si_2 is characterized by development of an unusually small staggered moment μ_o accompanied by large bulk anomalies and sharp magnon excitations. Through elastic and inelastic neutron scattering for a high quality single crystal, we have studied the influence of pressure P up to ~ 2.8 GPa on this phase transition. The experiments were performed on a triple-axis spectrometer TAS-1 at the JRR-3M reactor. Pressure was applied by means of a barrel-shaped piston cylinder and monitored by measuring the lattice constant of NaCl. Elastic scans were performed in the $(hk0)$ scattering plane, particularly on the antiferromagnetic Bragg reflections (100) and (210), and on the nuclear ones (200), (020) and (110). For inelastic scattering measurements, we made constant-Q scans at $Q = (1,0,0)$ and $(1,0.4,0)$, using neutrons with a fixed incident energy of $E_0 = 14.7$ meV. The energy resolution determined from the vanadium incoherent scattering was ~ 0.95 meV (FWHM).

We have found URu_2Si_2 to undergo a new phase transition under high pressure, at $P_c \sim 1.5$ GPa (Fig.1)$^{1-3)}$. Below P_c, the sublattice magnetization associated with the 17.5 K transition is strongly enhanced from $\sim 0.017(3)\ \mu_B$ to $\sim 0.25(2)\ \mu_B$, where the unusual T-linear behavior is conserved. In contrast to the ten-times increase in the saturation moment, the transition temperature rises only ten percent with pressure. These results for $P < P_c$ indicate that the tiny dipole moments are intrinsically induced by the 17.5 K transition, but that they are not the primary order parameter. A simple analysis based on the Landau's theory supports the hidden (non-dipolar) order scenarios$^{1)}$. Above P_c, on the other hand, the T variations of the staggered moment are well described by a 3D-Ising model, where we also found that the sharp magnon excitations below P_c disappear$^{3)}$. We suggest that the magnetic instabilities at P_c as well as the exotic phase below P_c could be ascribed to the competitions between the quadrupolar and dipolar degrees of freedom in the Γ_5 non-Kramers doublet$^{2,3)}$. In this context the low-pressure phase will be described as a staggered quadrupolar ordered state concomitant with dynamical spin fluctuations$^{4)}$.

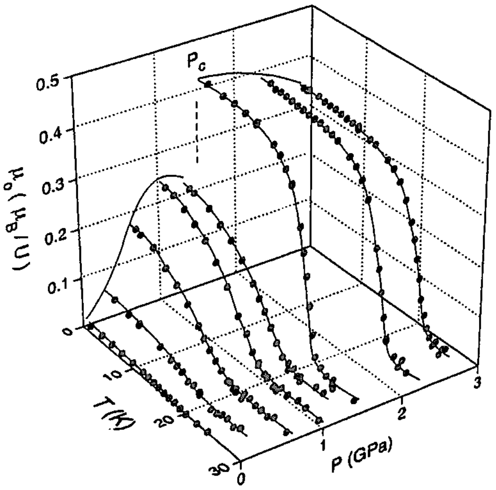

Fig.1 Temperature variations of the antiferromagnetic staggered moment μ_o of single-crystalline URu_2Si_2 under hydrostatic pressures.

References

[1] H. Amitsuka et al., Phys. Rev. Lett. **83**(1999), 5114.
[2] H. Amitsuka et al., Physica B **281&282** (2000), 326.
[3] H. Amitsuka et al., to be published in J. Phys. Soc. Jpn.
[4] F.J. Ohkawa and H. Shimizu, J. Phys.: Condens. Matter **11** (1999), L519.

2.3.6 Magnetic properties of the ladder compound $(Sr,Ca)_{14}Cu_{24}O_{41}$

T. NAGATA, H. FUJINO, J. AKIMITSU, and S. KATANO[1]

Department of Physics, Aoyama-Gakuin University, Setagaya-ku, Tokyo 157-8572
[1]*Neutron Scattering Group, Advanced Science Research Center, Japan Atomic Energy Research Institute, Tokai, Ibaraki 319-1195*

The ground state of hole-doped spin ladder system $Sr_{14-x}Ca_xCu_{24}O_{41}$ has been believed to be spin gap state from the NMR[1] and neutron scattering experiments.[2] However, magnetic long range ordering was observed by the specific heat and magnetic susceptibility measurements.[3,4] The magnetic susceptibility measurements reported that the magnetic long range order is antiferromagnetic and the direction of magnetic moments at x=10 is different from that at x=11.5. To examine the difference of magnetic structure between x=10 and 11.5, neutron scattering experiment was performed for x=10 samples.

The experiments have been carried out using TAS-1 (2G) triple-axis spectrometers in JRR-3M at JAERI with a collimation of 40′-40′-S-80′-80′. In these experiments, we used the neutron wavelength of 2.44 Å and placed the pyrolytic graphite and sapphire filters in front of the sample to eliminate the higher order contamination. $Sr_4Ca_{10}Cu_{24}O_{41}$ single crystals were mounted on a dilution refrigerator. The lattice constants along chain direction were determined to be c_L(ladder unit) = 3.902 Å and c_C(chain unit) = 2.749 Å for x=10 (at 1 K) from the neutron scattering measurements. In these lattice units, the lattice constant c becomes more commensurate at $c = 12\times c_L \approx 17\times c_C$ rather than at $c = 7\times c_L \approx 10\times c_C$. For this reason, in this report, we regard the lattice constant c as the length of $12\times c_L \approx 17\times c_C$.

Figure 1 shows the temperature dependence of the neutron scattering intensities from (3 0 12) at x=10 and (1 0 12) at x=11.5.[3] Bragg peak intensity at x=10 gradually increases below 1.1 K with decreasing temperature, which is corresponding to the T_N confirmed in the specific heat and susceptibility measurements, so this Bragg peaks must be magnetic in origin. In fact, the polarized neutron scattering experiments were performed for one of the Bragg peaks, (1 0 12) at x=11.5, and the results clearly showed that the Bragg peak, (1 0 12), is purely magnetic.[3]

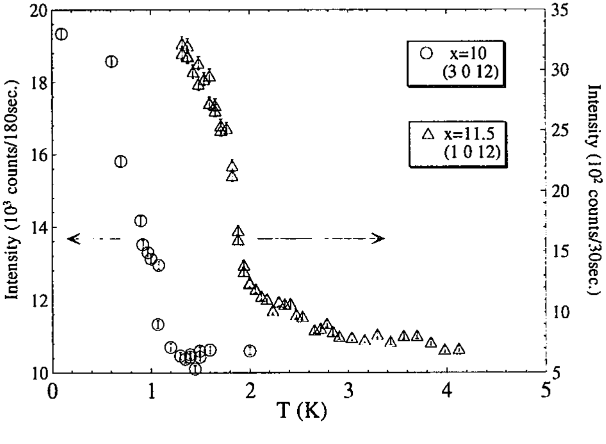

Fig. 1. Temperature dependence of magnetic Bragg peak intensities from (3 0 12) at x=10 and (1 0 12) at x=11.5.

Table I. Observed integrated intensities ($I_{\rm obs}$) and calculated intensities ($I_{\rm calc}$) of magnetic Bragg reflections on $Sr_4Ca_{10}Cu_{24}O_{41}$. $I_{\rm obs}$ was measured at T=0.1 K.

(h k l)	$I_{\rm obs}$	$I_{\rm calc}$
(1 0 2)	44	440
(3 0 2)	18	161
(1 0 12)	151	150
(3 0 12)	687	460
(5 0 12)	345	366
(1 0 22)	8	19

Table I summarizes the observed Bragg peak positions and intensities (I_{obs}) at x=10. I_{obs} is integrated intensity after subtracting the intensity at 1.5 K from at 0.1 K. We confirmed that the FWHM of the observed Bragg peaks is nearly resolution limited.

The magnetic structure factors (I_{calc}) were calculated with using the magnetic structure at x=11.5 reported in Ref.3. In this calculation, the direction of magnetic moments are supposed to be directed along c-axis and distributed uniformly at only chain sites. The magnetic moments at ladder site are ignored. Because neutron elastic scattering experiments in b-c plane were not performed for x=10, we could not determine the magnetic structure at ladder site. The magnetic form factors at chain site were evaluated by comparing with the magnetic peak intensity at (1 0 12) and nuclear Bragg peak intensity at (0 0 24). The estimated value of $\mu_{\rm eff}$ at x=10 is about $\mu_{\rm eff}$(chain) $\sim$ 0.378 $\mu_{\rm B}$/Cu in chain layer at 0.1 K.

From this experiment, we found that the antiferromangnetic structure at x=10 is basically same with that at x=11.5 except for the direction of magnetic moments. A more detailed study is required to completely clarify the magnetic structure both at chain and ladder planes.

---

1) K. Magishi *et al.*, Phys. Rev. B **57** (1998) 11533.
2) S. Katano *et al.*, Phys. Rev. Lett. **82** (1999) 636.
3) T. Nagata *et al.*, J. Phys. Soc. Jpn. **68** (1999) 2206.
4) T. Nagata *et al.*, unpublished.

2.3.7 Neutron Scattering Study of $Sr_2EuCu_2RuO_8$

T. Mochiku, Y. Matsuoka[1,*], N. Metoki[1], D.P. Hai[2] and K. Kadowaki[2]

National Research Institute for Metals, Tsukuba, Ibaraki 305-0047, Japan
[1]Japan Atomic Energy Research Institute, Tokai, Ibaraki 319-1195, Japan
[2]Institute of Materials Science, University of Tskuba, Tsukuba 305-8573, Japan

Coexistence of ferromagnetism and superconductivity has been discovered in $Sr_2GdCu_2RuO_8$ which has a Curie transition around 135 K and a superconducting transition around 15-40 K [1]. A recent study [2] using a zero-field muon spin rotation experiments shows that this compound is microscopically single phase with no evidence of spatial separation of ferromagnetic and superconducting phases. We report neutron scattering results for a $Sr_2EuCu_2RuO_8$ sample exhibiting a magnetic transition at 135 K and without superconductivity, which compound has the same structure as $Sr_2GdCu_2RuO_8$.

Sample 'was prepared by the solid state reaction of stoichiometric amount of $SrCO_3$, Eu_2O_3, CuO and RuO_2 powder. Isotope Eu153 with powder form of Eu_2O_3 was used in stead of natural Eu_2O_3, because the natural Eu has strong absorption for neutron. Neutron powder scattering experiments were carried out using a triple-axis spectrometer, TAS-2, installed in the research reactor, JRR-3M at the Japan Atomic Energy Research Institute. Intensity data of 101, 004 and 113 Bragg reflections were collected at room temperature, 150 K, 75 K and 7 K. Fig. 1 shows temperature dependence of 113 Bragg reflection. The intensity increases with decreasing temperature, although we observed no change of the intensity of other reflections within the deviation. More detailed experiments are required to discuss magnetism in this system.

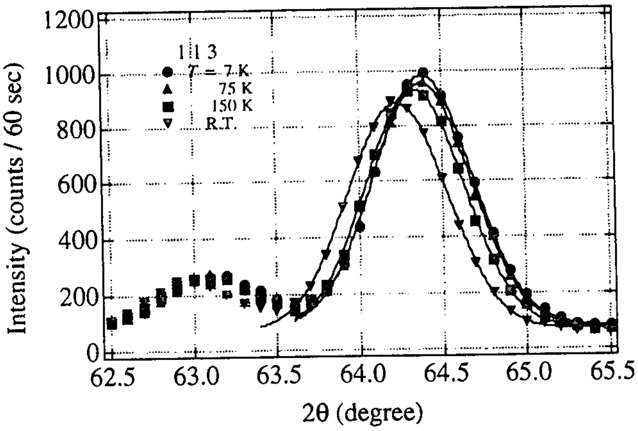

Fig. 1 Temperature dependence of 113 Bragg reflection.

References

[1] J.L. Tallon, C. Bernhard, M.E. Bowden, P.W. Gilberd, T.M. Stoto and D.J. Pringle: IEEE Trans. Appl. Supercond. 9 (1999) 1696.
[2] C. Bernhard, J.L. Tallon, Ch. Niedermayer, Th. Blasius, A. Golnik, E. Brucher, R.K. Kremer, D.R. Noaks, C.E. Stronach and E.J. Ansaldo: Phys. Rev. B 59 (1999) 14099.

[*] Present address: Nara Women's University, Nara, Nara 630-8506, Japan

2.3.8 Neutron diffraction study of $La_{1-x}Ca_xMnO_3$ with x= 0.18 and 0.25

Y. Ono[1], Shahnaz Begum[1], H. Fujishiro[2], M. Ikebe[2], T. Fukase[3] and T. Kajitani[1]
[1] Graduate School of Engineering, Tohoku University, Sendai, 980-8579
[2]Faculty of Engineering, Iwate University, Morioka, 020-8551
[3]IMR, Tohoku University, Sendai, 980-8577

Perovskite-based manganese oxides, $La_{1-x}A_xMnO_3$, where A refers to Ca or Sr, have attracted much attention since the discovery of colossal magnetoresistance [1]. The Sr-doped manganite undergoes successive phase transitions in the vicinity of x=1/8 [2]. We have studied deformation of MnO_6 octahedron and magnetic structure of $La_{1-x}Ca_xMnO_3$ with x~1/8 by means of neutron powder diffraction.

Powder samples of $La_{1-x}Ca_xMnO_3$ with x=0.18 and 0.25 were prepared by a conventional solid state reaction from stoichiometric mixture of La_2O_3, Mn_2O_3 and $CaCO_3$. Their magnetizations were measured by a SQUID magnetometer (Quantum design Co.) in the range from 4.2 K to 290 K. Neutron powder diffraction experiments were carried out using HRPD installed at JRR-3M (JAERI). The Pnma type space symmetry was assumed for both samples. Structure parameters and spin arrangement were determined using a Rietveld analysis program, GSAS [3]. Figure 1 shows observed, calculated and difference profiles of powder neutron diffraction intensities of $La_{0.75}Ca_{0.25}MnO_3$ at 8K. Figure 2 shows temperature variation of Mn-O bond lengths in the sample with x=0.18 (open circles). A large breathing-type *Jahn-Teller (J-T)* distortion was observed for the MnO_6 octahedron at low temperatures, i.e., in MnO_4 square plane, two equivalent Mn-O(2') bonds become short while others elongate. Mn-O(1) distance remains practically unchanged at low temperatures. As shown in Fig.2, the *J-T* distortion of this sample is comparable to that of $La_{1-x}Sr_xMnO_3$ with x=0.125 (filled circles) [4]. However, the sample with x=0.25 (open square) does not show such large distortion at 8 K. The magnetic spins on Mn ions are almost colinearly oriented parallel to [001] direction in both samples at low temperatures. Figure 3 shows the calculated magnetic moments of Mn ion (x=0.18) and the magnetizations measured under an applied field of 0.5 T.

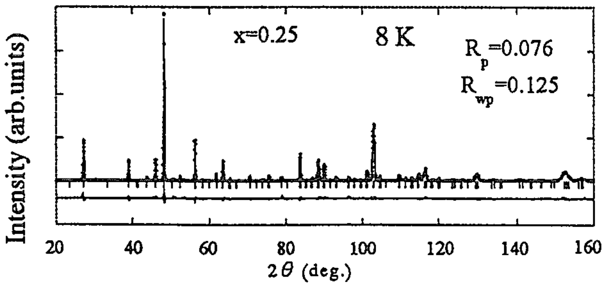

Figure 1 Observed, calculated and difference neutron diffraction profiles of $La_{0.75}Ca_{0.25}MnO_3$.

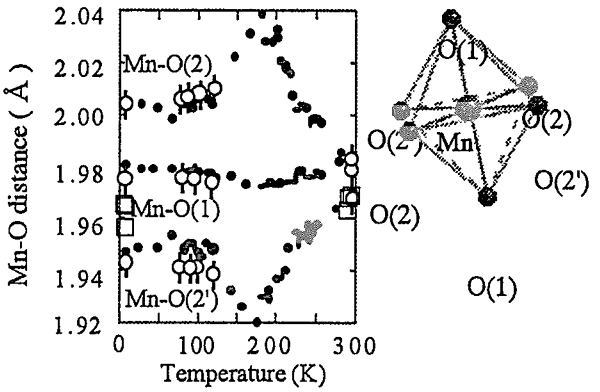

Fig.2 Temperature variations of Mn-O bond lengths in $La_{0.82}Ca_{0.18}MnO_3$ (open circles) and in $La_{0.875}Sr_{0.125}MnO_3$ (filled circles) [4]. Open squares represent Mn-O bond lengths of $La_{0.75}Ca_{0.25}MnO_3$ at 8 K and 293 K.

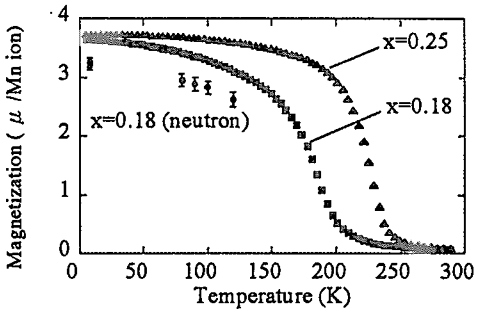

Fig.3 Magnetizations as a function of temperature. ● represents the neutron diffraction data. ▲ and ■ are SQUID data.

References

[1] Millis, A.J. Nature 392(1998)147.
[2] Yamada, Y. *et al.* Phys.Rev.Lett.77(1996)904.
[3] von Dreele, R.B. & Larson, A.C. General Structure Analysis System, University of California (1998).
[4] Argyriou, D.N. *et al.* Phys.Rev.Lett.76(1996)3826.

2.3.9 Nuclear- and Electron-Density Distribution in the Superconductor $HgBa_2CuO_{4+\delta}$

F. Izumi, S. Kumazawa[1], W.-Z. Hu[2,3], A. Yamamoto[2], K. Oikawa[4] and T. Ikeda

National Institute for Research in Inorganic Materials, 1-1 Namiki, Tsukuba, Ibaraki 305-0044, Japan
[1] Institute of Materials Structure Science, KEK, 1-1 Oho, Tsukuba, Ibaraki 305-0801, Japan
[2] Superconductivity Research Laboratory, 1-10-13 Shinonome, Koto-ku, Tokyo 135-0062, Japan
[3] Tokyo University of Mercantile Marine, 2-1-6 Etchujima, Koto-ku, Tokyo 135-8533, Japan
[4] Japan Atomic Energy Research Institute, Tokai, Naka-gun, Ibaraki 319-1195, Japan

We have recently developed a structure refinement system REMEDY [1] comprising RIETAN for angle-dispersive diffraction [2] and MEED for a maximum entropy method (MEM). MEM analysis and whole-powder-pattern fitting are repeated with REMEDY. In the latter, the diffraction pattern calculated from F_c(MEM) data derived by the Fourier transform of nuclear/electron densities is fit to the observed one to refine parameters irrelevant to the structure. This iterative procedure enables us to model disordered atomic arrangements, covalent bonds, nonlocalized electrons, and anharmonic thermal motion more adequately than the conventional Rietveld method.

We prepared a superconductor $HgBa_2CuO_{4+\delta}$ (Hg-1201; T_c = 97 K) where the content of carbonate ions substituting for O2–Hg–O2 groups was minimized to distribute excess oxygen atoms very uniformly by O_2 annealing for a relatively long time [3]. Neutron powder diffraction data of Hg-1201 were measured on HRPD with a wavelength of 1.823 Å. In structure refinements with both neutron and X-ray diffraction data, MEM-based whole-pattern fitting gave lower R factors than conventional Rietveld analysis [1,4]. Such improvements in profile fits are achieved by more sufficient representation of the real structure with nuclear/electron densities than with structure parameters in Rietveld analysis.

Figure 1 shows nuclear and electron densities on the (100) plane of Hg-1201. Interposition of bonding electrons between Hg and O2 and between Cu and O1 is clearly recognized in Fig. 1(b). The presence of a region where electron densities are negligibly low between the Cu and O2 atoms indicates nearly electrostatic interaction between them. Despite the assumption of harmonic thermal motion in the Rietveld analysis prior to the REMEDY cycles, the isosurface of nuclear densities for O2 considerably deviated from an ellipsoid. In fact, the analysis of anharmonic thermal vibration for O2 afforded significant cubic and quartic anharmonic terms.

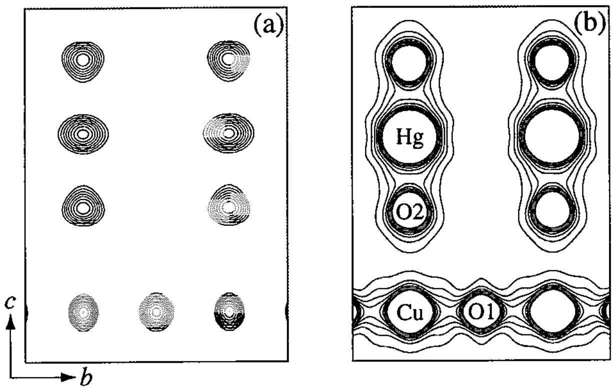

Fig. 1 (a) Nuclear- and (b) electron-density maps for the (100) plane in Hg-1201.

Interstitial oxygen defects, O3, at (1/2,1/2,0) are responsible for hole doping in Hg-1201. In Rietveld analysis, the isotropic atomic displacement parameter, B, of a slightly occupied site like O3 is often fixed arbitrarily at a typical value, *e.g.*, 1 $Å^2$, to refine only its occupancy, g, on account of very high correlation between B and g. We took more sophisticated approaches to get more reliable values of g(O3) and B(O3). That is, g(O3) was estimated at 0.14 by integrating nuclear densities of O3, and B(O3) at 1.5 $Å^2$ by evaluating mean square displacements. This technique is useful for determining B and g for partially occupied sites from nuclear densities obtained by the MEM.

References

[1] F. Izumi *et al.*: Mater. Sci. Forum, in press.
[2] F. Izumi and T. Ikeda: Mater. Sci. Forum, **321–324** (2000) 198.
[3] A. Yamamoto *et al.*: J. Low Temp. Phys. **117** (1999) 789.
[4] F. Izumi *et al.*: Physica C (Amsterdam), in press.

2.3.10 Study on the Crystal and Magnetic Structures of $(La,Tb)_{2/3}Ca_{1/3}MnO_3$ by Neutron Powder Diffraction

M. Watahiki[1,2], K. Oikawa[3], J. Suzuki[1]

[1]Advanced Science Research Center, JAERI, Tokai-mura, Ibaraki 319-1195, Japan
[2]Japan Science and Technology Corporation, Kawaguchi, Saitama 332-0012, Japan
[3]National Institute of Materials and Chemical Research, Tsukuba, Ibaraki 305-8565, Japan

Much interest is devoted to the manganese perovskite $La_{1-y}A_yMnO_3$ (A : divalent alkali ion), since the discovery of colossal magnetoresistance (CMR). A series of studies has been carried out on the systems expressed as $(La_{1-x}Tb_x)_{2/3}Ca_{1/3}MnO_3$ in which the average ionic radius of the La site is systematically varied by substituting Tb ions$^{1)}$. The motivation of the study is that by varying the x-value, one can control the band width of the e_g-band, while the carrier density is kept constant. Polycrystalline samples of $(La_{1-x}Tb_x)_{2/3}Ca_{1/3}MnO_3$ were prepared by solid-state reaction processing$^{2)}$.

The neutron powder diffraction experiments were carried out using a high resolution powder diffractometer HRPD and a triple-axis spectrometer TAS-2 constructed in JRR-3M. For HRPD experiments the incident beam was monochromatized with a vertically focused Ge(331) monochrometer for the wave length $\lambda = 0.182$ nm. The collimation 6'-20'-6' gives the resolution of typically 0.15 degrees. For TAS-2 experiments a vertically bent pyrolitic graphite (PG) monochrometer was used to obtain the incident beam with $\lambda = 0.237$ nm. Higher order contaminations were removed by a 10 cm thick PG filter. The collimation was 40'-40'-40', giving higher intensity at the sacrifice of the q-resolution.

The temperature dependence of resistivity ($\rho(T)$) curves with $x = 0.1$ and 0.3 exhibited cusp like behavior in the absence of magnetic field. These cusps appeared close to the Curie temperature (T_c) determined by ac susceptibility measurement. An application of external magnetic field of 5 T suppressed the $\rho(T)$ for both samples. The sample of $x = 0.3$ shows remarkable CMR effect of the order of 10^4 below T = 50 K. The sample of $x = 0.1$ suppressed the $\rho(T)$ close to T_c by one order of magnitude, indicating that the CMR effect is correlated with the paramagnetic-ferromagnetic transition. Figure 1 shows the Rietveld refinement pattern at room temperature for the sample of $x = 0.1$ measured on HRPD. From the Rietveld analysis we found that this profile can be explained in terms of a single phase of $(La_{1-x}Tb_x)_{2/3}Ca_{1/3}MnO_3$ with homogeneous Tb substitution into (La,Ca) sites. The lattice parameters were determined to be a = 0.545 nm, b = 0.77063(3) nm, and c = 0.54628(3) nm for $x = 0.1$ and a = 0.54577(3) nm, b = 0.76789(4) nm, and c = 0.54364(3) nm for $x = 0.3$. From the definition $t = d_{A\text{-}O}/\sqrt{2}\, d_{Mn\text{-}O}$, where $d_{A\text{-}O}$ and $d_{Mn\text{-}O}$ are the distances between the metallic ions and the neighbor oxygen atom, we calculated the tolerance factor $t = 0.913$ and 0.907 for $x = 0.1$ and 0.3, respectively. The bond angles of Mn-O-Mn becomes close to θ = 180 deg when the tolerance factor increases up to $t = 1$. The tolerance factor $t = 0.9128$ and 0.9071 for $x = 0.1$ and 0.3 obtained from the present work are consistent with the calculation.

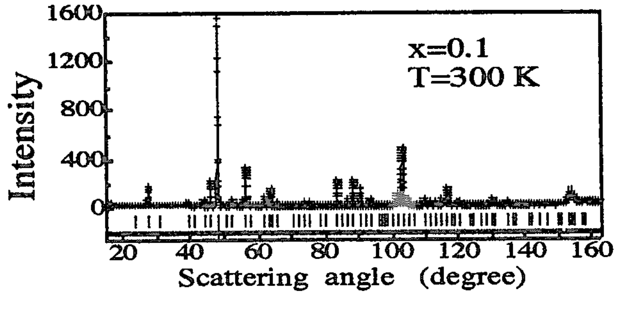

Fig. 1. The Rietveld refinement pattern at room temperature for the sample of $x = 0.1$.

Figure 2 shows the temperature dependence of the neutron powder diffraction patterns for the system of (a) $x = 0.1$ and (b) $x = 0.3$ measured on TAS-2. In the system of $x = 0.1$, it is clearly seen that at lower temperature there are extra contributions in each fundamental Bragg reflection. The integrated intensity of extra component at each indexed Bragg reflection was indexed by the ferromagnetic ordering of Mn spins with the moment of 1.45 μ_B parallel to the *a*- or *c*-axis at $T = 7$ K. On the other hand, for $x = 0.3$, a new superlattice reflection appears in the pattern taken below $T = 50$ K in addition to the ferromagnetic component similar to that for $x = 0.1$. The new peak can be indexed as (1/2,0,1/2) or (0,1,0). These two indices can not be distinguished from our experiments with rather low resolution using a triple-axis spectrometer. Since the new reflection is observed only in the low angle region, we infer that the reflection is of magnetic origin (antiferromagnetic reflection).

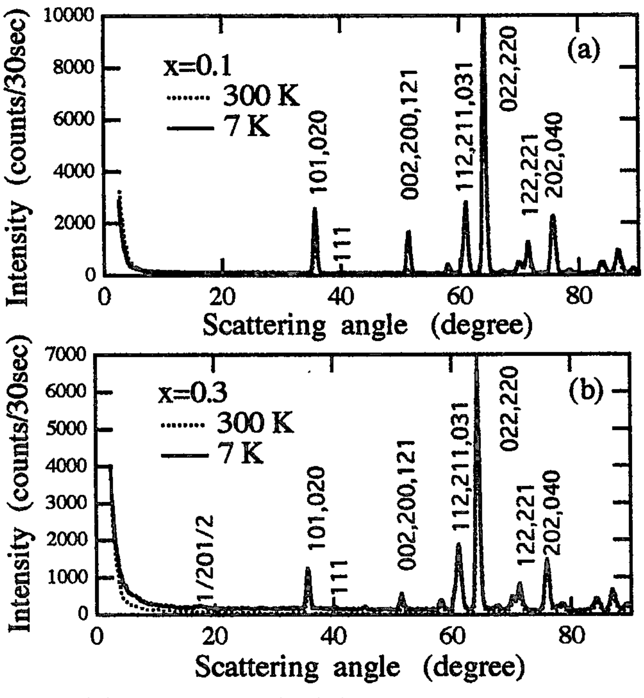

Fig. 2. The neutron powder diffraction patterns at T= 300 K and 7 K for the system of (a) $x = 0.1$ and (b) $x = 0.3$.

Figure 3 shows the temperature dependence of the three characteristic reflections (0,0,2)/(1,2,1) ($x = 0.1$ and 0.3), and (1/2,0,1/2)/(0,1,0) ($x = 0.3$). Since the intensity of (0,0,2)/(1,2,1) ($x = 0.1$) reflection develops exactly at $T_c = 190$ K, this reflection is due to the ferromagnetic ordering. The behavior of the magnetic reflections is similar to the one for $La_{0.7}Ca_{0.3}MnO_3$ in which double exchange interaction plays an important role for the magnetic transition. In contrast, for $x = 0.3$ the intensity of (0,0,2)/(1,2,1) reflection increases below about 100 K but does not show a clear transition to characterize the ordinary three dimensional cooperative ordering. This gradual temperature variation in the ferromagnetic order parameter is consistent with the result of the magnetization measurement. The intensity of (1/2,01/2)/(0,1,0) reflections ($x = 0.3$) sharply increases with decreasing temperature below 100 K. This temperature dependence of the antiferromagnetic intensity is different from the usual ordering process. Notice the intensity does not show any indication of saturation even at $T = 7$ K. The results for the system of $x = 0.3$ suggest that at $T < 100$ K, ferromagnetic and antiferromagnetic order coexist either in microscopic level (single canted antiferromagnetic phase) or in macroscopic level (segregated ferromagnetic and antiferromagnetic phases). Our result exhibited that the CMR effect appeared conspicuously with the excess doping of Tb ions since the substitution of Tb ions suppresses the growth of homogeneous ferromagnetic order.

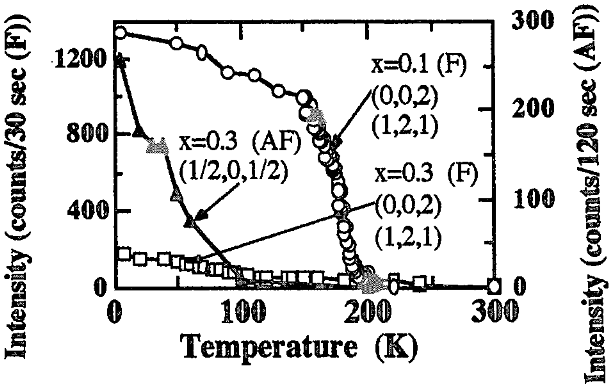

Fig. 3. Tthe temperature dependence of the three characteristic reflections (0,0,2)/(1,2,1) and (1/2,0,1/2).

References

[1] H.Y. Hwang *et al.*, Phys. Rev. Lett. **75** (1995) 914.

[2] J. Nie *et al.*, J. Magn. Mater. **192** (1999) 379

2.3.11

Small-Angle Neutron Scattering Study on Magnetoresistance Effect in Sr_2FeMoO_6

M. Watahiki[1,2], J. Suzuki[1], Y. Tomioka[3]

[1]Advanced Science Research Center, Japan Atomic Energy Research Institute, Tokai-mura, Ibaraki 319-1195, Japan
[2]Japan Science and Technology Corporation, Kawaguchi, Saitama 332-0012, Japan
[3]Joint Research Center for Atom Technology (JRCAT), Tsukuba, Ibaraki 305-8568, Japan

In order to investigate the origin of the negative magnetoresistance (MR) for the layered perovskite Sr_2FeMoO_6, both the single and polycrystalline samples have been studied by small-angle neutron scattering (SANS) under magnetic field. Sr_2FeMoO_6 has been known as a conducting ferrimagnet with a transition temperature T_N of 410 ~ 450 K[1]. It is composed of the ordered perovskites forming alternating Sr-O layer and transition-metal-O layer where Fe^{+3} (spin quantum number S=5/2) and Mo^{+5} (S=1/2) ions order alternately and the respective spins couple anitferromagnetically. Many groups have reported that negative MR effect of polycrystalline sample is larger than that of single crystalline sample. The SANS spectrum give the information on the spatial distribution of ferromagnetic correlation length and grain size with mesoscopic length scale (1 ~ 100 nm). The present study exhibited the difference appearing in SANS spectrum in both systems.

We performed measurements for the single crystalline sample prepared by floating zone-melting method and the polycrystalline sample prepared by solid-state reaction processing. Magnetoresistivity measurements have been performed under magnetic field by conventional four-probe method. The magnetic properties have been investigated by using the dc magnetization measurements. The small-angle scattering (SANS) experiments were performed by SANS-J of the research reactor JRR-3M installed at Japan Atomic Energy Research Institute (JAERI).

Figure 1 shows the temperature dependences of the resistivity $\rho(T)$ for both the samples of Sr_2FeMoO_6. Though the $\rho(T)$ curve for single crystalline sample shows the metallic behavior at zero magnetic field, the $\rho(T)$ curve for polycrystalline sample shows a gradual increase with decreasing temperature and tends to leave a large residual resistance. An application of magnetic fields suppressed the ρ for both the samples below T = 300 K. It is noted that a negative MR effect of polycrystalline sample is an order of magnitude larger than that of single crystalline sample at lowest temperature.

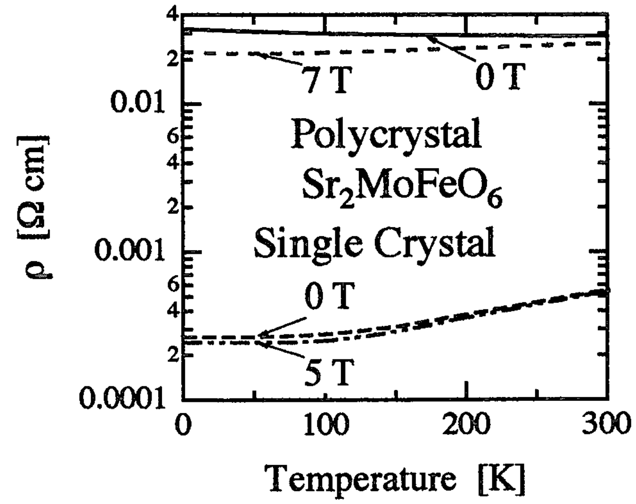

Fig. 1. The temperature dependences of the resistivity $\rho(T)$ for both the samples of Sr_2FeMoO_6.

The SANS profiles at T = 10 K where the negative MR effect was becoming more conspicuous are summarized in Fig.2 for both samples, respectively. In this figure the azimuthally averaged scattering intensities are transferred to the scattering cross-sections per unit volume, $d\Sigma(q)/d\Omega(q)$. It is clearly seen that at zero magnetic field there are diffused component of $d\Sigma(q)/d\Omega(q)$ in the SANS profile around $q = 0.1$ nm^{-1}. An application of magnetic field suppressed the diffused component of $d\Sigma(q)/d\Omega(q)$. This diffused scaterring around $q = 0.1$ nm^{-1} indicates the existence of magnetic domains with the size of several tens nm. An application of external magnetic field forces the ferromagnetic domains to grow into long range order. In the case of single crystalline sample the diffused scattering due to magnetic contribution shifts below q range used in these experiments. In comparison between the resistivity and SANS measurements, we notice that the ρ for both the samples increases with appearance of ferrimagnetic cluster.

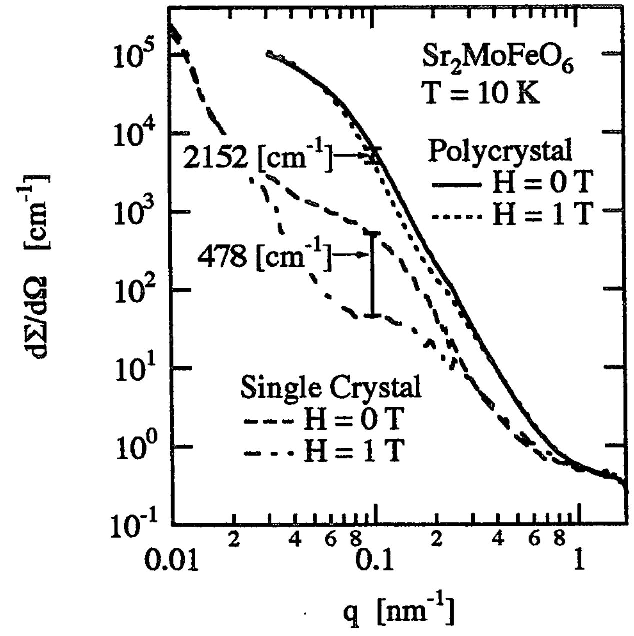

Fig.2. The SANS profiles at $T = 10$ K are summarized for both the single crystal and polycrystalline samples.

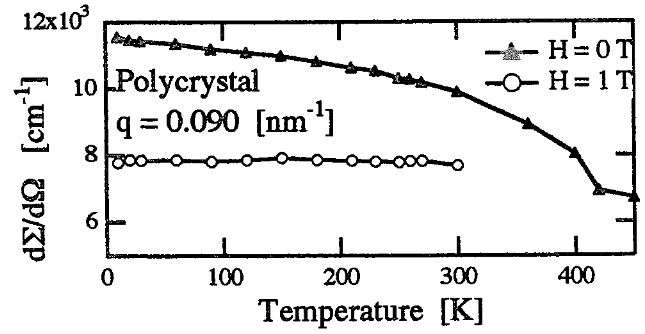

Fig. 3. The temperature dependences of $d\Sigma(q)/d\Omega(q)$ for the polycrystalline sample at $q = 0.09$ nm^{-1}

Figure 3 shows the temperature dependences of $d\Sigma(q)/d\Omega(q)$ for the polycrystalline sample at $q = 0.09$ nm^{-1} where the diffuse scattering due to magnetic contribution appeases conspicuously. At zero magnetic field, the $d\Sigma(q)/d\Omega(q)$ rises suddenly at $T = 420$ K and increased gradually with decreasing temperature. This behavior is consistent with the result that the negative MR effect was becoming more conspicuous on the lower temperature side. This result indicates that the negative MR for both samples are correlated with mesoscopic ferrimagnetic clusters. In the case of polycrystalline samples, we need to take notice of the effect of supplementary scattering from a grain boundary. The $d\Sigma(q)/d\Omega(q)$ for polycrystalline sample is larger than that for single crystalline sample within the q range up to 0.6 nm^{-1} (see Fig.2). It is a specious interpretation that this supplementary component of $d\Sigma(q)/d\Omega(q)$ which appeared in the low-q range is assigned to the scattering from a grain boundary. The grain size in polycrystalline sample is nearly one order of magnitude larger than the size of domains. Though the negative MR effect of polycrystalline sample is larger than that of single crystalline sample, we need to take notice of the influence of grain boundary in the case of polycrystalline sample. The ferrimagnetic domains in the polycrystalline sample grow into long range order comparable with grain size under magnetic field. The number of ferrimagnetic domains influences the negative MR effect. Figure 2 shows the differences between the $d\Sigma(q)/d\Omega(q)$ under $H = 0$ T and the $d\Sigma(q)/d\Omega(q)$ under $H = 1$ T at $q = 0.09$ nm^{-1} for both samples. The differences are proportional to the number of ferrimagnetic domains whose radius is corresponding to several tens nm. This value of polycrystalline sample is five times as large as that of the single crystalline sample. This result is comparable with the result that the negative MR effect of polycrystalline sample is larger than that of single crystalline sample. An application of magnetic field contributed to growing microscopic domains into a large domains, resulting in the suppresses of ρ.

References

[1] K. Kobayashi *et al.*, nature **395** (1998) 677.

2.3.12

Magnetic and Neutron Diffraction Studies of Rare-earth Orthotitanate $Pr_{1-x}Nd_xTiO_3$

K. Yoshii and A. Nakamura[1]

Japan Atomic Energy Research Institute, Synchrotron Radiation Research Center, Mikazuki, Hyogo 679-5143, Japan, and Dept. of Materials Science, Tokai, Ibaraki 319-1195, Japan[1]

Rare-earth (Ln) orthotitanates $LnTiO_3$ containing early trivalent lanthanides (Ln=La to Sm) are known as a canted antiferromagnet. The antiferromagnetic order in these systems readily disappears with slight deviation of Ti valence from 3+($3d^1$) caused by oxygen excess, Ln-deficiency, the substitution of Ln by alkali-earth ions ($Ln_{1-x}Sr_xTiO_3$), etc. Recently, as a different approach to these systems, the present authors have initiated a systematic study of mixed Ln orthotitanates (LnLn')TiO_3 to see what further variations of their physical properties are brought about, and found in most of such systems a characteristic susceptibility (χ) peak phenomenon in their χ vs. T plots, as shown in Fig. 1 for $Pr_{1-x}Nd_xTiO_3$: here, the χ peak occurs in the high Nd content region of x>0.5, as in $Ce_{1-x}Nd_xTiO_3$ reported previously. Whereas, in La-Sm system ($La_{1-x}Sm_xTiO_3$) this occurs in the low Sm content region of x<0.3. In order to elucidate the possible origin of such χ peak phenomenon in these systems, high resolution powder neutron diffraction (HRPD) experiments were performed on $Ce_{0.25}Nd_{0.75}TiO_3$ between room temperature and 10K. The results at 300 and 60K are shown in Fig.2, and demonstrate that neither structural nor long range magnetic order take place below T_N and even at the χ peak temperature(=60K) in this system, similar to $Ce_{1-x}Nd_xTiO_3$. While in this system, as seen in Fig. 1, the χ exhibits another upturn below 20K, the HRPD pattern at 10K does not reveal any magnetic peak. From these results it is judged that the χ peak in these systems originates from the onset of the cluster-glass type short range order of the frustrated canted anti-ferromagnetizm in these mixed Ln titanates.

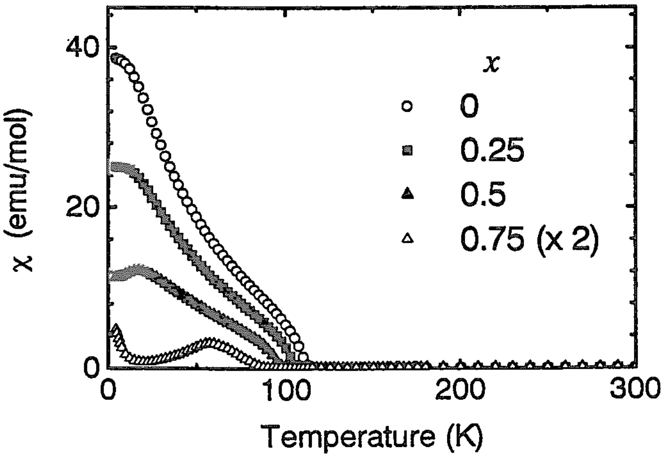

Fig. 1 DC susceptibility (χ). vs. T(K) curves of $Pr_{1-x}Nd_xTiO_3$ over the entire x range.

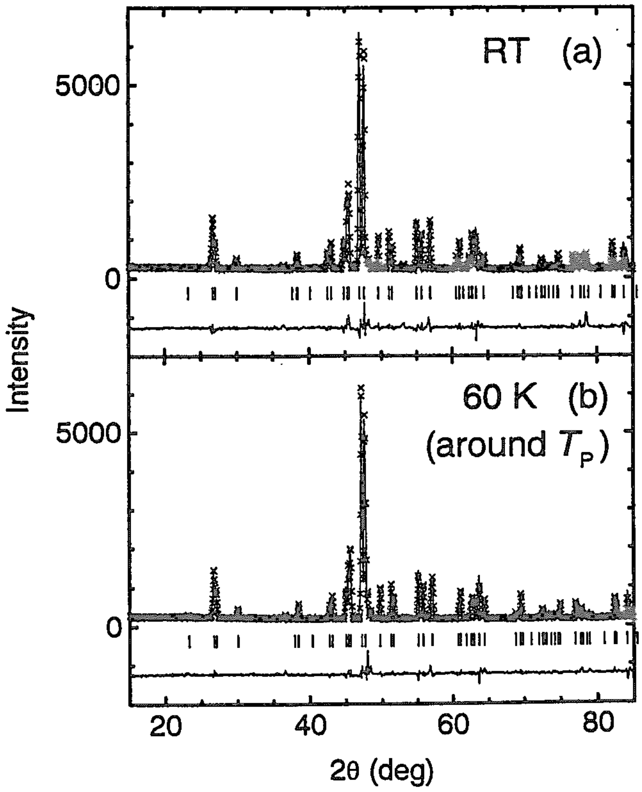

Fig. 2 HRPD pattern of $Ce_{0.25}Nd_{0.75}TiO_3$ at room temp and 50K

2.4 Magnetism and Low Temperature Physics

2.4.1 Magnetic Ordering in CeSb under Ultra-High Pressure

T. Osakabe, N. Tachi[1], M. Kohgi[1], H. Kitazawa[2]

ASRC, Japan Atomic Energy Research Institute, Ibaraki 319-1195, Japan
[1]Dep. of Physics, Tokyo Metropolitan University, Tokyo 192-0397, Japan
[2]National Research Institute for Metals, Ibaraki 305-0047, Japan

It is well known that CeSb shows the complicated magnetic (H-T and P-T) phase diagrams in spite of the simple NaCl-type crystal structure. The magnetic structures of CeSb in the phase diagram under magnetic field below about 11 T or under high pressure below about 2 GPa have been investigated so far by the neutron diffraction experiments [1]. Their magnetic structures are composed of ferromagnetic Ce layers with Γ_8 state Ce ions and paramagnetic layers with Γ_7 state Ce ions.

On the other hand, above about 2.5 GPa, it was reported that enormous enhancement of the resistivity appears at around 35 K and at the pressure of about 7 GPa the peak value of resistivity reaches a value nearly 20 times as large as that at ambient pressure [2].

In order to investigate the magnetic ordering of CeSb in the pressure – temperature range where huge peak of resistivity appears, we carried out the neutron diffraction experiments above 3 GPa on the triple axis spectrometer TAS-1 installed at the 2G beam hole of JRR-3M reactor in JAERI, Tokai. The high pressure was generated by a newly-developed sapphire anvil-type high pressure cell. The pressure was monitored by the measuring the positions of two fluorescence lines from a splinter ruby placed next to the sample.

Fig. 1 shows the temperature dependence of the (1 –2 0) and (1/2 –2 0) magnetic Bragg peaks which correspond to the type-I and type-IA antifferomagnetic order of Γ_8 state Ce ions, respectively. The results clearly show that the enormous enhancement of resistivity is accompanied by the type-I antiferromagnetic ordering and that the development of type-IA antiferromagnetic ordering below about 35 K leads to the rapid decrease of the resistivity. This may be explaned by the difference of mechanism in carrier-scattering or the difference of carrier number itself between two kinds of the magnetic phases.

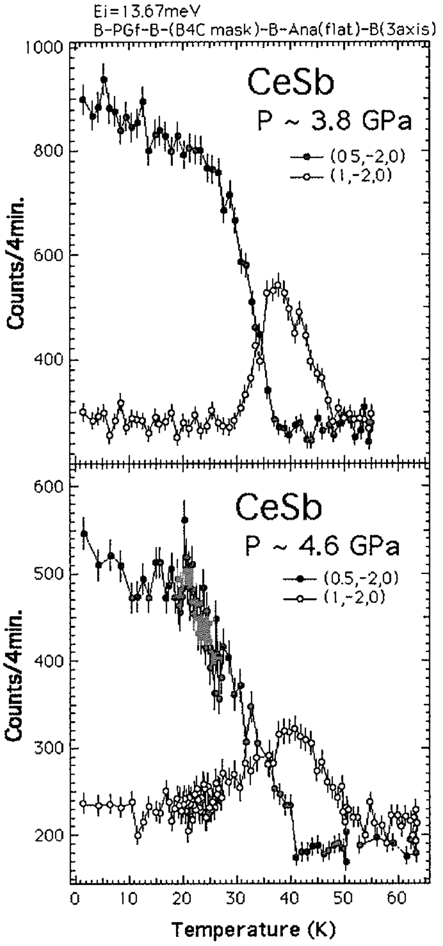

Fig. 1 Temperature dependence of the (1 –2 0) and (1/2 –2 0) magnetic Bragg peaks at 3.8 and 4.6 GPa.

References

[1] T. Chattopadhyay et al., Phys. Rev. B 49 (1994) 15096 and references therein.

[2] N. Môri et al., JJAP Series 8 (1993) pp.182-194

2.4.2 Survey of long range magnetic order in YbAs under high pressure

T. Osakabe, K. Ohoyama[1], A. Oyamada[2]

ASRC, Japan Atomic Energy Research Institute, Ibaraki 319-1195, Japan
[1] Institute for Materials Research, Tohoku University, Sendai 980-77, Japan
[2]Graduate School of Human and Environmental Studies, Kyoto University, Kyoto 606-01, Japan

YbAs is a semi-metallic compound with NaCl type crystal structure and shows heavy fermion behavior in spite of the low carrier concentration (~0.01 per Yb atom). This compound shows the type-III antiferromagnetic long range order below $T_N = 0.49$ K, whose propagation vector is [0.5, 0, 1]. The saturation magnetic moment in the ordered state is about $0.6\mu_B$, which is considerably smaller than the expected value of 1.3 μ_B for the crystal electric field ground state Γ_6. Furthermore, the short range magnetic correlation exists far above T_N [1].

Recently, Okayama et al. measured the electrical resistivity under high pressure up to 2 GPa. They found an anomalous bend in ρ(T) curve around 10 K at 0.75 GPa. They infer that the clear bend is attributed to an anomalous enhancement of T_N by applying pressure [2].

To confirm this point directory, we carried out neutron diffraction experiments under high pressure of 0.75 GPa and 0.95 GPa for single crystal sample of YbAs . The experiments were carried out using triple-axis spectrometer TAS-1, installed 2G beam hole of JRR-3M reactor. The pressure is generated by the clamp-type high pressure cell. The sample size is about 4×4×3 mm^3.

Fig. 1 show the diffraction patterns along [H 0 1] and [H 0 2] directions at 0.75 GPa. The patterns show the difference between data taken at 1.4 K and 16 K. The (200) nuclear Bragg peak at 0.75 GPa is shown in an inset of fig. 1. The intensity of the (200) peak is about 43000 counts/5sec. If the magnetic structure and the value of the magnetic moment of Yb ion under pressure are same as those under ambient pressure, the intensity at (0.5 0 1) is estimated to be about 200 counts/90sec because of the magnetic Bragg peak of a type-III antiferromagnetic order. We also carried out the mesh scan at around (0.5 0 1) at 0.75 GPa. However, as seen in fig. 1, there is no change from 1.4 K to 16 K in the diffraction patterns and no extra peak at around (0.5 0 1) in the mesh scan within the experimental error. Under pressure of 0.95 GPa, the experimental results are same as those at 0.75 GPa. These results imply that the origin of the anomalous bend in ρ(T) curve is not the static long range magnetic order. In order to investigate the origin of the anomaly seen in ρ(T) curve, we intend to carry out inelastic neutron scattering experiments under high pressure.

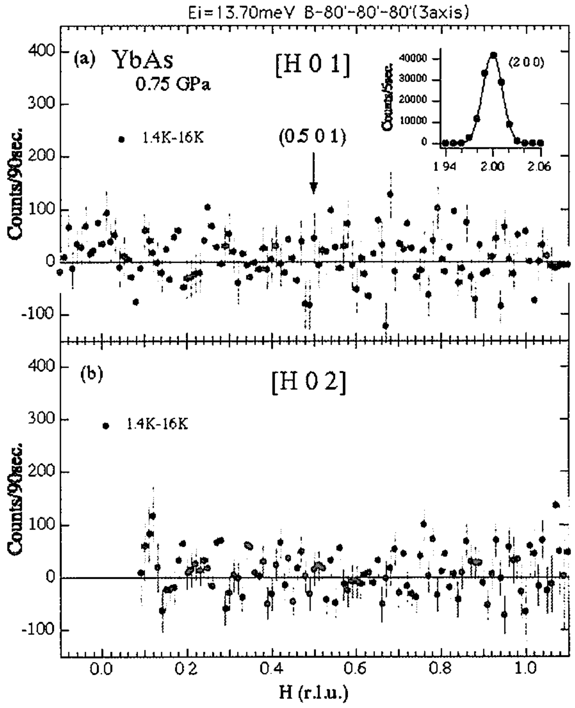

Fig. 1 The diffraction patterns along (a) [H 0 1] and (b) [H 0 2] directions at 0.75 GPa. The patterns show the difference between data taken at 1.4 K and 16 K.

References

[1] K. Ohoyama et al., J. Magn. Magn. Mater.177-181 (1998) 339 and references therein.
[2] Y. Okayama et al., Physica B 259-261 (1999) 148

2.4.3 SANS Study of Slow Dynamics in Concentrated Spin Glasses

K. Motoya, K. Hioki, J. Suzuki[1]

Department of Physics, Science University of Tokyo, Noda 278-8510 Japan
[1]Japan Atomic Energy Research Institute, Tokai, Ibaraki 319-1195 Japan

Previous neutron scattering studies on $Fe_{65}(Ni_{1-x}Mn_x)_{35}$ and $Cu_2(Mn_{1-x}Ti_x)Al$ alloys showed that magnetic clusters play an important role for the reentrant spin-glass (RSG) transition, and that a wide variety of spin dynamics observed by inelastic neutron scattering studies can be attributed to differences in the size and number of the magnetic clusters.1-3) Based on these studies, we speculate that the mechanism of slow dynamics might be probed by an observation of the time evolution of the magnetic diffuse scattering arising from magnetic clusters.

Small-angle neutron scattering measurements on two kinds of single crystal alloys, $Fe_{65}(Ni_{0.866}Mn_{0.134})_{35}$ and $Cu_2(Mn_{0.7}Ti_{0.3})Al$ were made utilizing the SANS-J spectrometer. The incident-neutron wave length and band-width are $\lambda = 0.65$nm and $\Delta\lambda/\lambda = 10\%$, respectively. The momentum-transfer range of $0.03 < Q < 2\ \mathrm{nm}^{-1}$ was covered with the sample-detector lengths of 1.35 and 10m. The time-resolved scattering patterns were taken with a time window of 10min. at low temperature RSG phase after being rapidly cooled from the ferromagnetic phase under various magnetic field. The magnetic part of the scattering patterns were well traced by the sum of Lorentzian (LOR) and squared Lorentzian (SQL) functions in the momentum space as

$$I(q) = A_L / (q^2 + \kappa_L^2) + A_S / (q^2 + \kappa_S^2)^2 ,$$

where A_L (A_S) and κ_L (κ_S) are the amplitude and the width (inverse correlation length) for the LOR (SQL) component, respectively. The goal of the present study is to determine the time evolution of these parameters from sequentially taken scattering patterns, and then to construct a real-time image of magnetic clusters. However, the statistics of the present data are not sufficient to definitely determine the time-variations of these parameters. We show in Fig.1 the time-variation of the magnetic scattering intensity from $Fe_{65}(Ni_{0.866}Mn_{0.134})_{35}$ at representative values of q. The measurement was made under the field of 120Oe and the scattering intensity for $q \perp H$ was obtained. The time variation persists up to 20 hours, as was observed in low-field susceptibility measurements. The present observation showed that the sensitivity of the present experimental method satisfies the condition to detect the slow dynamics of RSG. A quantitative analysis together with an improvement of the counting statistics by repetition of same heat cycles is under way.

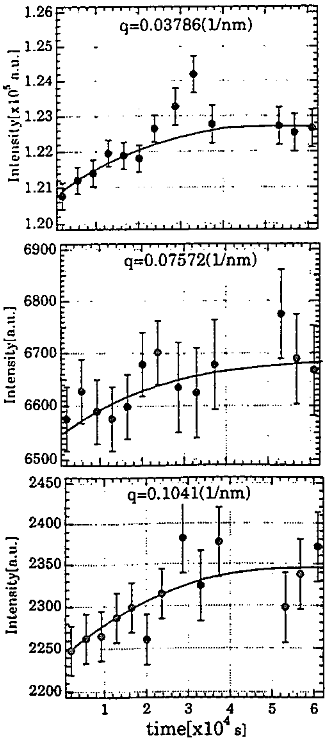

Fig. 1. Time-variation of the magnetic scattering intensity from $Fe_{65}(Ni_{0.866}Mn_{0.134})_{35}$ at representative values of q.

References

[1] K. Motoya and Y. Muraoka: J.Phys. Soc.Jpn. **62** (1993) 2819-2831.
[2] K. Motoya et al.: J.Mag.Mag.Mater. **140-144** (1995) 75-76.
[3] K. Motoya et al.: J.Phys.Soc.Jpn. **68** (1999) 2351-2360.

2.4.4 Crystal distortion and magnetic structure of γ-Mn(Ru) alloys

T. Hori[1], Y. Tsuchiya[2], Y. Ishii[2] and K. Hojou[2]

Shibaura Institute of Technology, Oomiya, Saitama 330-8570
[1]Japan Atomic Energy Research Institute, Tokai, Ibaraki 319-1106

As is well known, most Mn-rich γ-Mn alloys undergo a distortion from the face centered cubic structure to a face centered tetragonal (f.c.t.) structure with $c/a < 1$ below the Néel temperature. In some cases a distortion to a f.c.t. with $c/a > 1$ is also observed. In the γ - Mn(Ni) alloys, there is a face centered orthorhombic (f.c.o.) region in addition to the f.c.t. regions with $c/a < 1$ and $c/a > 1$ [1]. Recently, the present authors [2] have found that these three regions exist in the γ-Mn(Ga) alloys, and determined a non-collinear magnetic structure with 4 sublattices for the f.c.o. phase. The a, b and c-axis components of the magnetic moments, μ_a, μ_b and μ_c are as follows: $\mu_c^2 > \mu_b^2 > \mu_a^2 = 0$ in the f.c.o. structure with $a > b > c$. We have also found that there is the f.c.o. phase in γ-MnRu alloys with a small amount of Cu. Neutron diffraction experiments were made by using the HRPD and TAS II diffractometers in the JRR-3M reactor at JAERI. The HRPD has a higher resolution than the TAS II.

Fig. 1 shows a neutron diffraction pattern for the γ-Mn Alloy with 14 at % Ru and 5 at % Cu at 10 K obtained by the HRPD diffractometer (wave length λ=1.823 Å). The pattern can be indexed by assuming the f.c.o. structure with a = 3.566, b = 3.525 and c = 3.456 A and a non-collinear antiferromagnetic structure similar to that of the γ-Mn(Ga) alloy [2]. The components of the magnetic moments, $\mu_a = 0$, $\mu_b = 1.33$ and $\mu_c = 2.47\mu_B$/ Mn atom. We also measured the temperature dependence of these lines using the TAS II diffractometer (λ = 2.376 Å). Although the 110 and 101 reflections were not resolved, we obtained the intensities, I_{110} and I_{101}, by a curve fitting analysis using the double Gaussian functions. The results are shown in Fig. 2.

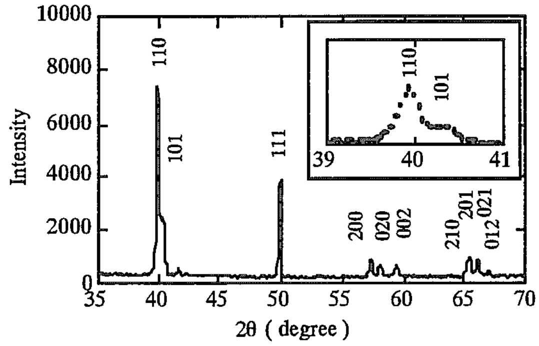

Fig. 1. Neutron diffraction pattern for the γ -Mn Alloy with 14 at % Ru and 5 at % Cu at 10 K.

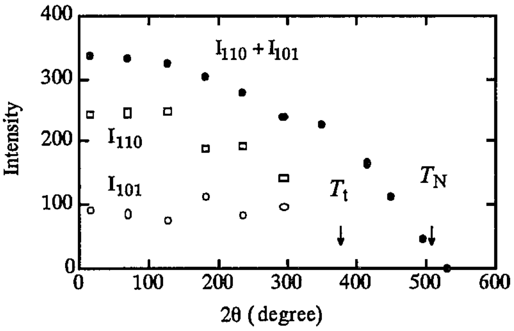

Fig. 2. Temperature dependence of the 110 and 101 intensities of the neutron diffraction for the γ-Mn Alloy with 14 at % Ru and 5 at % Cu at 10 K

From X-ray diffraction experiments, we have made confirmed that the alloy has the orthorhombic structure below T_o (= 380 K), the tetragonal structure with c/a <1 between T_t and T_N (= 510 K) and the cubic structure above T_N corresponding the Néel temperature. Jo et al. [7] have proposed a theoretical phase diagram and magnetic structures for various γ - Mn alloys on the basis of Landau expansion of the free energy. For example, the components of the magnetic moments along the three crystallographic axes μ_a, μ_b and μ_c in the f.c.o. structure with $a > b > c$ are as follows; $\mu_c^2 > \mu_b^2 > \mu_a^2$. The results of the present experiments are consistent with this theory.

[1] T. Hori, Y. Morii, S. Funahashi, H. Niida, M. Akimitsu and Y. Nakagawa; Physica B **213&214** (1995) 354.
[2] T. Jo and K. Hirai, J. Phys. Soc. Jpn **55** (1986) 1614.

2.4.5 Magnetic Structure of the Antiferromagnetic Manganese Sulfide $BaLa_2MnS_5$ by Powder Neutron Diffraction Measurements

M. Wakeshima, Y. Hinatsu, K. Oikawa[1], Y. Shimojo[1] and Y. Morii[1]

Division of Chemistry, Graduate School of Science, Hokkaido University, Sapporo 060-0810, Japan
[1] Japan Atomic Energy Research Institute, Tokai-mura, Ibaraki 319-1195, Japan

A quaternary manganese sulfide $BaLa_2MnS_5$ has a tetragonal structure with space group *I4/mcm*. Its magnetic susceptibility and specific heat showed that the Mn^{2+} ions were in the antiferromagnetic state below 58.5 K [1)].

Powder neutron diffraction patterns of $BaLa_2MnS_5$ were measured at 7 and 100 K using a High Resolution Powder Diffractometer (HRPD) in the JRR-3M reactor with a neutron incident wave length (λ = 1.82263 Å). The Rietveld analyses were performed with the neutron diffraction data.

Figure 1 shows the observed and calculated diffraction patterns for $BaLa_2MnS_5$ at 7 and 100 K. The calculated pattern at 100 K is in good agreement with the observed one (R_{wp} = 10.37 %, R_I / % = 2.39). Compared with the pattern at 100 K, no additional peaks appear, but some peaks are observed to be much stronger in intensity at 7 K. This result indicates that $BaLa_2MnS_5$ has a collinear antiferromagnetic structure (space group $I\bar{4}$) with a propagation vector $\boldsymbol{k}$ = (1/2, 1/2, 1/2) at 7 K. The magnetic moment of Mn^{2+} is estimated to be 4.21 μ_B and determined to lie in a parallel direction with the *c*-axis. The reliability factors R_{wp} and R_I for 7 K are 11.29 and 2.43 %, respectively. The magnetic structure of $BaLa_2MnS_5$ is shown in Fig. 2.

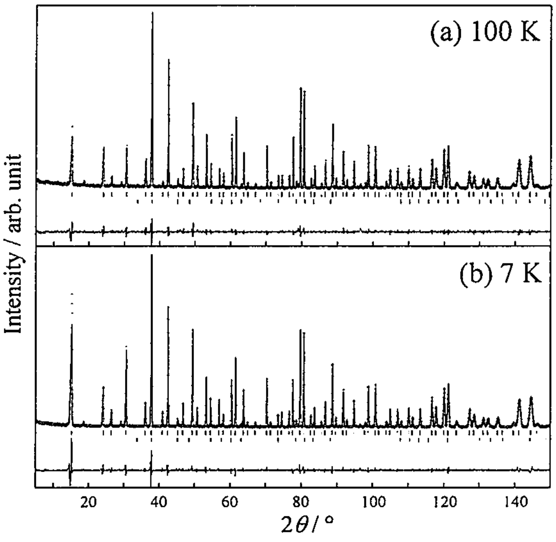

Fig. 1 Powder neutron diffraction patterns fitting for $BaLa_2MnS_5$.

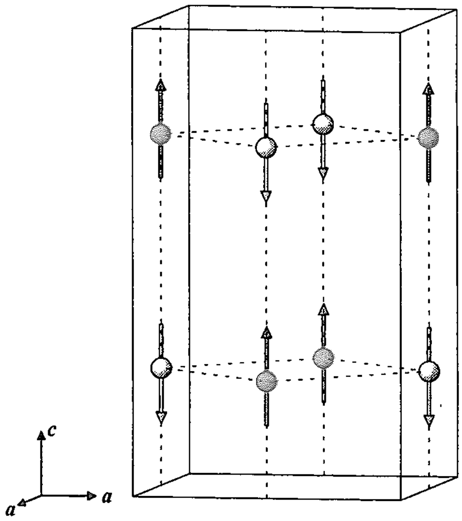

Fig. 2 Magnetic structure for $BaLa_2MnS_5$.

Reference

1) M. Wakeshima and Y. Hinatsu, J Solid State Chem., submitted.

2.4.6 Crystal Structure and Magnetic Properties of Ordered Perovskite Ba_2PrIrO_6

M. Wakeshima, D. Harada, Y. Hinatsu, K. Oikawa[1], Y. Shimojo[1] and Y. Morii[1]

Division of Chemistry, Graduate School of Science, Hokkaido University, Sapporo 060-0810, Japan
[1] *Japan Atomic Energy Research Institute, Tokai-mura, Ibaraki 319-1195, Japan*

For a series of ordered perovskites Ba_2RIrO_6 (R = rare earths) except for R = Ce and Pr, the rare earth and iridium ions are in the trivalent and pentavalent states, respectively. These compounds show paramagnetic behavior above 2 K. On the other hand, for the case of R = Ce and Pr, both R and Ir ions are in the tetravalent states and the antiferromagnetic transitions occur at 17 K for Ba_2CeIrO_6 and at 71 K for Ba_2PrIrO_6. 1)

Specific heat of Ba_2PrIrO_6 was measured using the commercial specific heat measurement system (Quantum Design, PPMS) in the temperature range 2-120 K. Powder neutron diffraction measurements of Ba_2PrIrO_6 were carried out at 7 and 100 K using a High Resolution Powder Diffractometer (HRPD) in the JRR-3M reactor with a neutron incident wave length (λ = 1.82263 Å). The Rietveld analyses were performed with the neutron diffraction data.

Figure 1 shows the temperature dependence of specific heat for Ba_2PrIrO_6. It has a λ-type anomaly at 71 K. This result reveals that both Ir^{4+} and Pr^{4+} ions are in the antiferromagnetic states below 71 K. In comparison with T_N of Ba_2CeIrO_6, high T_N of Ba_2PrIrO_6 is supposed to result from the participation of *f* electron of Pr^{4+} in the superexchange interaction

Figure 2 shows the observed and calculated diffraction patterns for Ba_2PrIrO_6 at 10 and 100 K. No magnetic reflection is found. This is caused by small magnetic moments of Ir^{4+} and Pr^{4+}. Their diffraction patterns were fitted with perovskite-type monoclinic structure (space group $P2_1/n$). The average Ir-O and Pr-O bond lengths at 100 K are calculated to be 2.004 and 2.192 Å. These values also suggest that the Ir and Pr ions are in the tetravalent states.

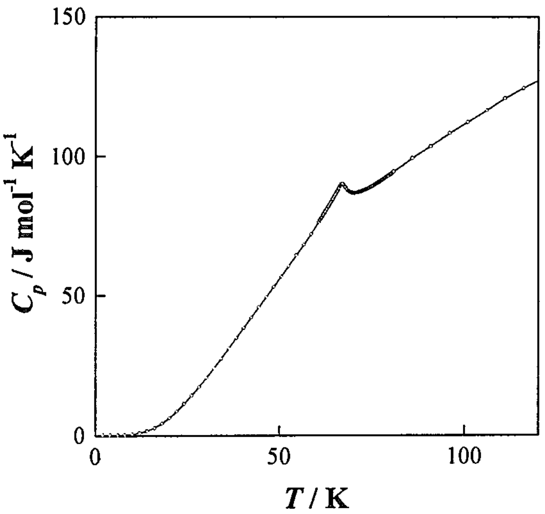

Fig. 1 Specific heat of Ba_2PrIrO_6.

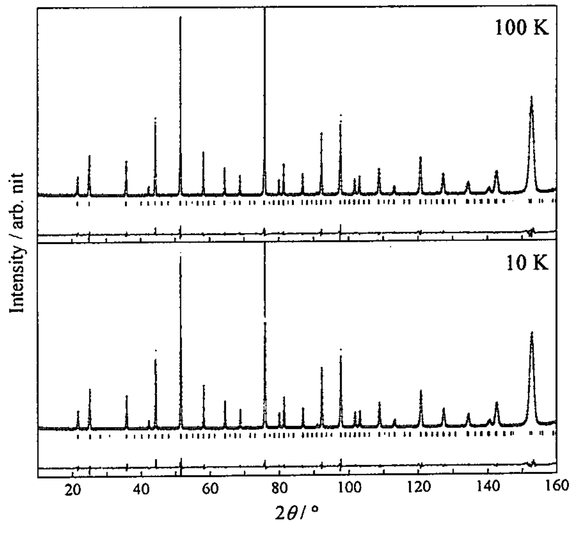

Fig. 2 Powder neutron diffraction patterns fitting for Ba_2PrIrO_6.

Reference

1) M. Wakeshima D. Harada and Y. Hinatsu, J Mater. Chem., 419, **10** (2000).

2.4.7 Neutron Diffraction Study on Ordered Perovskite Ba_2NdRuO_6

Y. Izumiyama, Y. Hinatsu, K. Oikawa[1], Y. Shimojo[1] and Y. Morii[1]

Division of Chemistry, Graduate School of Science, Hokkaido University, Sapporo 060-0810, Japan
[1] *Japan Atomic Energy Research Institute, Tokai-mura, Ibaraki 319-1195, Japan*

Magnetic properties of an ordered perovskite compound Ba_2NdRuO_6 have been reported. The temperature dependence of the magnetic susceptibility was measured in the temperature range of 2 - 300K. Two magnetic anomalies have been found in the susceptibility vs. temperature curve, i.e., one maximum of the susceptibility appears at ca.27K and an inflection of the susceptibility occurs at ca. 58K.

In order to determine the crystal structure and magnetic properties, powder neutron diffraction measurements were performed at 100, 35 and 7K using the high resolution powder diffractometer (HRPD) in the JRR-3M reactor, with a Ge (331) monochromator (λ = 1.8230 Å).

Figure 1 shows the powder neutron diffraction profiles for Ba_2NdRuO_6 and the Rietveld analysis at 100, 35 and 7K. The refinement of the data collected at 100K showed that this compound has a monoclinic symmetry with space group $P2_1/n$ (No.14), and that the structure is a perovskite with a 1:1 ordered arrangement of Ru^{5+} and Nd^{3+} over the 6-coordinate sites.

The magnetic structure determined is illustrated in Fig. 2, i.e., the magnetic type is Type I. Both the magnetic moments are found to be in the same direction from the analysis, therefore the *ab* plane would be ferromagnetic plane. On the *ab* plane, there exist both the Nd^{3+} and Ru^{5+} ions. Unfortunately, there is no difference between the profiles measured between at 35K and at 7K except for the variation of the intensity of their magnetic peaks, which indicates that two kinds of magnetic ions (Nd^{3+} ion and Ru^{5+} ion) magnetically order at the same temperature, 58K.

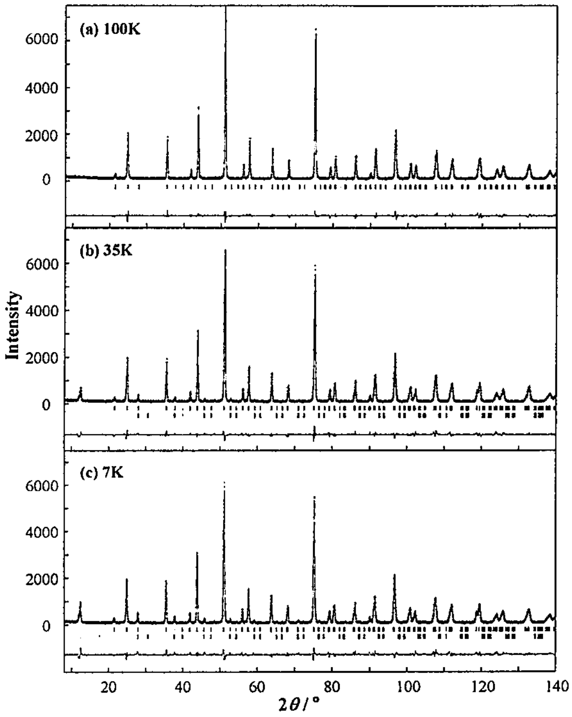

Figure 1 Powder neutron diffraction profiles for Ba_2NdRuO_6 at 100K (a), 35K (b) and 7K (c).

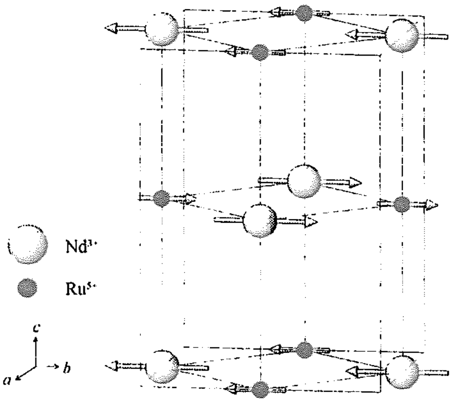

Figure 2 The magnetic structure of Ba_2NdRuO_6. Diamagnetic ions are omitted. Larger circles Nd^{3+}; smaller circles Ru^{5+}.

2.4.8 Magnetic Structure of the Ordered Perovskite Ba_2PrRuO_6 by Powder Neutron Diffraction Measurements

Y. Izumiyama, Y. Hinatsu, K. Oikawa[1], Y. Shimojo[1] and Y. Morii[1]

Division of Chemistry, Graduate School of Science, Hokkaido University, Sapporo 060-0810, Japan
[1] Japan Atomic Energy Research Institute, Tokai-mura, Ibaraki 319-1195, Japan

Magnetic properties of an ordered perovskite compound Ba_2PrRuO_6 have been reported. The temperature dependence of the magnetic susceptibility was measured in the temperature range of 2 - 300K, which is shown in Figure 1. A magnetic anomaly has been found at ca.112K.

In order to study the crystal and magnetic structures in detail, powder neutron diffraction measurements were performed at 150 and 7K using the high resolution powder diffractometer (HRPD) at the JRR-3M reactor, with a Ge (331) monochromator ($\lambda = 1.8230$ Å).

The RIETAN program was used for the analysis of the crystal and magnetic structures. The structural refinements of the neutron data collected at 150K showed that this compound has a monoclinic symmetry with space group $P2_1/n$ (No.14), $a = 6.0062(5)$, $b = 5.9863(4)$, $c = 8.4679(8)$ Å and $\beta = 90.03(2)°$, and that the structure is a perovskite with a 1:1 ordered arrangement of Ru^{5+} and Pr^{3+} over the 6-coordinate sites.

Magnetic peaks have been observed from the 7K neutron diffraction data. The magnetic structure we determined is Type I (Fig. 2), in which both the magnetic moments of Pr^{3+} and Ru^{5+} ions in the *ab* plane are parallel and the moments of adjacent planes are antiparallel each other. The strong magnetic reflections of (100) and (010) planes suggest that these moments are along the *c* axis. The ordered magnetic moments at 7K are 2.2(1) μ_B for Pr^{3+} and 2.0(2) μ_B for Ru^{5+}.

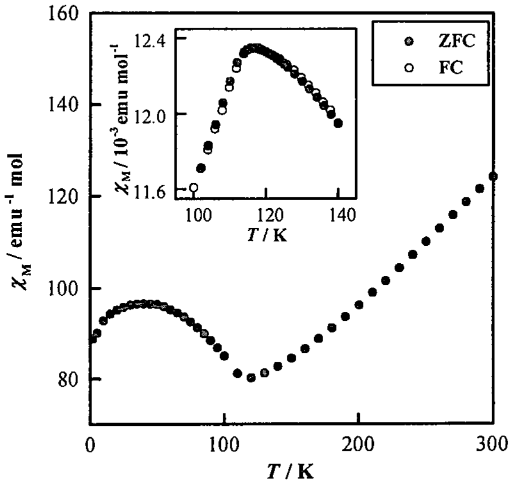

Figure 1 Temperature dependence of the magnetic susceptibility of Ba_2PrRuO_6.

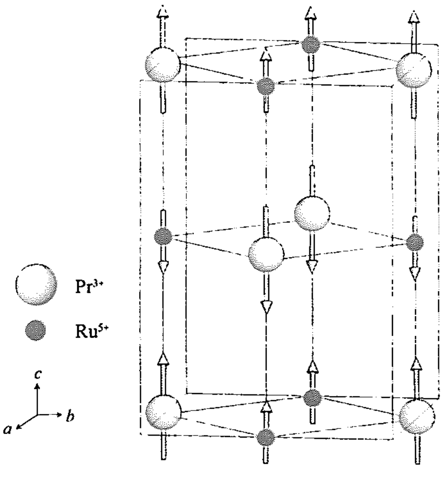

Figure 2 The magnetic structure of Ba_2PrRuO_6. Diamagnetic ions are omitted. Larger circles Nd^{3+}; smaller circles Ru^{5+}.

2.4.9 Neutron Diffraction Study on Ordered Perovskite Sr_2TbRuO_6

Y. Doi, Y. Hinatsu, K. Oikawa[1], Y. Shimojo[1] and Y. Morii[1]

Division of Chemistry, Graduate School of Science, Hokkaido University, Sapporo 060-0810, Japan
[1] *Japan Atomic Energy Research Institute, Tokai-mura, Ibaraki 319-1195, Japan*

Magnetic properties of ordered perovskite-type compound Sr_2TbRuO_6 have been reported. The magnetic susceptibility and specific heat measurements show the existence of magnetic transitions at 32K and 41K.

In order to determine the magnetic structures, powder neutron diffraction measurements were performed at room temperature and 10K with a High Resolution Powder Diffractometer (HRPD) in the JRR-3M reactor with a neutron incident wave length (λ = 1.8230Å).

Powder neutron diffraction patterns of Sr_2TbRuO_6 and the Rietveld analysis are shown in Fig.1. The crystal structure at room temperature is monoclinic with space group $P2_1/n$ (No.14), and the Tb^{3+} and Ru^{5+} ions are structurally ordered at the B sites of the ABO_3 perovskite-type structure.

The magnetic structure of Sr_2TbRuO_6 at 10K is illustrated in Fig.2. The magnetic moment of the Tb^{3+} and Ru^{5+} are ordered antiferromagnetically, respectively. Each of these orders in a type I arrangement. The gradient of the magnetic moments against the c axis is about 20°. The ordered magnetic moments are $2.99(11)\mu_B$ for Ru^{5+} and $4.98(12)\mu_B$ for Tb^{3+}. The ordered moment for Tb^{3+} is much smaller than the value of $g_J J$ ($9\mu_B$). This may be due to the fact that the magnetic moments of Tb^{3+} ions do not saturate at 10K.

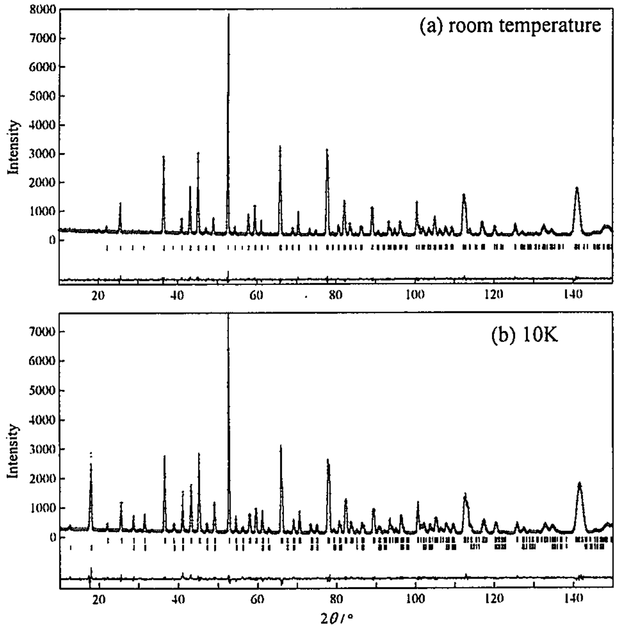

Fig.1 Powder neutron diffraction pattern fitting for Sr_2TbRuO_6.

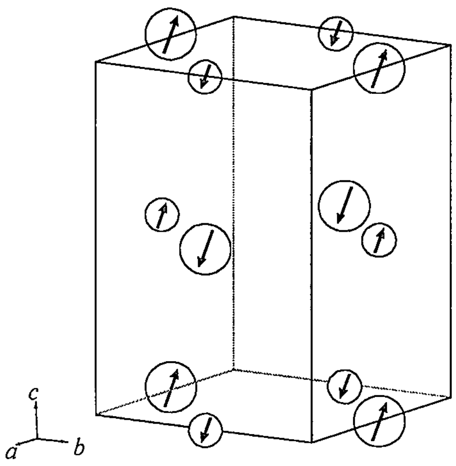

Fig.2 The magnetic structure of Sr_2TbRuO_6. Diamagnetic ions are omitted. Larger circles Tb^{3+}; smaller circles Ru^{5+}.

2.4.10 Neutron Diffraction Study on $La_{0.95}Sr_{0.05}CrO_3$ and $La_{0.85}Sr_{0.15}CrO_3$

K. Tezuka, Y. Hinatsu, K. Oikawa[1], Y. Shimojo[1] and Y. Morii[1]

Division of Chemistry, Graduate School of Science, Hokkaido University, Sapporo 060-0810, Japan
[1] Japan Atomic Energy Research Institute, Tokai-mura, Ibaraki 319-1195, Japan

Magnetic properties on perovskite-type compounds $La_{1-x}Sr_xCrO_3$ ($x = 0.05$ and 0.15) have been investigated. From the magnetic susceptibility measurements, three magnetic anomalies have been observed for $La_{0.95}Sr_{0.05}CrO_3$ (at 21K, 85K and 280K) and for $La_{0.85}Sr_{0.15}CrO_3$ (at 26K, 160K and 267K) as shown in Fig. 1.

Powder neutron diffraction measurements on these two compounds indicate that the anomaly found at *ca.* 20K in their susceptibility vs. temperature curves is not ascribable to the magnetic transition. Heat capacity measurements also show that two anomalies have been found at 90K and 280K for $La_{0.95}Sr_{0.05}CrO_3$ and at 160K, 190K and 266K for $La_{0.85}Sr_{0.15}CrO_3$, and no anomaly has been found at *ca.* 20K. The anomaly observed at *ca.* 20K in the susceptibility vs. temperature curve may be due to the weakness of the magnetic anisotropy with increasing temperature.

The magnetic structures for both the compounds have been determined to be the G-type, in which Cr atoms are antiferromagnetically coupled with the six neighboring Cr atoms at any of the temperatures. The magnetic moments of Cr atoms are directed to the *z*-axis of an orthorhombic unit cell for $La_{0.95}Sr_{0.05}CrO_3$ at 10K and 50K, and for $La_{0.85}Sr_{0.15}CrO_3$ at 10K and 50K; the G_z mode dominates. The G_y mode dominates for $La_{0.95}Sr_{0.05}CrO_3$ at 125K, *i.e.*, a spin reorientation has occurred between 50K and 125K. Table 1 summarizes the results of the magnetic structures for $La_{1-x}Sr_xCrO_3$ ($x = 0$, 0.05, 0.15).

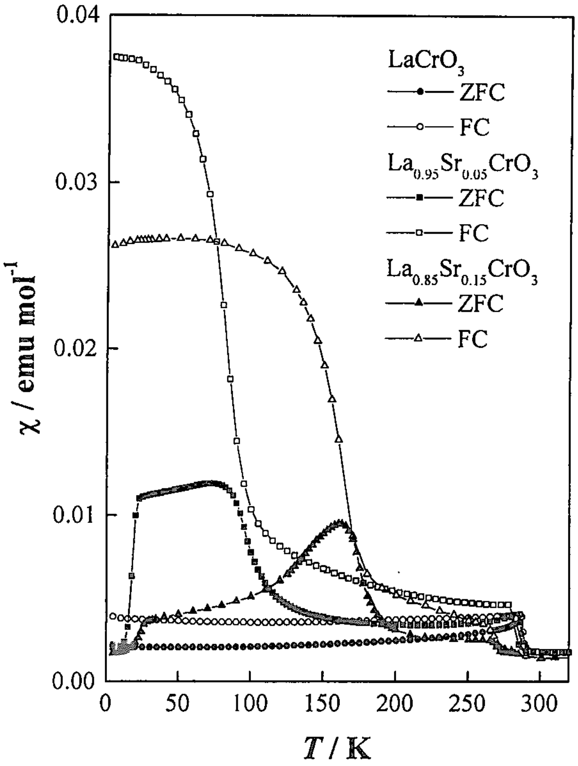

Figure 1 Temperature dependence of magnetic susceptibilities for $La_{1-x}Sr_xCrO_3$ ($x = 0$, 0.05 and 0.15) measured after zero field cooling (ZFC) and field cooling (FC).

Table 1
The magnetic structures for $La_{1-x}Sr_xCrO_3$ ($x = 0$, 0.05 and 0.15) at various temperatures.

	10K	50K	125K(250K)	r.t.
$LaCrO_3$	G_x			paramag.
$La_{0.95}Sr_{0.05}CrO_3$	G_z	G_z	G_y (125K)	paramag.
$La_{0.85}Sr_{0.15}CrO_3$	G_z	G_z	G^* (250K)	paramag.

* The magnetic moment is directed to [111] of the rhombohedral unit cell.

2.4.11 Neutron Powder Diffraction Study of Ferroelectric Antiferromagnet YMn_2O_5

H. Kimura[1], Y. Noda[1], I. Kagomiya[2], K. Kohn[2], K. Oikawa[3], and Y. Morii[3]

[1] *Research Institute for Scientific Measurements, Tohoku University*
[2] *Department of Physics, Waseda University*
[3] *Advanced Science Research Center, Japan Atomic Energy Research Institute*

In manganites of RMn_2O_5 (R; rare-earth or Y) system, ferroelectric transitions ($\equiv T_{CE} \sim 35$ K) occur under the Néel state ($T_N \sim 45$ K), indicating the coexistence of ferroelectricity and antiferromagnetism due to a strong spin–lattice interaction. Furthermore, some compounds in this system show anomalous behavior below T_{CE}, where the spontaneous polarization has a large jump ($\equiv T_2$)[1]. However, no structural information associated with the phase transition around T_{CE} and T_2 have been reported yet in Xray- and neutron- diffraction studies. In the present work, we studied the structure below and above T_N for YMn_2O_5, which has simple properties comparing with the other rare-earth manganites.

The neutron powder diffraction experiments were performed at HRPD in JRR-3M. The diffraction patterns were taken at 60 K ($> T_N$) and 7 K ($< T_2$) with incident neutron wavelength 1.163 Å. Figure 1(a) and (b) show the results of Rietvelt analyses for the 60 K and 7 K data, respectively. Fitting result at 60 K well reproduces the observed powder pattern. The reliable factor for profile fit R_{wp} was 6.29 % and that for intensities R_I was 1.02 %. The obtained atomic positional parameters well agree with the other rare-earth compounds[2]. As for the data at 7 K, we have analyzed the data with the high temperature structure parameters at the moment so that magnetic and ferroelectric characters were not included. Since then all the reliable factors were worse than those at 60 K, particularly because the extra magnetic reflections due to Néel order were observed at low-Q region (Figure 1(c)). It was cleared recently by our measurements of the YMn_2O_5 single crystal that the magnetic ordering has an incommensurate propagation wave vector $Q_{AF} \sim (1/2+\delta\ 0\ t)$ with $\delta \sim 0, t \sim 0.28$. No extra reflections suggesting structural change were found from the powder pattern taken at 7 K. In order to clarify the detailed magnetic and lattice structure at the lowest temperature phase, neutron- and Xray-diffraction studies by using single crystals are required.

References

[1] K. Kohn and I. Kagomiya, (in Japanese)
Cryst. Soc. Jpn. **41**, 342 (1999).

[2] J. A. Alonso *et al.*, J. Phys. Cond. Matt.
8515 (1997).

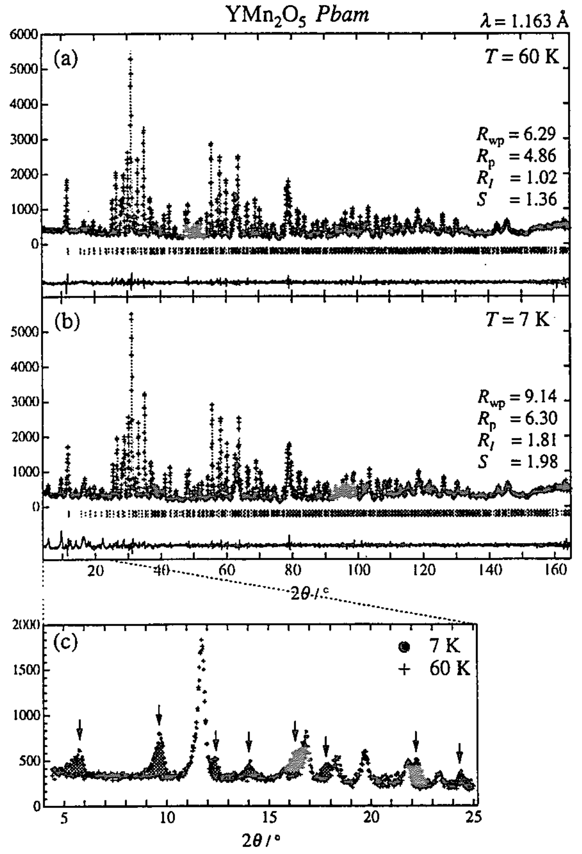

Figure 1: (a) and (b); Observed and calculated diffraction profiles at 60 K and 7 K, respectively. (c); Detailed diffraction patterns of low-Q region at 7 K (gray circle) and 60 K (cross). Hatched peaks indicate magnetic Bragg reflections.

2.4.12 NEUTRON DIFFRACTION STUDY AT 10K OF THE SPINEL COMPOUND $Co_{0.8}Mn_{0.2}Al_{1.6}Fe_2O_4$

S. M. Yunus[1], F. U. Ahmed[1,2]

[1] Institute of Nuclear Science and Technology, Atomic Energy Research Establishment, PO Box 3787,
Dhaka 1000, Bangladesh. e-mail: inst@bangla.net, aere@bangla.net
[2] ASRC, Japan Atomic Energy Research Institute, Tokai, Ibaraki 319-1195, Japan.

In spinel oxides there are two sublattices namely tetrahedral or A site and octahedral or B site. The interaction between the magnetic moments of ions in A and B sites takes place via the neighboring anions (oxygen ions) in the super-exchange mechanism. The two intra-sublattice interactions J_{AA} and J_{BB} are much weaker than the inter-sublattice interaction J_{AB}. Therefore, the inter-sublattice interaction dominates over the intra-sublattice interaction resulting into anti-parallel alignments of the moment of one sublattice to that of the other. Thus, there are unsatisfied bonds in the ferrimagnetic phase and with the introduction of nonmagnetic impurities a competition arises between the various exchange interactions which gives rise to a variety of magnetic behavior. Changing the concentration of magnetic ions in different sublattices by introducing nonmagnetic atoms one can induce interesting magnetic properties in spinel oxides [1-3]. In the present work we have studied magnetic properties of one such diluted spinel oxide sample $Co_{0.8}Mn_{0.2}Al_{1.6}Fe_2O_4$ at a temperature of 10K.

Neutron diffraction data from the sample have been collected at the JRR-3M reactor of JAERI using the High resolution Powder Diffractometer (HRPD). A neutron wavelength of 1.16Å reflected from a Si (5 3 3) monochromator set at an angle 89 deg. was used in the experiment. For this measurement a close circuit refrigerator was used to maintain the sample temperature at 10K. From our previous works on the spinel compound $Co_{0.8}Mn_{0.2}Al_{1.6}Fe_2O_4$ [4] we found a diffuse signal below the (111) Bragg diffraction peak. This signal arose at about 200K and showed a general trend of enhancement with the lowering of temperature up to 15K. We suggested that this diffuse signal was an indication of the formation of magnetic spin clusters and the evolution of the diffuse signal with lowering of temperature was due to the freezing of this clusters. The principal aim of the present work was to find how this diffuse signal behave at further low temperature. Fig. 1 shows the diffraction pattern limited to low-Q region taken at 10K. It is seen from the figure that the diffuse signal around (111) Bragg reflection is also present in this diffraction pattern. The diffuse signal appears to be rather stronger in this case than it was in the previous patterns taken up to 15K [4]. This means that at this temperature the magnetic spin clusters which are frozen in random directions, have been enhanced considerably. This feature provides a further support to our previous conclusion of a semi-spin glass transition at low temperature for this sample.

References

[1] Kanul B. Modi, V. T. Thanki and H. H. Joshi, Indian J. Phys., **70A** (4), 497, (1996).
[2] K. Muraleedharan, J. K. Srivastava, V. R. Marathe and R. Vijayaraghavan, J. Magn. Magn. Mater., **54-57**, 66, (1986).

[3] R. V. Upadhyay, R. B. Jotania and R. G. Kulkarni, Physica B **190**, 183, (1993).

[4] S. M. Yunus, J. A. Fernandez-Baca, M. A. Asgar and F. U. Ahmed, J. Alloys and Comp., **298**, 9, (2000).

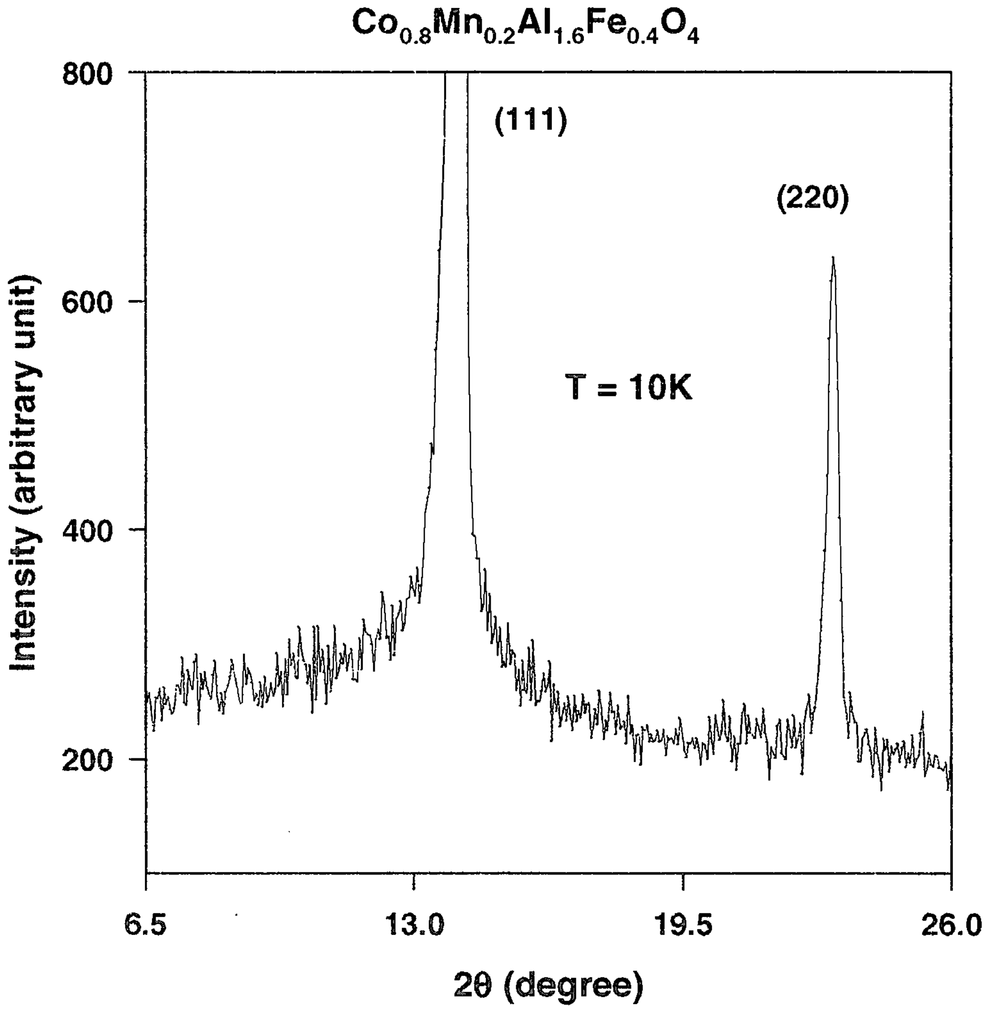

Fig. 1 Neutron diffraction pattern limited to low scattering angle of the spinel oxide sample $Co_{0.8}Mn_{0.2}Al_{1.6}Fe_2O_4$ taken at 10K with λ = 1.16 A.

2.5 Structural Physics

2.5.1 Lattice Dynamics of Lithium Oxide

Yoshinobu ISHII and Yukio MORII

Advanced Science Research Center, Japan Atomic Energy Research Institute
Tokai-mura, Naka-Gun, Ibaraki 319-1195, Japan

To clarify the fundamental properties of lithium oxide (Li_2O), measurements of phonon dispersion relations of Li_2O are very significant. The sample used in this measurements was a single crystal of $^7Li_2O$ and experiments were mainly carried out by the TAS-1 spectrometer installed at JRR-3M in JAERI. Measurements were conducted with fixed incident neutron energy by a constant-q method at 293 K and 700 K.

Figure 1 shows the phonon dispersion relations of Li_2O along three principal crystallographic axes. The open and solid circles indicate the transverse and longitudinal modes, respectively.

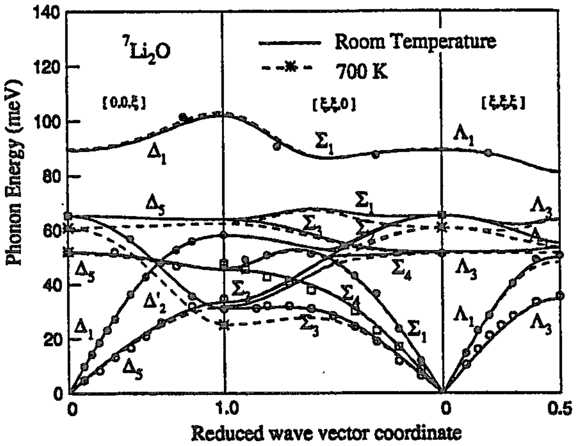

Fig.1. Phonon dispersion relations of Li_2O at 293 K and 700 K. Solid and broken lines indicate the calculated dispersion relations at 293 K and 700 K, respectively.

The motion of the ion is as follows in a matrix form$^{1)}$

$$M\omega^2 U = (R + ZCZ)U + (T + ZCY)W,$$
$$0 = (\widetilde{T} + YCZ)U + (\vartheta + YCY)W.$$

The notations for the matrices in above equations are the same as defined by Cowley et al.$^{1)}$ The force constants acting between ions are as follows

$$\frac{e^2 A_i}{v} = \left(\frac{\partial^2 V}{\partial r^2}\right) \quad and \quad \frac{e^2 B_i}{v} = \left(\frac{1}{r}\frac{\partial V}{\partial r}\right).$$

We calculate the force constants using all measured data by a best fitting method. Obtained phonon dispersion relations are shown in Fig.1 by solid lines and the force constants are listed in Table 1. In this table the Farley's results are also listed as a reference.

TableI. Force constant of Li_2O at 293 K.

Force constant		Unit	Farley, *et al.*$^{29)}$	Present Cal.
O – Li^1	A_1	e^2/V_a	11.97	11.43_7
	B_1	e^2/V_a	-1.46	-1.34_1
Li^1 – Li^2	A_2	e^2/V_a	-0.25	0.16_8
	B_2	e^2/V_a	-0.09	-0.05_0
O – O	A_3	e^2/V_a	-0.89	0.03_0
	B_3	e^2/V_a	-0.05	-0.05_4
Li^1 – Li^1, Li^2 – Li^2	A_4	e^2/V_a	0.15	0.09_1
	B_4	e^2/V_a	-0.08	0.04_8
O	Z_o	e	-2.0*	-1.90
Li	Z_{Li}	e	1.0*	0.95
O	α_o	10^{-30} m	2.46	2.39_8
	d_o	e	-0.76	0.71_7
Li	α_{Li}	10^{-30} m	-0.05	0.00_2
	d_{Li}	e	0.02	0.00_1

A frequency distribution for Li_2O was calculated using a mesh of 744299 q-vectors in the reducible 1/48 volume of the first Brillouin zone. The frequency distribution is shown in Fig.2 as a histogram.

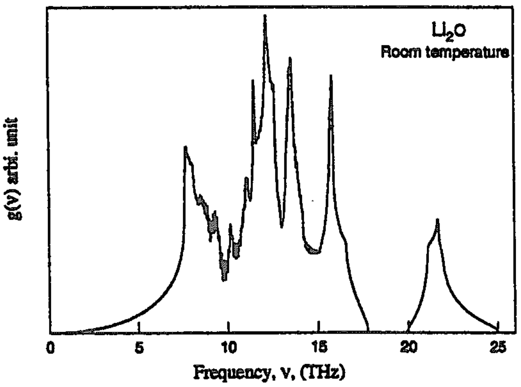

Fig.2. Frequency distribution of Li_2O at 293 K.

From this measurement, we obtained some fundamental knowledge for Li_2O and found that phonon energies for the Δ_2' mode drastically decreased with increasing temperature.

---

1) R.A. Cowley, W. Cochan, B.N.Brockhouse and A.D.B Woods, Phys. Rev. **131** (1963) 1020.
2) T.W.D. Farley, H. Hayes, S. Hull, R. Ward, M.T. Huchings and M. Alba, Solid State Ionics **28-30** (1988) 189.

2.5.2

Structural Investigation of Nanocrystalline Silicon by Small-Angle Scattering

J. Suzuki[1], T. Matsumoto[2], Y. Masumoto[2], and M. Ohnuma[3]

[1]Advanced Science Research Center, JAERI, Tokai 319-1195, Japan
[2]Single Quantum Dot Project, ERATO, Japan Science and Technology Corporation,
Tsukuba 300-2635, Japan
[3]National Research Institute for Metals Tsukuba 305-0047, Japan

Nanocrystalline porous silicon fabricated by electrochemical anodization has attracted much interest because it exhibits strong photoluminescence (PL) at room temperature [1,2]. Although a great deal of effort has been made to elucidate the origin of the PL, much uncertainty still remains due to the difficulty of physical characterization of silicon nanostructures.

We studied the nanostructures of porous silicon using small-angle scattering. Figure 1 shows scattering intensities $I(q)$ obtained from silicon nanocrystals with the porosity of p = 0.63, 0.79, and 0.87. The scattering profiles give qualitatively similar features and they can be divided into two q regions characterized by clear humps around 0.1 nm^{-1}. In the lower q region the scattering intensities gradually increase toward 0 nm^{-1}, which indicates that silicon nanocystals correlate with each other. In the higher q region, the scattering intensities obey the Porod law, *i.e.*, $I(q) \propto q^{-4}$. This well-known q dependence implies that the interface between the silicon nanocrystal and the pore shows a sharp boundary like a step function. Furthermore, we observed the porosity dependence of the scattering intensity. The decrease of the scattering volume fraction with increasing the porosity leads to the reduction of the scattering intensity in the whole q region. However, the reduction is not uniform for the whole q region. Especially, in the lower q region, the reduction is remarkable. This result suggests that in the higher porosity sample the correlation between silicon nanocrystals becomes lost.

According to a correlating polydisperse hard spherical nanocrystalline model, we determined the size distribution of nanocrystals (Fig. 2). The size distribution shifts toward the smaller radius of the silicon nanocrystal with increasing the porosity. The mean radius become 1.8, 1.36, and 1.18 nm for the porosity of p = 0.63, 0.79, and 0.87, respectively. The size estimated here is much smaller than the values determined by the Raman scattering [3] but shows similar value determined by silicon K-edge X-ray absorption measurements [4]. We report the effect of nanocrystal size on the photoluminescence elsewhere.

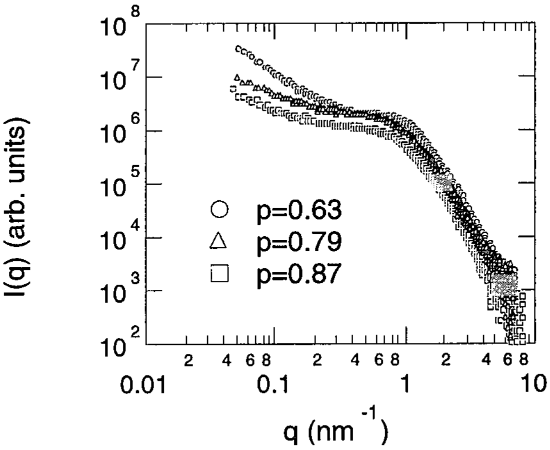

Fig. 1 Small-angle scattering from porous silicon.

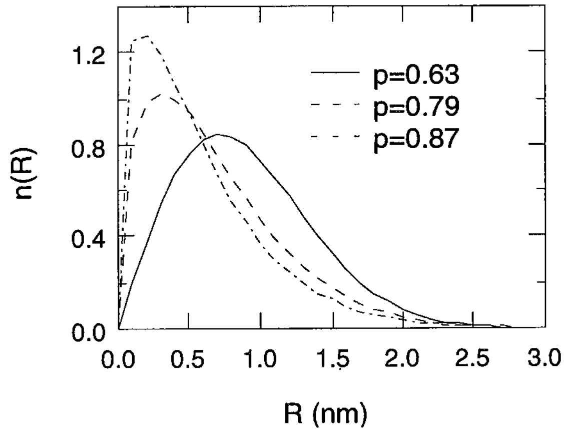

Fig. 2 Normalized size distribution function of nanocrystals in porous silicon samples.

References

[1] S. S. Iyer and Y. -H. Xie, Science **260** (1993) 40.

[2] Z. H. Lu, D. J. Lockwood, and J. –M. Baribeau, Nature **378** (1995) 258.

[3] Y. Kanemitsu, Phys. Reports 263 (1995) 15.

[4] S. Schuppler *et al.*, Phys. Rev. Lett. **72** (1994) 2648.

2.5.3 Neutron Powder Diffraction Study on Thermal Expansion of UGe_2

K. Oikawa*, M. Kohgi[1], H. Sagayama[1], K. Kuwahara[1], Y. Shimojyo, Y. Morii and Y. Onuki

Advanced Science Research Center, Japan Atomic Energy Research Institute, Tokai, Ibaraki 319-1195
[1] Tokyo Metropolitan University, Hachioji, Tokyo 192-0397
* Present address: National Institute of Materials and Chemical Research, 1-1 Higashi, Tsukuba, Ibaraki 305-8565

A heavy fermion compound, UGe_2 shows highly anisotropic ferromagnetism with Curie temperature, T_c = 52 K[1)]. Crystal structure of UGe_2 is isomorphic with the orthorhombic $ThGe_2$[2, 3)], and uranium magnetic moment as large as 1.4 μ_B aligned along the *a*-axis.

Oomi et al.[4)] measured thermal expansion of a single-crystalline UGe_2 by using a strain gauge, and showed anomalies at T_c and T' (≈ 25 K). The former is due to magnetostriction, but the origin of the later was not clarified. Kohgi et al.[5)] measured thermal expansion of a single-crystalline UGe_2 with a capacitance bridge. The resultant values were, however, not coincident with Oomi's result, especially in the behavior of the *a*-axis.

To study the thermal expansion, Rietveld refinement of high-resolution neutron powder diffraction has several advantages, because

i) lattice constants can be obtained simultaneously,
ii) magnetic moment can be estimated,
iii) in addition, other structural parameters can be obtained.

On the other hand, disadvantages as compared with strain gauge method are that

iv) relative precision is worse,
v) temperature fluctuation and uniformity of the sample are not negligible, and
vi) a target material is restricted by the diffracted intensity.

In this work, we studied the anomalies in thermal expansion due to magnetostriction in UGe_2 using high-resolution neutron powder diffraction and compare the results with previous studies.

Neutron powder diffraction data were collected every 5 K from 10 K to 110 K and every 10 K from 110 K to 300 K. The 40 diffraction data were analyzed by the Rietveld refinement program RIETAN. The obtained lattice constants were fitted by Grueneisen-Einstein function between 55 K and 300 K, and the calculated line was extrapolated to 10 K. Figure 1a shows refined lattice parameters (lower), and resultant thermal expansion coefficients, $\alpha = \frac{1}{l}\frac{\Delta l}{\Delta T}$ (upper), of *a*-axis as a function of temperature. Figure 1b and 1c shows those of *b*- and *c*-axis, respectively.

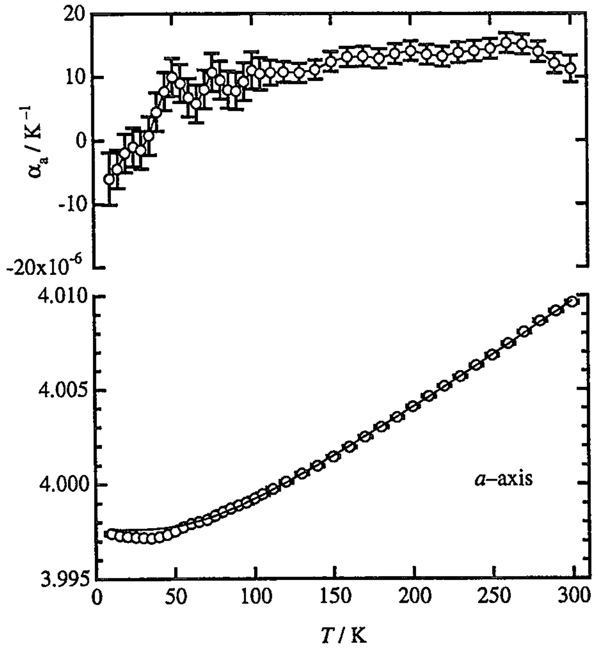

Fig. 1a. Temperature variation of the thermal expansion coefficient and the lattice constant (Å) along the *a*-axis.

The thermal expansion coefficients shows some spurious roughness around 80 K, but the behavior of the coefficients of *a*-axis under T_c is similar to Oomi's result. These spurious humps would come from limitation of the precision and the accuracy of the refined lattice prameters and its standard deviations. Typical values concerned with α in this region were, for example, l = 4.00000(6) Å, Δl = 16(8)×10^{-5}, ΔT = 5.0(5), thus deviation of Δl was worst. The relative deviation of Δl will be negligible if the temperature interval (which depends on the steepness of the variation of the phenomena) could be chosen to be large.

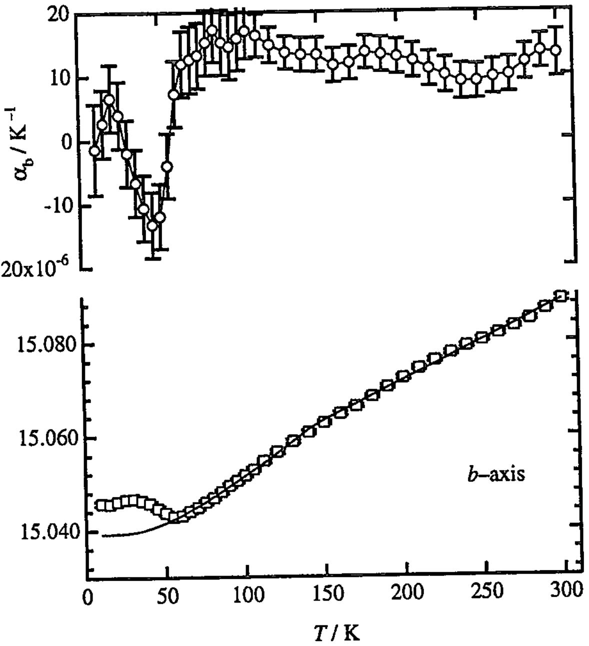

Fig. 1b. Temperature variation of the thermal expansion coefficient and the lattice constant (Å) along the b-axis

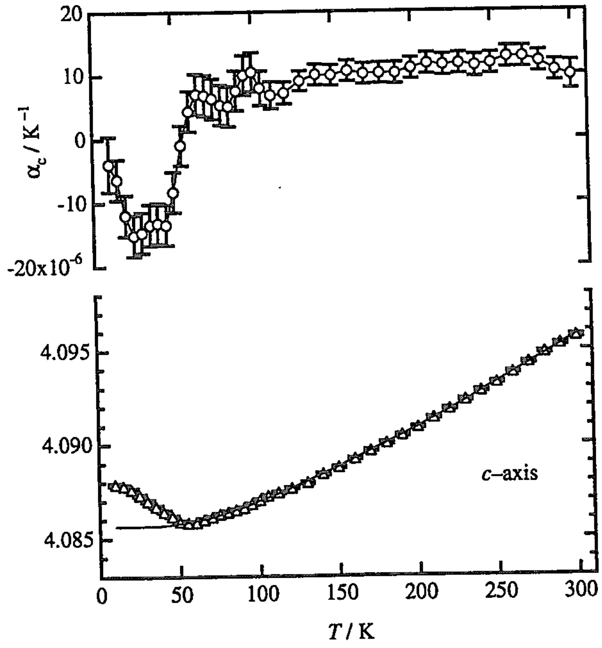

Fig. 1c. Temperature variation of the thermal expansion coefficient and the lattice constant (Å) along the c-axis

Figure 2 shows temperature dependence of refined magnetic moment. The value is much larger than reported value of 1.4 μ_B, but it would be attributed to that preferred orientation correction does not correct the magnetic component. The quantitative analysis between spontaneous magnetization and anomalies in thermal expansion under 55 K is in progress.

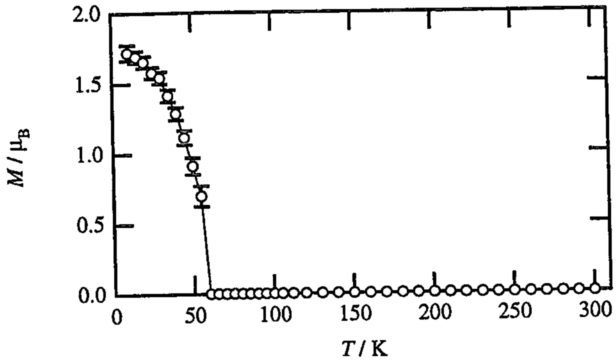

Fig. 2. Calculated ferromagnetic moment of Uranium, assuming magnetic formfactors of U^{3+}.

In conclusion, we showed that Rietveld refinement using high-resolution neutron powder diffraction is available for work on thermal expansion, and the temperature interval should be properly chosen to achieve reliable results.

References

1) Y. Onuki, I. Ukon, S. W. Yun, I. Umehara, K. Satoh, T. Fukuhara, H. Sato, S. Takayanagi, S. Shikama and A. Ochiai: J. Phys. Soc. Jpn. 61, (1992) 293.
2) K. Oikawa, T. Kamiyama, H. Asano, Y. Onuki and M. Kohgi: J. Phys. Soc. Jpn. 65, (1996) 3229.
3) P. Boulet, A. Daoudi, M. Potel, H. Noel, G. M. Gross, G. Andre and F. Bouree: J. Alloys Compd. 247, (1997) 104.
4) G. Oomi, K. Nishimura, Y. Onuki and S. W. Yun: Physica. B 186-188, (1993) 758.
5) T. Inamura, M. Kohgi, K. Iwasa, Y. Haga and Y. Onuki: Autumn Meeting of the Phys. Soc. Jpn. Abstract 25a-PS-12 (1998).

2.5.4 Structural Study of High Ionic Conductor $Rb_4Cu_{16}I_{7.2}Cl_{12.8}$

K. Oikawa*, T. Kamiyama[1], T. Ikeda[2], R. Kanno[3], T. Hata[3], F. Izumi[2], Y. Shimojyo and Y. Morii

Advanced Science Research Center, Japan Atomic Energy Research Institute, Tokai, Ibaraki 319-1195
[1] Institute of Materials Structure Science, High Energy Accelerator Research Organization, Tsukuba, Ibaraki 305-0801
[2] National Institute for Research in Inorganic Materials, 1-1 Namiki, Tsukuba, Ibaraki 300-0047
[3] Department of Chemistry, Faculty of Science, Kobe University, Nada, Kobe, Hyogo, 657-8501
* Present address: National Institute of Materials and Chemical Research, 1-1 Higashi, Tsukuba, Ibaraki 305-8565

The high ionic conductor $Rb_4Cu_{16}I_7Cl_{13}$ has a room-temperature conductivity of 0.34 S/cm, which is the highest conductivity value of the ionic conductors so far prepared. The crystallographic study on the transition from a normal conduction state to a high conduction state at around 200 K is of particular importance for understanding the conduction mechanism of high ionic conductors. Geller et al.[1)] have determined the crystal structure of $RbCu_4I_2Cl_3$ ($Rb_4Cu_{16}I_8Cl_{12}$) at room temperature by single-crystal X-ray diffraction. Kanno et al.[2)] studied the structural changes of $Rb_4Cu_{16}I_{7.2}Cl_{12.8}$ using time-of-flight neutron powder diffraction at low temperatures. Their results are summarized as follows; no structural phase transition was detected, and a gradual migration of copper ions from the Cu(3) 'nonconducting' site into the Cu(2) 'conducting' site. However, their neutron diffraction study seems to be somewhat uncertain because the Rietveld refinements were carried out without reflections at large-*d* region (*d*-spacing > 3.4 Å) which are important for determination of the occupation factors.

In this study, we reinvestigate the structural change of $Rb_4Cu_{16}I_{7.2}Cl_{12.8}$ using angle dispersive neutron powder diffraction at low temperatures. The incident wavelength of 1.16 Å was chosen to collect as many reflections as possible, including lowest index. Figure 1 and 2 show temperature dependence of occupation factors × multiplicity and isotropic thermal displacement parameters of Cu sites, respectively. The isotropic thermal displacement parameters of Cu(3) site were converged to be larger than those of Kanno's, but the parameters were found to be strongly correlated with occupation factors of this site. The nuclear density distribution analysis using Maximum Entropy Method is in progress.

References

1) S. Geller, J. R. Akridge and S. A. Wilber, Phys. Rev. 19, 5396 (1993)
2) R. Kanno, K. Ohno, Y. Kawamoto, Y. Takeda, O. Yamamoto, T. Kamiyama, H. Asano, F. Izumi and S. Kondo, J. Solid State Chem. 102, 79 (1993)

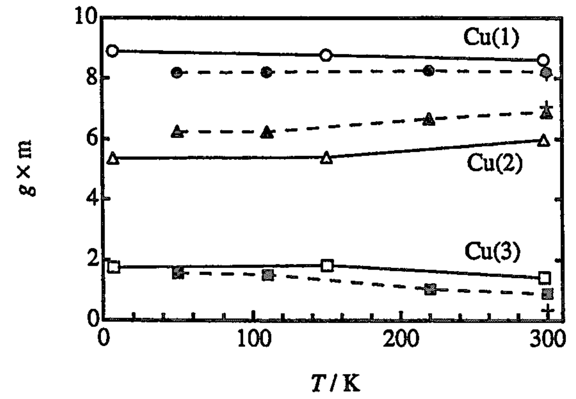

Fig. 1. Temperature dependence of occupation factor × multiplicity of each Cu(1), Cu(2) and Cu(3) sites: open marks; this work, closed; Kanno et al. and +; Geller et al.

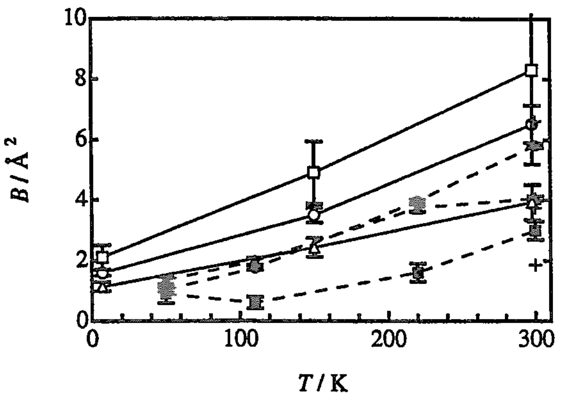

Fig. 2. Temperature dependence of the isotropic thermal displacement parameters of Cu(1), Cu(2) and Cu(3) sites. Marks are the same as in Fig. 1.

2.5.5 Crystal Structure of Charge Ordering State of $CuIr_2S_4$

K. Oikawa*, T. Matsumoto[1], T. Furubayashi[1], N. Matsumoto[2], S. Nagata[2], Y. Shimojyo and Y. Morii

Advanced Science Research Center, Japan Atomic Energy Research Institute, Tokai, Ibaraki 319-1195
[1] National Research Institute for Metals, Tsukuba, Ibaraki 300-0047
[2] Department of Materials Science and Engineering, Muroran Institute of Technology, Mizumoto-cho, Muroran, 50-8585
* Present address: National Institute of Materials and Chemical Research, 1-1 Higashi, Tsukuba, Ibaraki 305-8565

The thiospinel compound $CuIr_2S_4$ exhibits a metal-insulator transition accompanied by a structural transition at T_{MI} ~ 230 K¹⁾. Superlattice reflections below T_{MI} were previously reported by the X-ray powder diffraction¹⁾ and the electron diffraction²⁾. A triclinic unit cell was recently proposed from the analysis of the high-resolution synchrotron powder diffraction at 50 K³⁾. The details of the crystal structure at the low temperature (LT) phase, however, have not been clarified yet.

In this work, the crystal structure of the LT phase of $CuIr_2S_4$ was studied by neutron powder diffraction on HRPD. Two wavelengths were selected for the present study; the wavelength λ = 1.82299 Å (Ge 331 monochromator) was employed in order to obtain higher Q-resolution, and the wavelength λ = 1.16379 Å (Si 533 monochromator) was used to obtain precise structural parameters. The diffraction data taken at 50 K were analyzed on the basis of the triclinic unit cell (space group $P\bar{1}$) with lattice parameters a = 13.979(2), b = 11.954(2), c = 6.9880(5) Å, α = 91.1267(6), β = 88.201(5) and γ = 125.764(7)°. Figure 1 shows Rietveld refinement patterns of $CuIr_2S_4$ at 50 K. The possible ordered ionic configurations of Ir^{3+} and Ir^{4+}, which are deduced by calculating $[IrO_6]$ octahedral volumes, were consistent with the magnetic properties¹⁾.

References

1) T. Furubayashi, T. Matsumoto, T. Hagino and S. Nagata, J. Phys. Sci. Jpn., **63** (1994) 3333.
2) H. Ishibashi, K. Tanioka, R. Oshima and K. Nakahigashi, Annual Meeting of the Phys. Soc. Jpn. Abstract 1p-YL-13 (1998).
3) H. Ishibashi, T. Sakai, R. Oshima and K. Nakahigashi, Autumn Meeting of the Phys. Soc. Jpn. Abstract 24aPS-92 (1999).

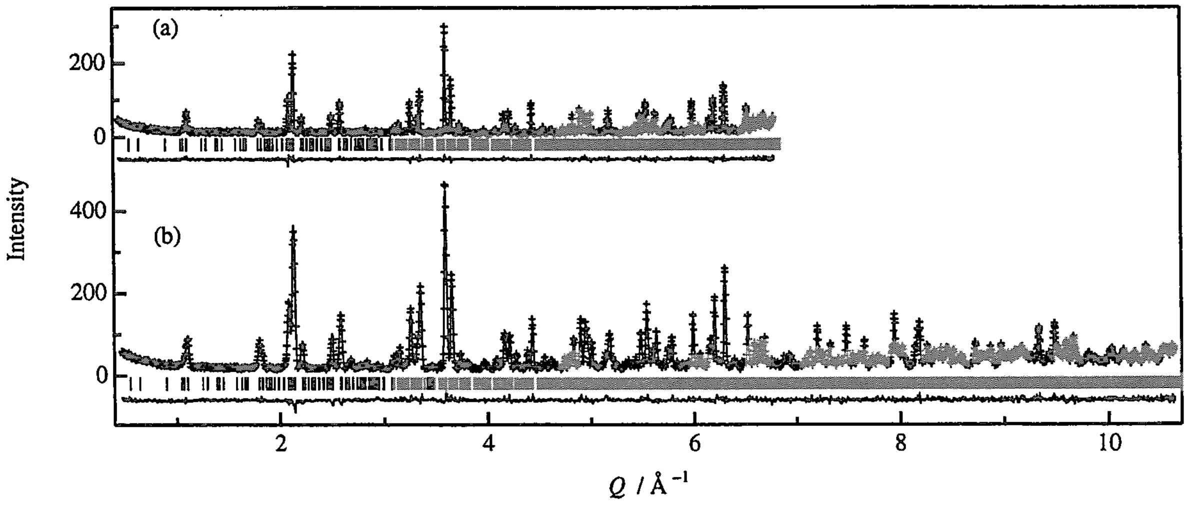

Fig. 1. Rietveld refinement patterns of $CuIr_2S_4$ at 50 K; (a) λ = 1.82299 Å, (b) λ = 1.16379 Å.

2.5.6 Structural Phase Transition of Orthorhombic $LaCrO_3$

K. Oikawa*, T. Kamiyama[1], T. Hashimoto[2], Y. Shimojyo and Y. Morii

Advanced Science Research Center, Japan Atomic Energy Research Institute, Tokai, Ibaraki 319-1195
[1] Institute of Materials Structure Science, High Energy Accelerator Research Organization, Tsukuba, Ibaraki 305-0801
[2] Department of Applied Physics, College of Humanities and Sciences, Nihon University, Setagaya-ku, Tokyo 156-8550
* Present address: National Institute of Materials and Chemical Research, 1-1 Higashi, Tsukuba, Ibaraki 305-8565

$LaCrO_3$ and related oxides have been studied widely aiming at various industrial uses above room temperature (RT): for example, interconnects in solid-oxide fuel cells. It is well known that stoichiometric $LaCrO_3$ has phase transitions at around T = 15 and 260°C. The former is due to a magnetic order-disorder transition, while the latter to a structural phase transition, i.e., from an orthorhombic to a rhombohedral symmetry. Although the physical properties such as heat capacity and thermal conductivity of $LaCrO_3$–based perovskites at high temperatures have been measured widely, the crystal structure above room temperature has not been examined precisely.

By use of X-ray powder diffraction at high temperatures, several workers reported that $LaCrO_3$ showed the volume contraction at the structural phase transition. However, it remains open whether the large volume contraction arises from the deformation of $[LaO_{12}]$ and/or $[CrO_6]$ polyhedra. Then we carried out neutron diffraction experiments on $LaCrO_3$ at high temperatures and studied the structural phase transition from an orthorhombic to a rhombohedral phase. A geometrical relationship between polyhedral volumes and their tilts in perovskites developed by Thomas (1-3) was utilized to deduce polyhedral volume changes at the phase transition.

Neutron powder diffraction experiments were carried out on HRPD from RT to 740 °C with a high-temperature furnace. The sample was contained in a V holder. The temperature was monitored by a Chromel-Alumel thermocouple and was kept within ±0.5 K during the measurement. Two different wavelengths were selected depending on the requirement for the present study. The elastically-bent Si (533) monochromator which gives wavelength of 1.16251 Å was mainly used to obtain detailed structural information for the orthorhombic phase. The hot-pressed Ge (331) monochromator which gives 1.82340 Å was employed at around the phase transition region in order to obtain higher Q-resolution and at high temperature region. The 30 diffraction data were analyzed by the Rietveld method with RIETAN. Typical R_{WP} and R_B were ca. 7 % and 3 % respectively. The coefficients of volume thermal expansion, $\frac{1}{V}\frac{\partial V}{\partial T}$, were estimated as $2.285(16) \times 10^{-5}$ K^{-1} (between T = 295 K and T = 533 K) and $2.842(12) \times 10^{-5}$ K^{-1} (between T = 533 K and T = 1013 K) for the orthorhombic and rhombohedral phases, respectively. The volume contraction at the phase transition was calculated to be about –0.138%, which is very close to the values reported by Sakai et al (4).

The relationship between polyhedral volumes and their shapes in orthorhombic and rhombohedral perovskites ABO_3 were discussed by Thomas. For orthorhombic perovskites, the volume of the $[AO_{12}]$ polyhedron, V_A, that of the $[BO_6]$ polyhedron, V_B, and their ratio V_A/V_B are given by

$$V_B = \frac{s_1 s_2 s_3}{6},$$

$$\frac{V_A}{V_B} = 6\cos^2\theta_m \cos\theta_z - 1,$$

where s_1, s_2 and s_3 are distances between diagonal vertices of an octahedron, and θ_m and θ_z the tilt angles of the $[BO_6]$ octahedra along [101] and [010] direction of the present setting, respectively.

For rhombohedral perovskites, V_A, V_B, V_A/V_B and octahedral tilt angle, ω, are given by

$$V_B = \frac{\sqrt{3}cs^2}{18},$$

$$V_A = \frac{\sqrt{3}a^2c}{12} - \frac{\sqrt{3}cs^2}{18},$$

$$\cos\omega = \frac{a}{2s} \text{ and}$$

$$\frac{V_A}{V_B} = 6\cos^2\omega - 1,$$

where a and c are the lattice constants in the hexagonal unit cell, and s the edge length of the $[BO_6]$ octahedra. From these equations given by Thomas et al., V_A, V_B and V_A/V_B for both the orthorhombic and rhombohedral phases were calculated and plotted in Fig. 1. We can clearly see the shrinking of V_B at the phase transition and almost linear expansion of V_A at whole temperature range. This figure unambiguously reveals that the volume contraction at the phase transition principally results from the shrinking of the $[BO_6]$ polyhedron.

Thomas introduced a parameter Φ to combine θ_m and θ_z in orthorhombic structure:

$$\Phi = 1 - \cos^2\theta_m \cos\theta_z.$$

Using Φ, V_A/V_B can be simply written as

$$\frac{V_A}{V_B} = 5 - 6\Phi.$$

In order to extend Φ to the rhombohedral structure and to study the characteristics of the phase transition in the present system, the degree of tilt in rhombohedral structure is expressed as

$$\Phi = 1 - \cos^2\omega.$$

Using Φ, V_A/V_B is similarly written as

$$\frac{V_A}{V_B} = 5 - 6\Phi.$$

V_A/V_B of both orthorhombic and rhombohedral phases in $LaCrO_3$ is plotted as a function of Φ in Fig. 2. V_A/V_B of various known samples having orthorhombic (space group Pnma) and rhombohedral (space group $R\bar{3}c$) structure are also included in the figure. The rhombohedral samples tend to have smaller tilts Φ and larger V_A/V_B values. It is emphasized in the case of $LaCrO_3$ that Φ decreases as the phase transition from the orthorhombic to rhombohedral proceeds, and its phase boundary is located near the limit of the reference values of rhombohedral samples.

It is curious that the $[BO_6]$ polyhedron contracts instead of the $[AO_{12}]$ polyhedron, because the V_B is much tighter than V_A. The same kind of contraction would occur in the structural phase transition of $La(Co_{1-t}Cr_t)O_3$, $(La_{1-t}A_t)CrO_3$ (A = Ca or Sr) system. Further investigations are required to clarify the origin of the V_B contraction.

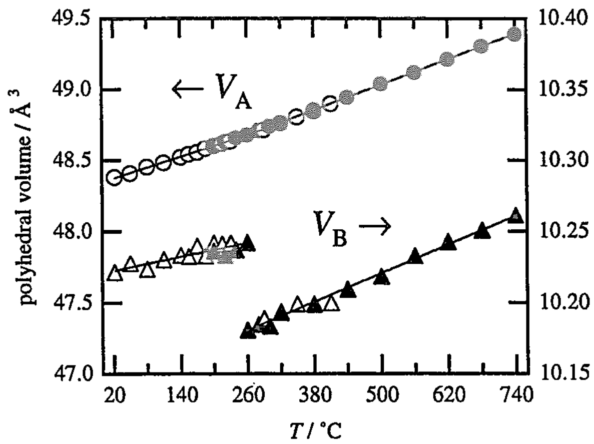

Fig. 1. Temperature variation of the volume of the $[LaO_{12}]$ polyhedron: V_A, and of the $[CrO_6]$ polyhedron: V_B. Circles and triangles express the volume for the orthorhombic and the rhombohedral phases respectively. Data points obtained from experiments with wavelength of 1.82340 Å are represented by filled symbols.

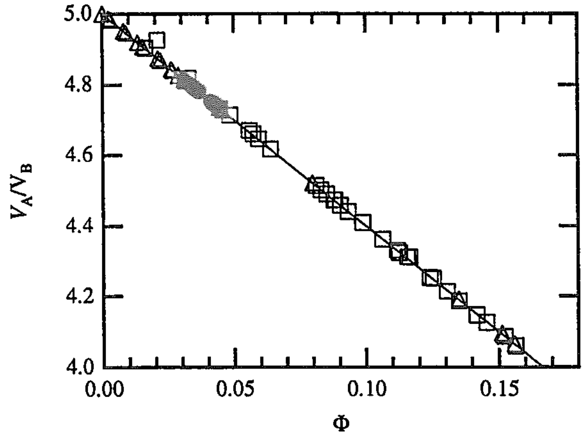

Fig. 2. Variation of V_A/V_B of $LaCrO_3$ with degree of tilt Φ (circles). Triangles and squares represent that of rhombohedral and orthorhombic structure.

References

1) N. W. Thomas and A. Beitollahi: *Acta Crystallogr.* B 50, (1994) 549.
2) N. W. Thomas: *Acta Crystallogr.* B 52, (1996) 16.
3) N. W. Thomas: *Acta Crystallogr.* B 52, (1996) 954.
4) N. Sakai, H. Fjellvag and B. C. Hauback: *J. Solid State Chem.*, 121 (1996) 202.

2.5.7 Structures of layered superconductor, $Li_{0.18}ZrNBr$, and the parent compound ß-ZrNBr

S. Shamoto[1], Y. Kato[1], K. Oikawa[2], T. Kajitani[1]
[1] *Department of Applied Physics, Faculty of Engineering, Tohoku University, Sendai 980-8579*
[2] *Advanced Science Research Center, Japan Atomic Energy Research Institute, Tokai-mura, 319-1195*

One of the novel honeycomb lattice superconductors, $Li_{0.18}ZrNBr$, and the parent compound, β-ZrNBr, have been studied from a structural point of view by means of Rietveld analysis technique using powder neutron diffraction data with the incident wave length of 1.1636 Å at T=8 K. In the ZrNBr-system, the sliding of $[ZrNBr]_2$ blocks by Li intercalation has not taken place unlike the other isostructual compounds, such as A_xHfNCl or A_xZrNCl (A; alkali metals) [1,2]. Structural parameters of ß-ZrNBr and $Li_{0.18}ZrNBr$ are shown in Table I. The ratio of electronic density of states for three superconductors, $Li_{0.18}ZrNBr$, $Li_{0.16}ZrNCl$, and $Na_{0.29}HfNCl$, has been estimated to be 1.00:1.05:1.23 from each bond length between the nearest neighbor transition metals. The ratio corresponds well to their superconducting transition temperatures, i.e., 12.6 K, 15.0 K and 20.0 K, respectively. This could be explained in terms of the simple BCS theory, indicating the importance of electronic density of states in the present novel layered superconductors.

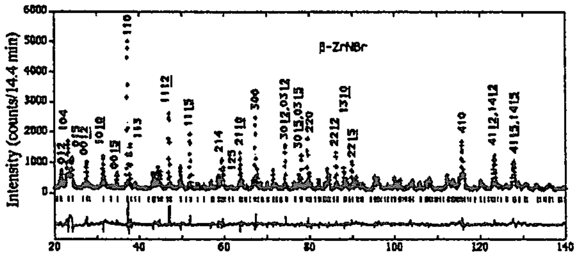

Fig. 1. Neutron diffraction pattern of ZrNBr.

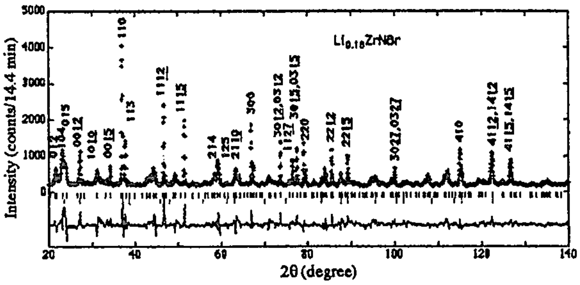

Fig. 2. Neutron diffraction pattern of $Li_{0.18}ZrNBr$.

Table I. Structural parameters, a. ß-ZrNBr, b. $Li_{0.18}ZrNBr$ [3].

a. $R\text{-}3m$; a=3.6341(2) Å, c=29.157(2) Å

atom	site	g	x	y	z
Zr	6c	1	0	0	0.12348(9)
N	6c	1(fixed)	0	0	0.19725(7)
Br	6c	1(fixed)	0	0	0.38847(9)

R_I=6.27%, R_p=10.88%, R_{wp}=13.69%, R_e=5.58%, B_{eq}^{all}=0.41(3) Å^2

b. $R\text{-}3m$; a=3.6504(3) Å, c=29.568(3) Å

atom	site	g	x	y	z
Zr	6c	1	0	0	0.1280(2)
N	6c	1(fixed)	0	0	0.2002(2)
Br	6c	1(fixed)	0	0	0.3882(2)
Li	3a	0.36(fixed)	0	0	0

R_I=12.32%, R_p=14.41%, R_{wp}=18.79%, R_e=5.58%, B_{eq}^{all}=0.03(5) Å^2

References

[1] S. Shamoto, T. Kato, Y. Ono, Y. Miyazaki, K. Ohoyama, M. Ohashi, Y. Yamaguchi and T. Kajitani, Physica C 306, 7 (1998).
[2] S. Shamoto, K. Iizawa, M. Yamada, K. Ohoyama, Y. Yamaguchi and T. Kajitani, J. Phys. Chem. Solids 60, 1431 (1999).
[3] S. Shamoto, Y. Kato, K. Oikawa and T. Kajitani, in preparation (ASR-2000).

2.5.8

Temperature dependence of the structure of liquid Sn: Neutron scattering experiment and an *ab initio* molecular-dynamics simulation

S. Munejiri, T. Masaki, T. Itami, Y. Senda[1], F. Shimojo[1], K. Hoshino[1], T. Kamiyama and Y. Ishii[2]

Space Development Agency of Japan (NASDA), 2-1-1 Sengen, Tsukuba 305-8505, Japan
[1]*Hiroshima University, Higashi-Hiroshima 739-8521, Japan*
[2]*Japan Atomic Energy Research Institute, Tokai, Ibaraki, 319-1195, Japan*

The measurements of the self-diffusion coefficient D of liquid tin for a wide range of temperature have been made under a microgravity environment and rather accurate data compared with those measured on the ground have been obtained owing to the absence of convection [1,2)]. Several models to try to explain the temperature dependence of D of liquid metals have been proposed so far. However, to clarify the mechanism of the self-diffusion and to construct a reliable model for a wide range of temperature, it is crucial not only to measure D accurately but also to understand the microscopic liquid structure.

It is known that though the structure factor $S(Q)$ of liquid tin has a shoulder on the high-Q side of the first peak near the melting point[3)], the shoulder becomes less clear with increasing temperature[4)]. Since the shoulder is probably related to a complex local structure, it is expected that the disappearance of the shoulder makes an effect on the diffusion mechanism. In this sense, the liquid tin is a suitable liquid to investigate the relation between the structure and the self-diffusion systematically. In this paper, to investigate a correlation between the microscopic structure and the self-diffusion of liquid tin for a wide range of temperature, we have performed a neutron scattering experiment and an *ab initio* molecular-dynamics (AIMD) simulation.

The neutron scattering measurements for liquid tin have been performed on JRR-3M, using the TAS-1 (2G) spectrometer. The data of scattering intensity were measured in a Q-range from 0.2 to 12.1 Å^{-1} with the steps 0.05 and 0.1 Å^{-1} for $Q < 6.0$ Å^{-1} and $Q > 6.0$ Å^{-1} , respectively at the temperatures of 573, 773 and 1073 K. For almost whole Q region, $0.5 < Q < 10.3$ Å^{-1} the wavelength 0.95 Å was used and the data at high and low angle regions were obtained with the wavelengths of 0.85 and 2.44 Å, respectively. The sample was sealed in a thin quartz glass tube, 8.0 mm inner diameter with 0.3 mm thickness and 30 mm height. The accumulated counts of scattering intensity were of the order of 10^4 and those of empty quartz glass cell were about 10^3.

The AIMD was performed using the supercomputer VPP500 at the Center for Promotion of Computational Science and Engineering(CCSE). Our method of the AIMD calculation[5)] is based on density functional theory with the local density approximation. The norm-conserving pseudopotential by Troullier and Martins was employed for the interaction between valence and core electrons. The MD simulation was carried out with 64 atoms from 773 to 1473 K with Nosé-Hoover thermostat.

In Fig.1, the data of $S(Q)$ obtained in the present study from 573 to 1473 K are shown. The solid and circles show the results obtained from AIMD simulation and from the neutron scattering, respectively. The calculated results are in excellent agreement with the experiments. In both the calculated and the experimental $S(Q)$, the shoulders are observed clearly at high-Q side of main peak, around $Q = 2.8$ Å^{-1} at low temperatures. With increasing temperature, the first peak becomes

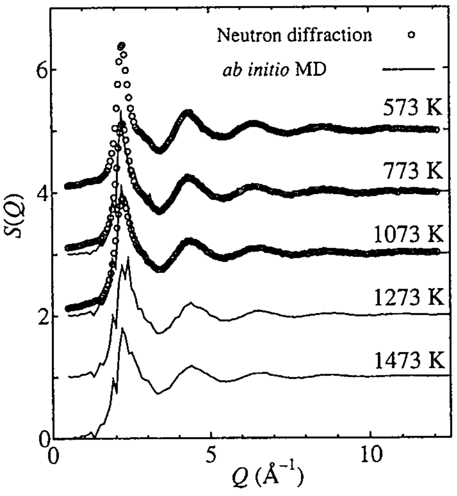

Fig 1: Structure factors pf liquid tin from 523 to 1473 K.

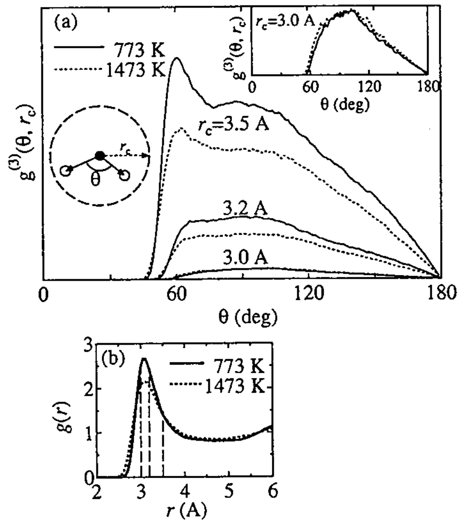

Fig 2: Bond angle distribution functions (a) and Radial distribution functions (b).

lower and broader and the shoulder seems to disappear. However since the values of $S(Q)$ around the shoulder stay almost constant and even at highest temperature 1473 K the shape of the first peak in $S(Q)$ is unsymmetrical, it is considered that at high temperature the shoulder dose not disappear but is merely covered by the broadened first peak. From these results we conclude that the some local structures still remain at 1473 K in the liquid tin.

To study the microscopic structure more detail, we calculated bond angle distribution functions from the atomic configuration obtained by the AIMD simulation; the bond angle is formed by a pair of vectors drawn from a reference atom to any other two atoms within a cutoff radius r_c. In Fig.2(a) the result of the bond angle distribution functions $g^{(3)}(\theta, r_c)$ at 773 and 1473 K are shown. When the cutoff radius r_c is 3.0 Å, which is shorter than the average nearest neighbor distance, $g^{(3)}(\theta, r_c)$ shows one broad peak centered at 100°. This peak suggests that some fragments of a tetrahedral structure persist in a short period even in the liquid state. With increasing the cutoff radius r_c, a new peak appears around 60°. Since when an interatomic interaction is isotropic and the atoms are in closed-packed, the peak distributed near 60° occurs, the latter peak means a typical metallic interaction. With increasing temperature the distribution function $g^{(3)}(\theta, r_c)$ becomes broad for $r_c = 3.2$ and 3.5 Å while that for $r_c = 3.0$ Å is almost unchanged. This means that the short-range structure within 3 Å dose not so much depend on the temperature.

References

[1] G. Frohberg *et al.*, Proc. 6th Europ. Symp. on Material Sciences under microgravity conditions, Bordeaux, 2-5 Dec. 1986.

[2] T. Itami *et al.*, J. Jpn. Soc. Microgravity Appl. **15** (1998) 225-232.

[3] S. Takeda *et al.*, J. Phys. Soc. Jpn. **53** (1984) 3447-3456

[4] Y. Waseda, The Structure of Non-Crystalline Materials, Liquid and Amorphous Solid, McGraw-Hill, New York 1980

[5] F. Shimojo *et al.*, Phys. Rev. B **52** (1995) 9320-9329

2.5.9

Neutron Powder Diffraction study of K_x@K-LTA using the MEM-based whole pattern fitting

T. Ikeda, T. Kodaira[1] and F. Izumi

National Institute for Research in Inorganic Materials, Tsukuba, Ibaraki 305-0044, Japan
[1]National Institute of Materials and Chemical Research, Tsukuba, Ibaraki 305-8565, Japan

Crystal structure of the K clusters in K_x-doped zeolite K-LTA (x = 4.9, 5.8) with ferromagnetic properties were studied by using neutron powder diffraction.

A detailed crystallographic study is indispensable for understanding the mechanism of the ferromagnetism because the mode of ordering in the clusters affects a magnetic ordering. Especially, nuclear density distribution gives us very important information to understand a spatial view of K clusters. Neutron powder diffraction data of x = 4.9 and 5.8 were collected at 11 K and 7 K, respectively, on the HRPD high-resolution powder diffractometer with λ = 1.824 Å at the JAERI JRR-3M [1,2].

The space group of K_x-doped zeolite K-LTA was determined F23 with lattice constant of twice α-cage size a = 24.7065(9) Å at x = 4.9 and 24.6573(3) Å at x = 5.8, which led to alternate ordering of two kind of K clusters of different K^+ ions location between adjacent α-cages in framework of LTA. All atom location is clearly shown by nuclear density distributions which were obtained using the MEM-based whole-pattern fitting method derived from combination the Rietveld refinement and the MEM calculation by REMEDY & RIETAN-98 [3].

Preliminary Rietveld refinements revealed almost structural view and K^+ ions positions. However, disordering of K atoms cannot be sufficiently represented in these structure refinements. After one iteration of the MEM-based whole-pattern fitting, R_B slightly decreased from 2.82% to 2.32%, and R_F from 1.55% to 1.07% for $K_{4.9}$@K-LTA in Fig. 1, respectively. Figure 2 shows nuclear density map of (110) plane. K^+ ions are observed with different arrangements in adjacent α-cages.

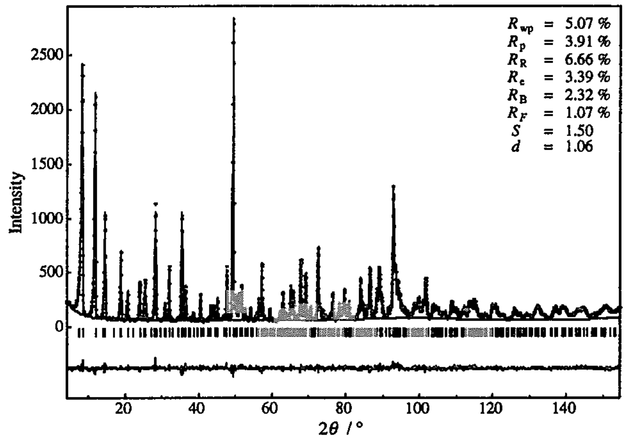

Fig.1 After refinements of $K_{4.9}$@K-LTA at 11 K

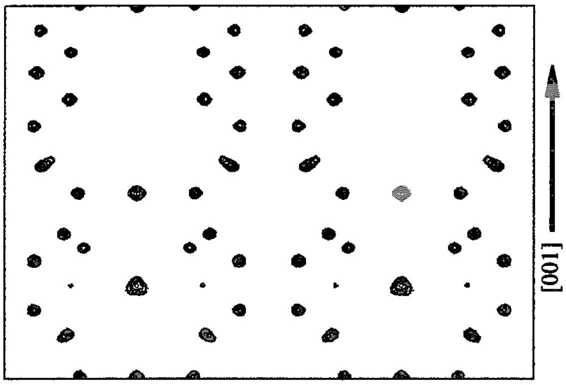

Fig.2 Nuclear density distributions of $K_{4.9}$@K-LTA.

The difference in the number of K atoms between the two types of the α-cages was ca. two in a sample with the highest degree of spontaneous magnetization, which will give rise to the ferromagnetism with antiferromagnetic components.

Reference

[1] T. Ikeda, T. Kodaira, F. Izumi and T. Kamiyama, Chem. Phys. Lett., **318**, 93 (1999).
[2] T. Ikeda, T. Kodaira, F. Izumi and S. Kumazawa, Mol. Cryst. Liq. Cryst., in press.
[3] F. Izumi, T. Ikeda, Mater. Sci. Forum, **321-324** 198-203 (2000).

2.5.10

Single Crystal Neutron Diffraction Study of the Crystalline-State Photoracemization of Cobaloxime Complex with Bulky Alkyl Group by BIX-3 Diffractometer

H. Imura, T. Ohhara, H. Uekusa, T.Ozeki, Y. Ohashi, I. Tanaka[1], K. Kurihara[1] and N. Niimura[1]

Dept. of Chemistry and Materials Science, Tokyo Inst. of Tech., Meguro-ku, Tokyo 152-8551, Japan
[1]Japan Atomic Energy Research Institute, Tokai, Ibaraki 319-1195, Japan

Crystalline-state photoreaction of cobaloxime complexes which have intramolecular Co-C bond have been greatly interested as a model reaction of the bioactivation of Vitamin B_{12}, and various reactions of cobaloximes have been investigated by X-rays. Recently, the crystalline-state photoracemization of [(*R*)-bis(ethoxycarbonyl)ethyl](pyridine)cobaloxime (*1a*) was reported[1]. This reaction was very interested because the bulky (*R*)-bis(ethoxycarbonyl)ethyl group was racemized in the restricted environment of crystal lattice, however, the mechanism of the racemization was obscure. In this work, the hydrogen atom bonded to the α-carbon atom of the reactive group was replaced with the deuterium atom and the migration of this deuterium atom according to the racemization was followed by single crystal neutron diffraction to clarify the mechanism of this photoracemization.

The crystal of partly deuterated *1a* (*1b*) was prepared. The hydrogen atoms of dimethylglyoximato and pyridine ligands were also replaced with deuterium atom to prevent the incoherent neutron scattering from hydrogen atoms. The near infrared light (>680nm) was irradiated to the crystal for 7 days. After irradiation, the single crystal neutron diffraction measurement was carried out by BIX-3 diffractometer at the 1G port of the JRR-3M reactor. The crystal size was 2.5x1.6x1.0mm, and the wavelength was 2.35Å. In the 3 days measurement at room temperature, 656 independent reflections were obtained.

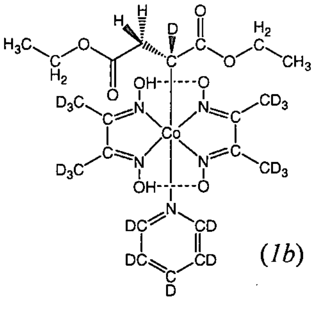

(*1b*)

As a result of structure refinement, the inverted (*S*)-bis(ethoxycarbonyl)ethyl group was observed with 35% occupancy. In this group, the deuterium atom was also bonded to the α-carbon atom. This result indicates that the crystalline-state photoracemization proceeds with the rotation of bis(ethoxycarbonyl)ethyl radical produced by irradiation as shown in Figure 1. The free rotation of the single bond between the α-carbon and its neighbor carbon atoms in alkyl radical would make such inversion mechanism possible.

Reference

[1] H. Sato and Y. Ohashi, Bull. Chem. Soc. Jpn. **72** (1999) 367-375.

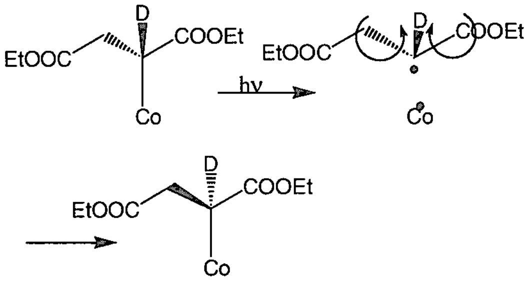

Fig. 1 Mechanism of the crystalline-state photo-inversion of bis(ethoxycarbonyl)ethyl group

2.6 Materials Science and Industrial Applications

2.6.1 SANS Study of precipitation phenomena of electron-irradiated Fe-Cu alloy

K. Aizawa, A. Iwase, T. Tobita and M. Suzuki

Japan Atomic Energy Research Institute, Tokai, Ibaraki 319-1195, Japan

In order to understand the relation of precipitation and hardening of electron irradiated Fe-Cu alloy system, we studied Fe-0.53at%Cu and Fe-0.0018at%Cu alloys by small-angle neutron scattering (SANS). Electron irradiations were carried out at the ACCELERATOR NO.2 at Takasaki establishment of JAERI. The electron irradiation dose is ranged from 8×10^{-5} to 8.55×10^{-4} dpa. SANS measurements were performed using SANS-J instrument at JRR-3M in JAERI. The covered q-range ($q=2\pi\theta/\lambda$, θ : scattering angle, λ : neutron wavelength) was from 0.2 to 2nm^{-1}.

Figure 1 shows the evolution of SANS cross-section of electron irradiated samples evaluated by subtracting intensity from unirradiated sample. As increasing electron irradiation dose, SANS cross-section increased and shifted to lower q-value in the case of Fe-0.53at%Cu alloy. On the other hand, SANS cross-section of Fe-0.0018at%Cu alloy, which is low copper concentration sample, is rather lower than that of Fe-0.53at%Cu alloy corresponding to electron irradiation dose. This means that SANS cross-section arise from copper precipitation due to electron irradiation but not irradiation damage such as vacancy clusters. We assumed that the shape of the precipitation is spherical and performed least square fittings. Solid lines are fitted curves in Fig. 1. The fitting is quite well. We performed Guinier analysis also and Guinier plots showed straight regions in all data. These mean that polydispersibility of precipitate is low.

Figure 2 shows the evolution of the radius of copper precipitate obtained from model fitting and Guinier analysis. Copper precipitated even very low electron irradiation dose in the case of Fe-0.53at%Cu alloy. And we can see a tendency of saturating of the radius in high electron irradiation dose.

The hardness curve obtained from the Vickers hardness measurement behaves as a curve of evolution of radius. This means that the radius or volume of precipitation is strongly correlated to the hardness.

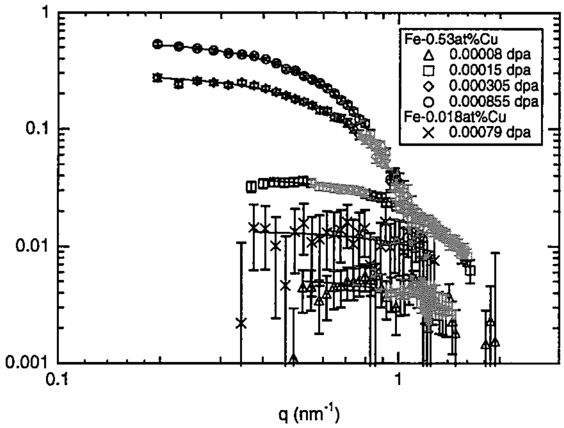

Fig. 1 SANS cross-section for copper precipitate of electron irradiated Fe-0.53at%Cu and Fe-0.0018at%Cu alloys.

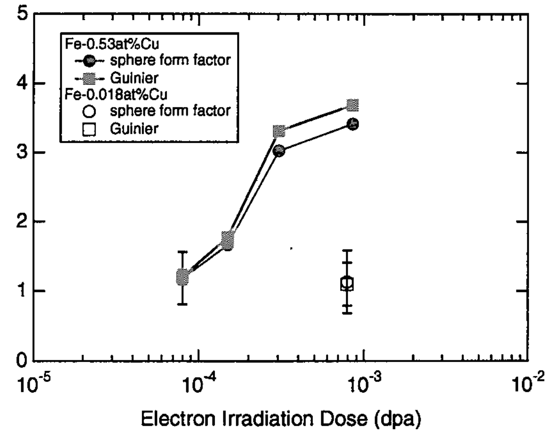

Fig. 2 Evolution of radius of copper precipitate obtained from sphere-particle model fitting and Guinier analysis.

2.6.2 Measurement of Elastic Constant of A7075 in Neutron Diffraction

T.Saito[1,2], N.Minakawa[2], Y.Morii[2]

[1]Department of Material Science & Engineering, Kanazawa University, Kanazawa, Ishikawa 920-1192, Japan
[2]Japan Atomic Energy Research Institute, Tokai, Ibaraki 319-1195, Japan

Residual stress in material has been frequently measured by neutron diffraction method. In the residual stress measurement by the neutron diffraction method, the strain on various diffraction planes should be measured. The stress can be obtained by using Hooke's law from the strain arises when material is deformed. In the neutron diffraction method, the stress can be calculated from the strain for three axial directions.

$$\sigma_{R,H,A} = \frac{E}{1+\nu}\left[\varepsilon_{R,H,A} + \frac{\nu}{1-2\nu}\left(\varepsilon_R + \varepsilon_H + \varepsilon_A\right)\right]$$

The elastic constant is necessary to convert this strain into the stress. E is Young's modulus, and ν is Poison's ratio.

Purposing of this experiment is to make the data bank of this elastic constant. Then, the elastic constant for Al(111), (200) and (220) of A7075 was calculated in this experiment. In the measurement a small tensile specimen was loaded in the tensile test rig specially designed for a neutron diffractometer. To calculate the elastic constant, the strain on two kinds of diffraction planes should be measured. That is, when the load is given to the sample, the strain of the expanding lattice spacing and the shrinking lattice spacing should be measured. This state is shown in Fig.1(a) and (b). The expanding lattice spacing is measured in (a). Fig.2 shows the peak position of the diffraction profile against the stress. The peak position shifts to the low angle in the lattice spacing of the expansion. The peak position shifts to the high angle in the lattice spacing of shrinking. The shrinking lattice spacing is measured in (b). Fig.3 shows the strain against each load for A7075. The slope of the approximation straight line of the expanding strain is E in these graphs. Moreover, ν is a ratio for the slope of the approximation straight line of the expansion and shrinking.

The elastic constant in each diffraction plane which had been as mentioned above calculated by the neutron diffraction method was able to be calculated.

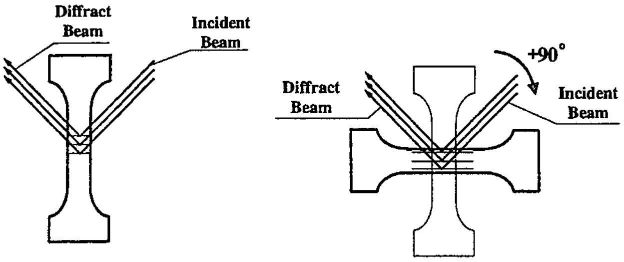

(a) expanding (b) shrinking

Fig. 1. Scattering geometries for measurement of two components of lattice strain

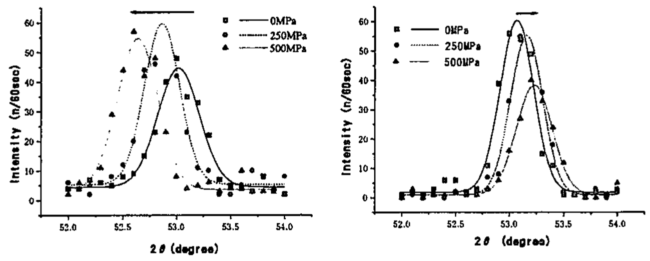

(a) expanding (b) shrinking

Fig. 2. Peak position of diffraction profile against stress for Al(111).

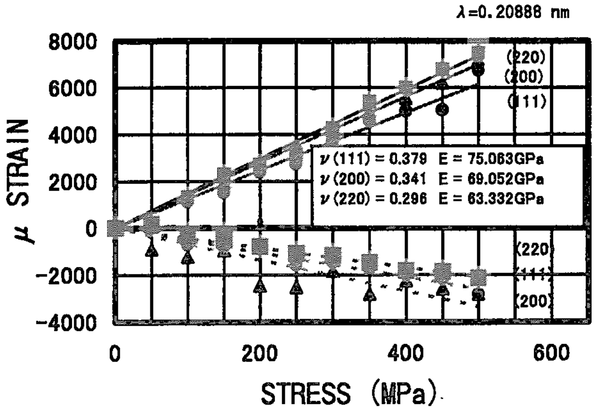

Fig. 3. Relation between stress and strain for A7075.

2.6.3 Measurement of Residual Stress Redistribution for Structural Material by Neutron Diffraction

Y. Tsuchiya, K. Kikuchi[1], N. Minakawa[2], Y. Morii[2], T. Kato, H. Nakajima and H. Tsuji

Naka Fusion Research Establishment, Japan Atomic Energy Research Institute, Ibaraki 311-0193 Japan
[1] Center for Neutron Science, Japan Atomic Energy Research Institute, Ibaraki 319-1195 Japan
[2]Advanced Science Research Center, Japan Atomic Energy Research Institute, Ibaraki 319-1195 Japan

A machining introduces a residual stress and produces a redistribution of the residual stress to a material. Estimation of the residual stress for industrial material at each step of processes is required for preventing some problems such as stress-induced cracking. In this study, the residual stress redistribution that was brought by a bending processing of a conduit material was measured by neutron diffraction using a neutron diffractometer for the residual stress analysis, RESA, installed at the research reactor JRR-3M guide hall.

The sample is a round-hollowed conduit of INCOLOY908 alloy for a superconducting coil. INCOLOY908 is a nickel-iron based alloy and it shows fcc single phase. The conduit has been compressed by 5% to the radial direction by cold rolling. After the rolling, the conduit has a square cross section of 46 × 46 mm^2 and an inner diameter of 37 mm. For the neutron diffraction measurement, the conduit was cut in length of 150 mm. Then the compressed conduit was bent in radius of 500 mm by a triple-roll bender at room temperature. A sampling volume was adjusted for the size of 2 × 2 × 4 mm^3 by the cadmium slits. The sampling volume was located at every 1 mm in depth from the sample surface to the radial direction. The measurement position was the center of the conduit sample as illustrated in figure 1. The thickness of the conduit is 4.5 mm at the measurement position. The wavelength of the incident neutron beam used was 2.07 - 2.08 Å. The reflection of (111) plane was used for the measurement. The data acquisition time was set 2 to 8 hours for a spectrum. The elastic constants that were evaluated by the neutron diffraction measurement under tension load were used for a calculation of the residual stress. The Young's modulus was 195 GPa and the Poisson's ratio was 0.26 for the (111) plane of INCOLOY 908 alloy.

Figure 1 shows the axial residual stress distribution at the inside position of the bent conduit as a function of the depth from the outer surface of the conduit. The triangles indicate the residual stress and the solid line shows the distribution of the as-compressed straight sample in the figure. The axial residual stresses were observed tension on the all measurement point at the inside of bent sample. The axial residual stress reveals the largest value of 220 MPa of tension at the outer surface. The tensile stress decreases gently with the depth of sample and became 65 MPa at 3 mm in depth.

While, the residual stress of the as-compressed straight sample shows a large distribution from tension to compression. These result shows that the initial large residual stress tends to relax by the bending processing of the conduit.

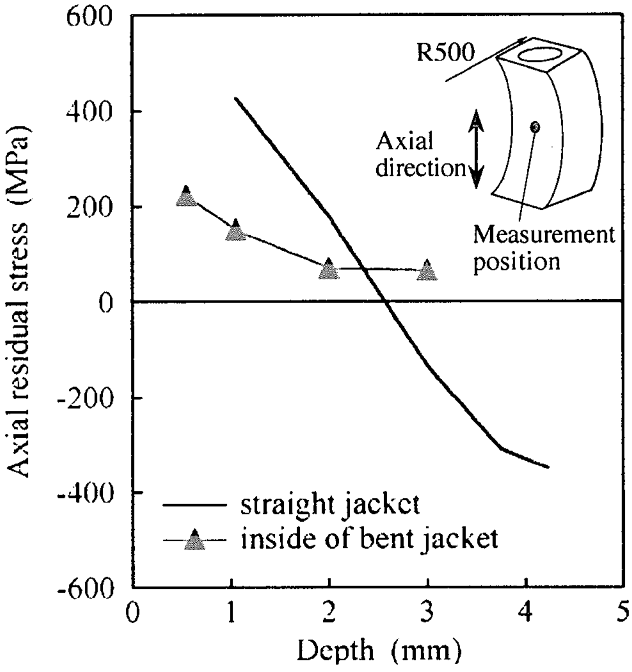

Fig 1. The redistribution of the axial residual stress of the conduit material after bending process.

2.6.4 Neutron Stress Measurement using Neutron Image Plate

T.Sasaki[1], N.Minakawa[2], Y.Morii[2], N.Niimura[2] and Y.Hirose[1]

[1]Kanazawa University, Kanazawa, Ishikawa 920-1192, Japan
[2]Japan Atomic Energy Research Institute, Tokai, Ibaraki 319-1195, Japan

A neutron image plate (NIP) was developed recently as an area detector for the neutron experiment. It is possible to obtain strains along the line in the material where neutron beams penetrate analyzing a Debye-Scherrer ring recorded on a NIP. The diffraction ring contains continuous strains with different orientations, so that the depth profile of stress can be determined more correctly as well as quickly than the ordinary method. In this study, we investigate the fundamental possibility of the NIP for the stress measurement.

The neutron experiment was conducted using the reactor named JRR-3M at the Japan Atomic Energy Research Institute (JAERI). Thermal neutrons derived from the reactor pass through the guide tube which is made from glass coated with nickel thin film, and was monochromated by 002 diffraction of pyrolytic graphite to the wave length of 0.20888 nm. There is a 2000 mm length flight tube made from aluminum after the monochrometer. A slit made from B_4C rubber having a hole of the diameter of 10 mm was put at the entrance of the flight tube, and another slit made from cadmium of the diameter of 3 mm was put at the exit. The NIP enwrapped in black paper was put into a cassette which was covered with both an aluminum plate (1 mm thickness) and a lead plate (1 mm thickness). The cassette, placed normal to the beam, has a hole at its center so the neutron beam can pass through. The specimen was put after the NIP. The distance between the NIP and the specimen was 65 mm. The incidence angle of the neutron beams to the specimen was 20 degree.

The specimen used for the neutron experiment was steel (JIS S50C) with a thickness of 2 mm. Mean grain size of the specimen was 10 μm. Main neutron diffraction conditions were as follows: wave length of neutron 0.20888 nm, diffraction plane Fe-211, diffraction angle 2θ=127 deg., incident angle of neutron beam to the specimen 24 deg, diameter of neutron beam about 3 mm, exposure time 2 hours. The specimen was applied tensile strains of 0, 400 and 800 ($\times 10^{-6}$) respectively. Strain in the specimen was monitored with a strain gauge attached. Applied stress was calculated by multiplying the Young's modulus (206 GPa) to the strain.

The NIP used had a rectangular shape with the dimensions of 250 mm×200 mm. The intensity of the diffracted neutron stored in NIP was read out under the condition of 100 μm for space resolution and 8 bit for intensity resolution, and saved in the computer. The fundamental image processing was conducted using the software made by Fuji Film Co., which was however not sufficient for the stress analysis. So new software was developed for the stress analysis in this study.

A steel plate was used for determining the position of the incident neutron beams on NIP, assuming its Debye-Scherrer ring as a circle. The diffraction pattern of the plate was double exposed on NIP by putting the plate at the position between NIP and the specimen. The distance between the plate and NIP was 35 mm.

Since the diffraction profile obtained from NIP is a superposition of diffracted neutron beams from a wide range of the depth, the stress calculation should be conducted considering the effect of the neutron beams diffracted inside of the specimen. However, such a method has not been proposed yet. So the method which has been used for the X-ray image plate (XIP) was used in this study (ref [1][2]). The result will show limits and effectiveness of the theory used in the X-ray stress analysis.

The diffraction image data was analyzed on the computer with the diffraction profile in the direction of the radius of the ring calculated for the whole ring, from which the radii of the ring and the strain were determined. This calculation was conducted by 1 degree step of the central angle, and 360 strains were obtained from each Debye-Scherrer ring. Finally, the stress was calculated according to the method shown in the previous section. The stress which was obtained from the specimen was compared with the theoretical one which was calculated with applied strain and Young's modulus. It was seen that the stress obtained by the present method almost agrees with the theoretical value. The result shows that it is possible to determine mean stress in the material with neutron diffraction using a NIP. Fig.1 shows the distribution of radii obtained from the Debye-Scherrer ring as a function of the central angle. Plots in the figure indicate the result obtained with NIP, and the curved line indicates the result recalculated by the present method using the stress obtained from the experiment. The result shows a similar tendency in macroscopic view in case of the applied strain of 800×10^{-6}, but a larger difference can be seen at the other strain levels. Since the calculation of the stress and the recalculation of the radius on the diffraction ring were conducted using the equations based on the X-ray stress measurement, the effect of the beams diffracted at the deeper place in the specimen was not considered. As the neutron diffracted beams can emerge from deeper in the specimen than X-rays, the diffraction profile is influenced by them more severely. In the case of the small specimen, a part of the diffracted beam can pass through the side face of the specimen. Since these beams are absorbed by the material slightly, they deform the shape of the diffraction profile on NIP, which leads to the shift of the peak position as shown in Fig.1. A similar phenomena can occur in the Cu plate, which results in the error at the determination of the center position of the diffraction ring on NIP images. This error can have influence on the determination of the radius of the diffraction ring.

Another new experiment has been conducted after this experiment by improving some experimental conditions used in this study. Although the data has not yet been analyzed completely, some good results have been seen.

Though the experiment was performed in a uniaxial and uniform stress state, most materials have generally a multiaxial stress state as well as nonlinear depth profile inside the body. So the method need to be modified to cope with these situation at the next stage. The theoretical proposal and the verification for this problem have already been done in the X-ray range using XIP. (see ref[1]-[3])

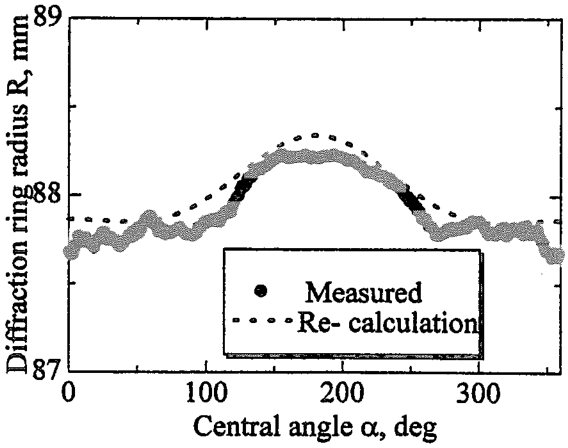

Fig.1 Plots of radius of the Debye-Scherre ring vs. central angle. Curved line indicates recalculated results using stress measured.

References

[1] T. Sasaki and Y. Hirose, J. Soc. Mat. Sci., Japan, vol.**44**, No.504 (1995) 1138-1143.
[2] T. Sasaki and Y. Hirose, Trans. Japan Soc. Mech. Eng., vol.**61**, No.590, A, (1995) 2288-2295.
[3] T. Sasaki, Y. Hirose and S. Yasukawa, Trans. Japan Soc. Mech. Eng., vol.**63**, No.607, A, (1997) 533-541.
[4] T. Sasaki and Y. Hirose, Trans. Japan Soc. Mech. Eng., vol.**63**, No.606, A, (1995) 370-377.
[5] T. Sasaki and Y. Hirose, Trans. Japan Soc. Mech. Eng., vol.**63**, No.614, A, (1997) 2196-2204.

2.6.5

Phonon Dispersion of $Ti_{50}Ni_{30}Cu_{20}$ Prior to B2-B19 Martensitic Transformation

X. Ren, K. Taniwaki, N. Miura, M. Inami, J. Zhang, K. Otsuka, Y. Morii[1], Yu.I. Chumlyakov[2]

Institute of Materials Science, University of Tsukuba, Tsukuba, Ibaraki 305-8573, Japan
1. Japan Atomic Energy Research Institute, Tokai, Ibaraki 319-1195, Japan
2. Siberian Physical Technical Institute, Tomsk 634050, Russia

Point defects and alloying elements can greatly alter many aspects of martensitic transformation. The most well known effect is the great change in transition temperature and even in the structure of transformation product with alloying addition or quench (which introduces point defects). Another effect is the martensite aging effect, which causes interesting rubber-like pseudo-elasticity [1] and two-way shape memory [2]. The latter effect has attained a fairly clear understanding [1,2]; however, the former effect is far from being well understood. To understand these effects, a study of lattice dynamics as a function of composition is most desirable, because martensitic transformation is closely related to lattice dynamics. Our recent work on TiNi-based alloys [3-5] revealed some interesting aspects of the composition dependence of elastic constants prior to martensitic transformation. These results provided some new insight into the central question about how martensitic transformation is altered by alloying addition or composition change.

Nevertheless, elastic constant measurement provides only incomplete information about lattice dynamics, because it is related only to the initial slop of the phonon dispersion curve. To obtain complete information about lattice dynamics, measurement of the whole phonon dispersion curve, especially the TA2 [110](e//[1 $\bar{1}$ 0] acoustic branch is most desirable.

In the present study, we measured the phonon dispersion relation of $Ti_{50}Ni_{30}Cu_{20}$ alloy prior to B2-B19 (cubic-orthorhombic) transformation with neutron inelastic scattering. The result is compared with the phonon dispersion of $Ti_{50}Ni_{50}$ alloys. Such a comparison may provide important insight into the nature of the composition effect on martensitic transformation.

Single crystal sample with a size of $9*9*6mm^3$ was mounted on a triple axis spectrometer TAS-2 with a temperature controlling system. The incident neutron energy was 14.7mV (wavelength 2.35A) , a PG filter was used to reduce higher order reflection, the collimations were 17'-40'-40'-40'. It should be pointed out that Ti-Ni based alloys appear to exhibit strong incoherent scattering, which makes the background very high, thus the accurate determination of peak position is difficult, especially around BZ boundary. We tried to solve this problem by sampling over a wide ΔE range for several times and determined peak position with Guassian fitting.

The main results are as follows:

(1) TA2 phonon branch exhibits a very broad dip around $0.375q_{max}$, being neither 1/3 nor 1/2 position. This dip deepens with lowering temperature toward Ms. However, it seems that it will not go to zero even at Ms temperature.

(2) The position of the dip also exhibits strong temperature dependence. It shifts towards $(1/2)q_{max}$ position with approaching Ms temperature.

(3) TA1 [100][001] branch is also low for this system, having the same feature as the binary TiNi alloy. Due to the limitation in

machine time, we were not able to measure the temperature dependence of this branch. Nevertheless, from the elastic constant measurement, we can indirectly conclude that this branch also softens with lowering temperature [5].

Compared with the phonon dispersion of binary TiNi alloys, $Ti_{50}Ni_{30}Cu_{20}$ alloy show some similarities and dissimilarities. TiNi alloys exhibit a clear 1/3 TA2 dip and a shallow 1/2 TA2 dip [6]. The 1/3 dip is related to the trigonal R phase, while to 1/2 dip is related to the B19 phase. However, this alloy does not transform to B19 phase due to the coupling of 1/2 mode with the low TA1. The initial slope of the TA1 branch of TiNi is lower than that of $Ti_{50}Ni_{30}Cu_{20}$ alloy. This is responsible for the fact why TiNi transforms into the B19' martensite (which requires a softening in TA1 BZ center mode), while $Ti_{50}Ni_{30}Cu_{20}$ alloy transforms into B19' at much lower temperature.

From the above information, we can clearly understand why $Ti_{50}Ni_{30}Cu_{20}$ alloy does not transform into R phase. This is due to the absence of the 1/3TA2 dip. We can also understand why B19 martensite appears (which does not appear in TiNi alloys. This is due to the significant softening around 1/2 position, as well as the hardening of the TA1 BZ center mode; the first factor promotes the condensation of 1/2[110](e//[1 $\bar{1}$ 0] mode (which leads to B19) and the second factor prevents the coupling of the TA1 BZ center mode with the 1/2 TA2 mode (such a coupling leads to B19' formation). As a result, Cu addition changes the transformation path from B2-(R)-B19' for TiNi into B2-B19-B19' for $Ti_{50}Ni_{30}Cu_{20}$.

References:

1. X. Ren and K. Otsuka, Nature, 389 (1997), 6651.
2. X. Ren and K. Otsuka, Phys. Rev. Lett., 2000, in press.
3. X. Ren and K. Otsuka, Scripta Mater., 38(1998), 1669.
4. X. Ren, K. Taniwaki, K. Otsuka, T. Suzuki, K. Tanaka, Yu.I. Chumlyakow, and T. Ueki, Philo. Mag. A, 79(1999), 31.
5. X. Ren, N. Miura, J. Zhang, K. Otsuka, K. Tanaka, M. Koiwa, T. Suzuki, Yu.I. Chumlyakov, M. Asai, submitted to Mater. Sci. Eng. A, 2000.
6. P. Moine, J. Allain, and B. Renker, J. Phys. F: Met. Phys. 14 (1984), 2517.

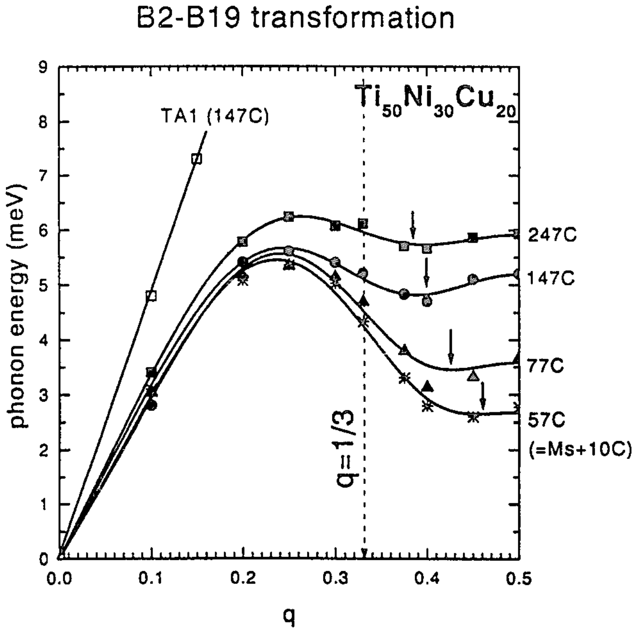

Figure 1. TA2 and TA1 phonon branch of $Ti_{50}Ni_{30}Cu_{20}$ alloy prior to B2-B19 martensitic transformation.

2.6.6 Diffuse Neutron Scattering from GaAs

M. Arai, K. Ohki, M. Mutou, T. Sakuma, H. Takahashi[1], Y. Ishii[2]

Faculty of Science, Ibaraki University, Mito 310-8512, Japan
[1]Faculty of Engineering, Ibaraki University, Hitachi 316-8511, Japan
[2]Japan Atomic Energy Research Institute, Tokai 319-1195, Japan

Correlation effects between the thermal displacements of atoms1) play an important role to explain the oscillatory diffuse scattering in solid electrolytes, CuI and AgBr. The correlation effect would not be specific in solid electrolytes. In order to inspect the existence of the oscillatory diffuse scattering in semiconductor, diffuse neutron background intensity of GaAs has been measured at 290 K and 8 K using a neutron diffractometer TAS-2 installed at JRR-3 in JAERI. A powder sample of GaAs in a vanadium container with 8 mm in diameter was used. The incident neutron wave length of 1.443 Å was used. Neutron diffraction data were collected for 60 sec per step at 0.1° intervals over the 2θ range of 5° to 118° by a step-scan mode. Fig. 1 shows the result of the double-axis measurement of GaAs at 8 K and 290 K. Several sharp Bragg lines and a large diffuse scattering were observed at 290 K. The first and second peak of the oscillatory diffuse scattering appear at $2\theta \sim 45°$ and 85°, respectively. The oscillatory characteristic in the diffuse scattering of GaAs at 8 K is not clear. The temperature dependence of the oscillatory diffuse scattering from GaAs crystals, which was predicted with the correlation effect between the thermal displacements of atoms, was confirmed by the measurement.

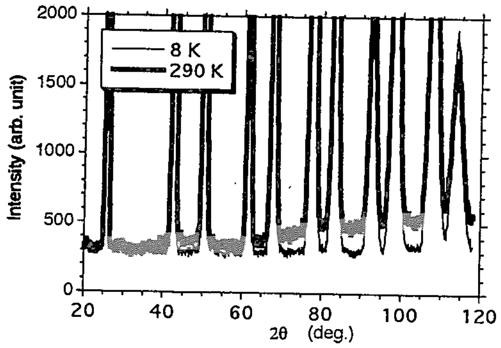

Fig.1 Observed neutron powder diffraction intensity for GaAs at 8 K and 290 K.

Numerical calculations of the diffuse background have been made based on zinc blende type structure of GaAs including the correlation between the thermal displacements of atoms. The peak positions of the first and second peak in diffuse scattering of GaAs in fig. 1 are greater than those of super ionic conductor CuI which belongs to zinc blende type structure. They are related to the reciprocal of the distance between nearest neighbor atoms; the distances in CuI and GaAs are 2.60 and 2.45 Å at 290 K, respectively. The main contribution to the oscillatory diffuse scattering of super ionic conductors was from the correlation among the displacements of cation and anion atoms. It is suggested that the main contribution of GaAs would be from the correlation among the displacements of gallium and arsenic atoms.

Expected contributions from Ga-Ga, Ga-As and As-As pairs to the diffuse scattering were calculated. The contribution from the correlation among Ga-Ga and As-As atoms was very weak to produce the observed oscillating scheme. The main contribution to the observed oscillatory diffuse scattering is from the correlation between the thermal displacements of gallium and arsenic atoms. The background function including the correlation effect between the thermal displacements of atoms is very effective to treat the diffuse scattering from crystals with the measurement by X-rays and neutrons.

Reference

[1] T. Sakuma: J. Phys Soc. Jpn, 42(1993), 4150

2.6.7

Neutron Diffraction Study on Shape Memory Effect of Ni_2MnGa-based Alloys

K. Inoue, K. Enami, M. Igawa, Y. Yamaguchi[1], Y. Morii[2] and Y. Matsuoka[2]

Fac. Sci & Tech. Ryukoku Univ. Seta, Otsu 520-2194, Japan
[1]IMR, Tohoku Univ. Aoba-ku, Sendai 980-8577, Japan
[2]Japan Atomic Energy Research Institute, Tokai, Ibaraki 319-1195, Japan

We intend to control the shape memory effect originated from the thermoelastic martensitic transformation of the Heusler-type Ni_2MnGa-based alloy, using the external magnetic field instead of temperature change. The martensitic transformation temperature, M_S, of stoichiometric Ni_2MnGa is about 200K$^{1)}$. The alloy is ferromagnetic below and above this M_S point. The Curie temperature, T_C, of the Heusler structure above M_S point is around 370K$^{1)}$. For our intention, we tried to bring the temperature, M_S, closes to the temperature, T_C, by changing the concentration of composite atoms off-stoichiometrically. As a result, the magnetic energy under the magnetic field of the ferromagnetic martensitic phase is smaller than that of the paramagnetic Heusler phase.

In this paper, we report the effect of magnetic field on the transformation of Heusler-type $Ni_{2.19}Mn_{0.81}Ga$, of which the M_S and T_C temperatures coincide to be about 350K.

We have made the powder neutron diffraction of this $Ni_{2.19}Mn_{0.81}Ga$ at 297K with no magnetic field, using HERMES diffractometer installed at JRR-3M reactor at JAERI. The neutron wave length was 1.8196Å. The result is shown in Fig.1. The diffraction pattern is similar to that of $Ni_2(Pd_{0.16}Mn_{0.84})Ga$ at 16K $^{2)}$. This fact indicates that the martensitic structure of this $Ni_{2.19}Mn_{0.81}Ga$ is the same as that of $Ni_2(Pd_{0.16}Mn_{0.84})Ga$, that is, two structures coexist. One is an orthorhombic structure distorted from the cubic Heusler one and the other is a monoclinic one with the shuffling of 6 layers of (220) planes of this orthorhombic structure $^{2)}$.

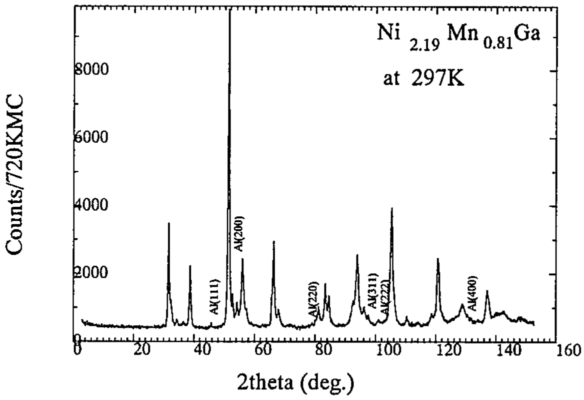

Fig.1. Neutron diffraction pattern of $Ni_{2.19}Mn_{0.81}Ga$ at 297K with no external magnetic field.

To investigate whether the martensitic transformation is affected by external magnetic field or not, we have observed the powder neutron diffraction patterns of $Ni_{2.19}Mn_{0.81}Ga$ at M_S temperature of 350K under the external magnetic field. The TAS-2 diffractometer installed at JRR-3M reactor at JAERI, equipped with a superconductor magnet, was used. The neutron wave length was 1.6498Å. We have observed the change of the peak intensity in the region of $2\theta = 67^\circ \sim 96^\circ$, which corresponds $2\theta = 75^\circ \sim 110^\circ$ in the case of HERMES measurement. In this 2θ region at 350K, two nuclear peaks of Heusler phase and the other peaks of martensitic phase are observed simultaneously. The effect of magnetic scattering disappears in this high 2θ region.

The experimentally obtained diffraction patterns of the alloy under each magnetic field and the result of Rietveld analysis with the computer program, RIETAN $^{3)}$, are shown in

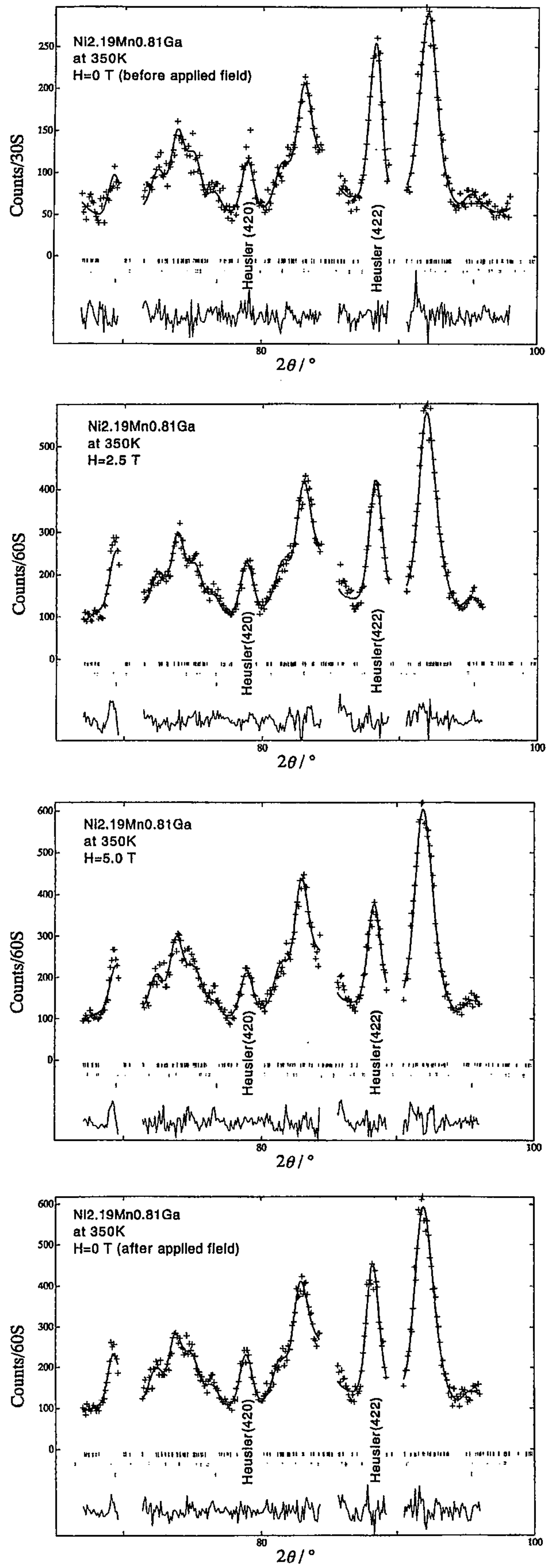

Fig.2. Change of diffraction pattern due to external magnetic field and the result of Rietveld analysis.

Fig.2. The magnetic field was applied in the order 0T, 2.5T, 5.0T and then 0T. The results are shown from upward to downward in the figure. We explicitly observe that the application of magnetic field reduces the peak intensity of the Heusler phase. The mass fraction of each phase versus each magnetic field, obtained by Rietveld analysis, is shown in Fig.3.

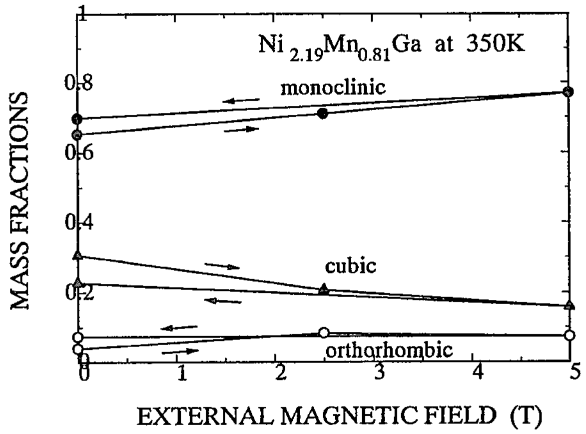

Fig.3. Mass fraction of each phase versus external magnetic field for $Ni_{2.19}Mn_{0.81}Ga$ at 350K.

The mass fraction of cubic Heusler phase under the magnetic field of 5T decreases to be half as much as that under the first field of 0T. This result suggests the possibility that the application of magnetic field onto the cubic Heusler phase just above the transformation temperature changes the Heusler phase to martensitic one.

References

[1]P.J.Webster, K.R.A.Ziebeck, S.L.Town and M.S.Peak: Philos.Mag. 49 (1984) 295.

[2]Kazuko Inoue, K.Enami, M.Igawa, Kanryu Inoue, Y.Yamaguchi and K.Ohoyama: Proceedings of the International Conference on Solid-Solid Phase Transformations '99 (1999) 1120.

[3]F.Izumi: *The Rietveld Method*, ed. R.A.Young (Oxford Univ. Press, Oxford, 1993) Chap.13.

2.6.8
Residual strain measurement of functionally gradient material by RESA

K. Inoue, T.Tsujikami, M. Kawagai, M.Ohyanagi, N.Minakawa[1], Y. Morii[1] and T.Saitoh[1]

Fac. Sci & Tech. Ryukoku Univ. Seta, Otsu 520-2194, Japan
[1]Japan Atomic Energy Research Institute, Tokai, Ibaraki 319-1195, Japan

An internal residual strain of the three-layer functionally gradient material, [WC-10Wt%Ni]-[Ni]-[WC-10Wt%Ni], made by combustion synthesis was measured by neutron diffraction with a detection system, RESA, which is installed at JRR-3M reactor at JAERI. The material [WC-10Wt%Ni] is a super hard alloy. The results obtained by the measurements are discussed in comparison with those calculated by finite element method.

The material was made by self-propagating high temperature synthesis with the ignition by the induction heating. The synthesis was done by the static pseudo isostatic compaction method under 25MPa. The obtained three layers material and the SEM image of [WC-10Wt%Ni] layer is shown in Figs.1(a) and (b). The diameter of this material is about 37.8 mm and the thickness is about 12.4mm. In Fig.1 (b), the white particle is composed of WC, of which size is several μm, and the black region is composed of Ni.

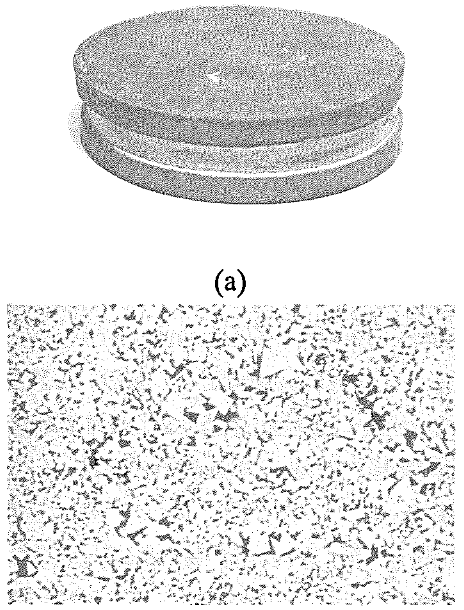
(a)

(b)

Fig.1. (a) the shape of the three layers sample and (b) the SEM image of the [WC-10Wt%Ni] layer.

The residual strain was measured for radial and axial directions. As the size of the slits for both incident and reflected beams was 2mm × 10mm, the area including three layers was observed simultaneously. Some typical peaks versus 2θ angle are shown in Figs.2 and 3.

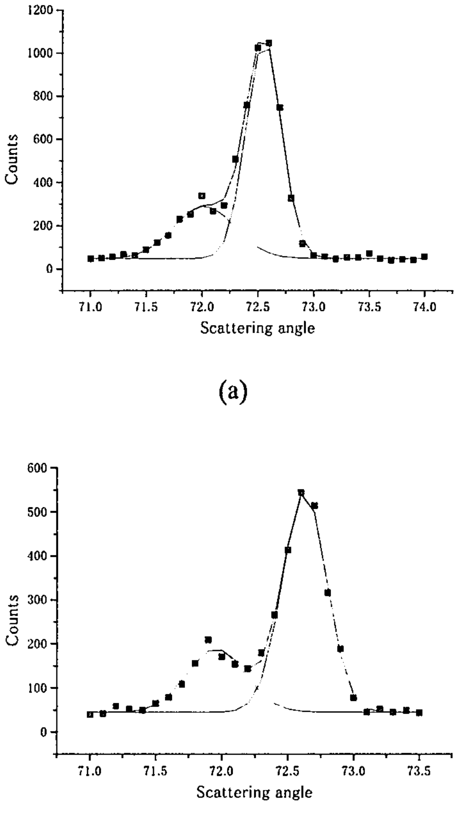

(a)

(b)

Fig.2. Ni (200) reflection (a)for radial direction at 14mm position from the center of the diameter and (b)for axial direction at 10mm position from the center.

In Fig.2, a large peak from the middle [Ni] layer and a small peak from the Ni region in both side

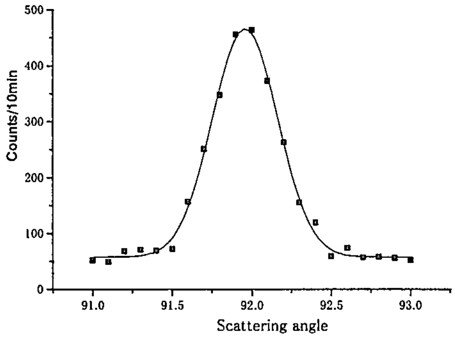

Fig.3. WC (110) reflection for radial direction at 14mm position from the center of the sample.

[WC-10Wt%Ni] layers are observed. We can estimate each strain of Ni region, comparing with the Ni (200) reflection from the [Ni] single layer material. The strain of WC in both side [WC-10Wt%Ni] layers is estimated, using the general lattice constant of WC at room temperature, a=2.9065Å, as a standard. The strain of Ni (200) plane and that of WC (110) plane in [WC-10Wt%Ni] layers for radial direction are shown in Figs.4 (a) and (b). There is no explicit difference according to each position of the sample. The Ni region in [WC-10Wt%Ni] layer both for single layer material and for three layers material is exposed to large tensile strain of 0.7~0.8%, whereas WC particles are exposed to small compressive strain between 0 and –0.2%.

The strain obtained by the measurements for the axial direction does not show any explicit difference from that for the radial direction.

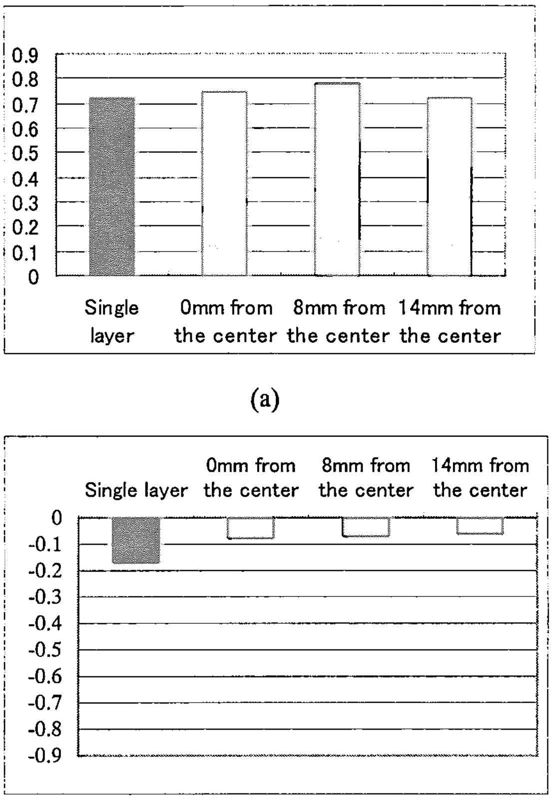

(a)

(b)

Fig.4. Strain (%) of (a) Ni (200) and (b)WC (110) in [WC-10Wt%Ni] layer for radial direction. Black bar shows the strain of single layer [WC-10Wt%Ni] material and gray bars show those of three layers [WC-10Wt%Ni]-[Ni]-[WC-10Wt%Ni] material.

The obtained strain values of Ni and WC in [WC-10Wt%Ni] layer show good coincidence with those calculated by finite element method. This fact indicates that as the Ni melted in [WC-10Wt%Ni] layer joins tightly with WC particles, it is elongated in the cooling process under the influence of the small coefficient of contraction of WC. This tensile strain is not released at room temperature. On the other hand, a large amount of WC is hardly influenced by the contraction of Ni region.

It was found that the middle [Ni] layer experiences almost no strain. This experimental result suggests that the [Ni] layer shrinks freely in the process of cooling, because the joint between the [Ni] layer and the [WC-10Wt%Ni] layer seems to be loose.

2.6.9 Lattice dynamics of disordered Perovskite PZN ($Pb(Zn_{1/3}Nb_{2/3})O_3$)

I. Tomeno, S. Shimanuki, Y. Tsunoda[1], and Y. Ishii[2]

Research and Development Center, Toshiba Corporation, Saiwai-ku, Kawasaki 210-8582
[1]School of Science and Engineering, Waseda University, Shinjuku-ku, Tokyo 169-8555
[2]Japan Atomic Energy Research Institute, Tokai, Ibaraki 319-11

Relaxor is the important industrial material which is applied to the ultrasonic devices, actuators and multi-layer capacitors due to its huge piezoelectric and dielectric response in wide temperature range. The microscopic mechanism of the properties, however, such as a glass-like phenomenon are still not well known. To study the essence of the phenomena microscopically, phonon dispersion relation of PZN ($Pb(Zn_{1/3}Nb_{2/3})O_3$) was measured by neutron inelastic scattering. The industrial PZN includes about 10% of Ti impurities, but we used pure PZN single crystal in order to avoid the effects of the impurities.

Phonon data were taken along the symmetric directions above and below the transition temperature ($T_C \sim 100\ ^\circ C$). The dispersion relation curves obtained above the transition temperature ($T = 150^\circ\ C$) is given in Fig. 1. The dispersion curves for typical dielectric materials with the perovskite structure are also given for comparison. The [1 1 0] TA_2 phonon branch of the PZN is very special. The phonon frequency is very low at small q-region. In addition, another phonon mode which is not observed for other materials seems to exist. One of possible explanations of this feature is a resonance phonon mode around 5 meV; Zn and Nb are randomly distributed in B site of perovskite structure in PZN and the mass ratio of these elements is rather large (65 : 93). Thus, the resonance phonon mode is anticipated for this system as a mass-defect random system. In the [1 0 0] T branch phonon line width studied by the constant-q mode abruptly increases around $q \sim 0.2$. This is consistent with above discussion if we assume that the resonance phonon energy is about 5 meV. Further measurements are desired to confirm the resonance phonon mode.

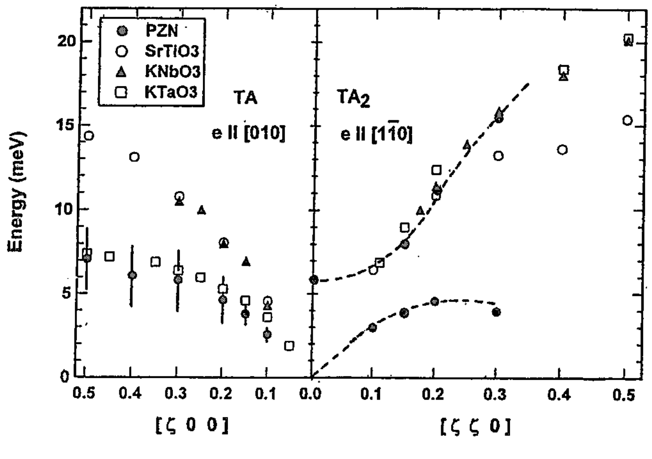

2.6.10 Residual stress measurement of friction welding boundary by neutron diffraction method

S.Okido, M.Hayashi, Y.Morii[1], N.Minakawa[1]

Mechanical Engineering Research Laboratory, Hitachi Ltd. Hitachi, Ibaraki 317-8511
[1] ASRC, JAERI, Tokai, Ibaraki 319-1195

The friction welding is the bonding method which uses the friction heat generating in the rotation of two contacted components under the load. This method is used widely in the fields of automobile, industrial machine and so on, since it can weld the different materials. However, high residual stress is expected to generate at the welding boundary through the heat history in the welding process. In this study, the neutron diffraction method is applied to measure the residual stress, and the mechanism of residual stress initiation at the bonding boundary is discussed.

SS400 carbon steel bar and Type 304 stainless steel one were bonded by friction welding. The diameter and length of each bar were 25mm and 100mm. The welding was performed in the conditions that the rotating velocity was 1200 rpm, the friction pressure was 59 MPa, and the upset pressure and time was 118 MPa and 10 sec.

RESA (REsidual Stress Analyzer) at JRR-3M, which is operated by JAERI (Japan Atomic Energy Research Institute), was used for the measurement of the lattice strain. The 110 diffraction for SS400 and the 111 diffraction for type 304 were measured. The wavelength λ of the used monochromatic neutron beam was 0.208872nm. The measurement was performed at 1, 3, 5, 8, 15 and 30 mm from the welding boundary in the center and at the surface of bar. The sampling volume in each measurement was a 2mm width and 4mm height in parallel to the boundary. The strain measured by neutron diffraction was converted to the stress using E=165GPa, Poisson's ratio=0.16 for SS400 obtained from the calculation for the mono-crystal model, and E=231 GPa, Poisson's ratio=0.19 for Type 304 obtained by literature quotation.

The obtained residual stresses in the vicinity of the boundary for both materials were shown in Fig.1. The residual stress showed compressive about 300 MPa at the surface and tensile about 200 MPa in the center of the specimen. The difference of circumferential velocity makes the higher temperature rise at the surface than in the center. However the heat radiation in the cooling process makes the temperature at surface lower rather than that of the center. The result of neutron diffraction measurement means that the residual stresses generate in the cooling process after up-set process.

The residual stresses abruptly decrease in the 5mm region from the boundary for SS400 and 10 mm for type 304. These differences of residual stress distribution are attributed to the effects of the heat conductivity, since the heat conductivity is 47.2 W/m/K for SS400, and is 19.0 W/m/K for Type 304 stainless Steel.

In this report, the mechanism of residual stress generation at the bonding boundary is discussed. The residual stresses generate in the cooling process after up-set process, and the differences of residual stress distribution are attributed to the effects of the heat conductivity.

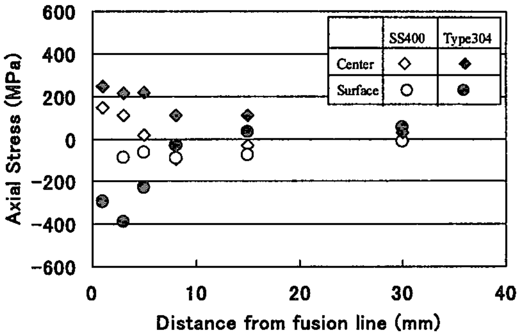

Fig.1 Residual stress distribution around the friction welding.

2.6.11 Neutron diffraction study of open tunnel oxide α-MnO_2

N. Kijima*, T. Ikeda[†], K. Oikawa[‡], F. Izumi[†], and Y. Yoshimura*

* *National Institute of Materials and Chemical Research, Tsukuba, Ibaraki 305-8565, Japan*
[†] *National Institute for Research in Inorganic Materials, Tsukuba, Ibaraki 305-0044, Japan*
[‡] *Japan Atomic Energy Research Institute, Tokai, Ibaraki, 319-1195, Japan*

Introduction

Alminosilicates, including zeolites, clay minerals, and mesoporus silicates, are well known families of porous crystals. Recently, much attention has been focused on the porous materials of transition metal oxides.

It is known that α-MnO_2 alone has a tunnel structure without any large stabilizing cations in its tunnel, whereas almost of porous manganese oxides have some large stabilizing cations in its tunnels. Rossouw *et al.* [1] have synthesized the α-MnO_2 specimen without any large stabilizing cations for the first time, whereas it might contain H_3O^+ in its tunnel. They have also investigated the crystal structure of hydrated and dehydrated α-MnO_2 specimens by using the neutron diffraction technique. However, nature and locations of residual H_2O molecules in its tunnel remain unclear at present.

We have recently succeeded in synthesizing a well-crystallized α-MnO_2 specimen by a redox precipitation using ozone oxidation. To verify and clarify the nature of residual H_2O molecules in the tunnel structure, neutron diffraction investigations have been made in this work.

Experimental

A well-crystallized α-MnO_2 specimen was prepared by oxidation of $MnSO_4$ with ozone gas in H_2SO_4 solution at 353 K. Scanning electron microscope images indicated the particles of the α-MnO_2 have needle-like crystals. This α-MnO_2 specimen contained residual H_2O molecules in its tunnels on the based of a temperature-programmed desorption (TPD) analysis.

Neutron powder diffraction data were taken at room temperature on the high-resolution powder diffractometer (HRPD) equipped with Si (533) monochromator with a neutron wavelength of 1.16 Å. Data were collected between $2\theta = 5°$–$165°$ with a step interval of 0.05°. The deuterated specimen was located in a cylindrical vanadium can with an inner diameter 12 mm. The collected data were analyzed by a Rietveld-refinement program RIETAN-2000, and the technique of partial profile relaxation was applied to a few reflections.

Results and discussion

Figure 1 shows the preliminary result of the Rietveld-refinement pattern for the neutron powder diffraction data of the deuterated α-$MnO_2 \cdot 0.3D_2O$ specimen at room temperature. The lattice constants are a = 9.7387(10) Å and c = 2.8438(2) Å. The technique of partial profile relaxation considerably improves fits between observed and calculated profiles, although highly asymmetric reflections due to anisotropic broadening.

The amount of water in the tunnel is estimated to be 0.1 per α-MnO_2 molecule from the result of the Rietveld-refinement, which is consistent with a result of the TPD analysis. These detailed experimental results will be published elsewhere [2]

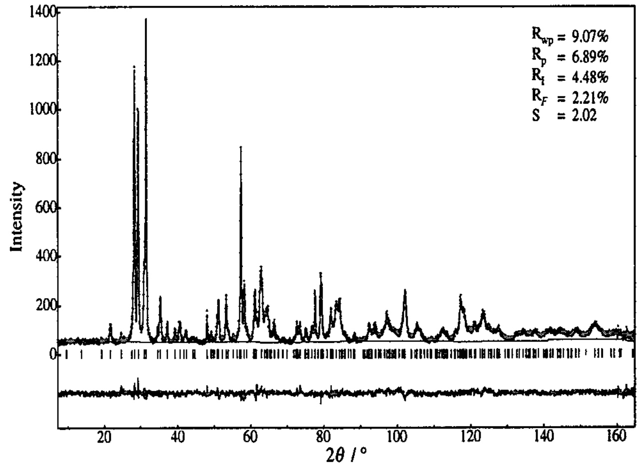

Fig. 1 Rietveld-refinement pattern for the neutron powder diffraction data of the deuterated α-$MnO_2 \cdot 0.3D_2O$.

References

[1] M. H. Rossouw *et al. Mat. Res. Bull.* 27, 221 (1992).
[2] N. Kijima *et al.*, in preparation.

2.6.12

Trial of Neutron Measurement of Stress in Cu Film Deposited on Glass Substrate

M. Nishida , T. Hanabusa[1] and N. Minakawa[2]

Kobe City College of Technology, Kobe 651-2194, Japan
[1] Faculty of Engineering, Tokushima University, Tokushima 770-8506, Japan
[2] Japan Atomic Energy Research Institute, Tokai, Ibaraki 319-1195, Japan

Recently, a variety of functional materials are vigorously developing in industrial fields. In mechanical as well as electrical field, diverse thin solid films are built on several kind of substrates. Multi-layer structure is also developed so as to bring out several functions. In these cases, development of residual stresses in the films is essential because of different mechanical and physical properties between the substrate and the film as well as among the layers. If residual stress becomes very large, the film may be destroyed and/or the characteristics of the film may change by the residual stress itself. Therefore, it is important to evaluate the behavior of residual stresses in the films in order to ensure a reliable function of the film structurs. The X-ray stress measurement technique has been applied to measure residual stresses in thin films. However, in the case of laminated films, residual stresses may not be able to measure because of a shallow penetration depth of X-rays. On the other hand, the penetration depth of neutron is much higher than X-rays. Therefore, the stresses in the sub-surface layers might be possible to meaure.

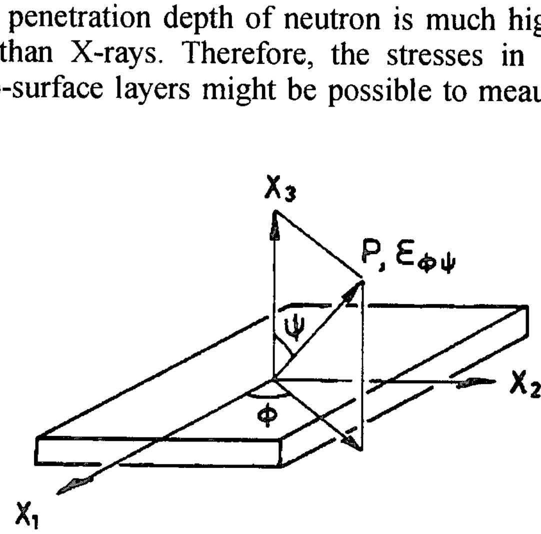

Fig. 1 Coordinate system for neutron stress measurement.

The present investigation is the first trial of measuring the stress in thin films by neutron diffraction.

This investigation made the measurement of residual stress in the Cu film deposited on a glass substrate and confirmed a possibility of the stress mesurement by neutron diffraction.

Cu thin films spattered on glass substrate were used in this investigation. Figure 1 shows a specimen coordinate system. We assume in this experiment that the state of residual stress in Cu film is an equi-biaxial, because the film is a mono-layered thin structure. In this case, the stress strain relation is considered as follows. The normal lattice strain $\varepsilon_{\phi\psi}$ in the direction defined by the angles ϕ and ψ is written as folows:

$$\varepsilon_{\phi\psi}=\frac{1+\nu}{E}\sigma\sin^2\psi-\frac{2\nu}{E}\sigma. \qquad (1)$$

Since $\varepsilon_{\phi\psi}$ is linearly related to $\sin^2\psi$, residual stress σ can be calculated from the slope of the straight line in $\varepsilon_{\phi\psi}$ - $\sin^2\psi$ relation. However, the present Cu film exhibits a high {111} preffered orientation so that the conventional $\sin^2\psi$ method cannot be applied. Therefore, the following equation[1)] is used to evaluate stress in the film, i.e., the two-exposure measurement (ψ=0°, 70.53°) was applied:

$$\sigma=\frac{E}{1+\nu}\ \frac{\varepsilon(\psi_1)-\varepsilon(\psi_2)}{\sin^2\psi_1-\sin^2\psi_2} \qquad (2)$$

From the results of neutron measurement, the measurable peak was 111 diffraction appeared at 2θ=60.1° in the "RESA" system. For the diffraction of low Bragg angle, the Ψ

- diffractometer method must be used in order to get the diffraction at large ϕ - angle. However, in a case of neutron diffraction, the glass substrate transmits the neutron beam very easily. Therefore, the Ω -diffractometer method can be used in the neutron stress measurement. Table 1 shows material parameters of Cu and measurement conditions.

Table1 Material parameters and measurement conditions.

Diffraction plate	Cu 111
Diffraction angle (deg.)	$2\theta = 60.1$
ϕ angle (deg.)	0, 70.53
Young's modulus E (GPa)	136
Poison's ratio ν	0.3
Neutron wave length λ (nm)	0.2091102

Before the stress measurement, the neutron diffraction pattern from 111 plane of Cu powder was measured. From this profile, a lattice spacing in stress free state is determined as d_o = 0.20869 nm. Since this value agrees very well with the hand book data, a considerable precision is expected in this investigation.

Figure 2 shows the rocking curve of 111 diffraction for the Cu film. This measurement was made of θ -scanning under the conditions of fixed 2θ angle at 60.149° . It can be seen from this result that the diffraction peak exists in the range of ± 10 degrees. Furthermore, it was identified that a orientation gap of about +3° exists against the normal of the substrate surface.

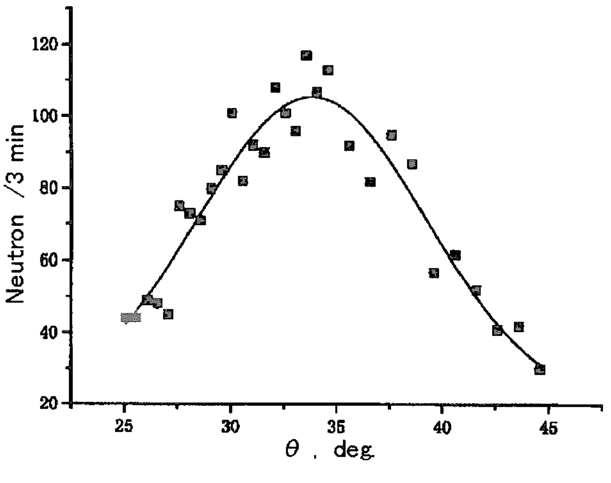

Fig. 2 Rocking curve of 111 plane in Cu film.

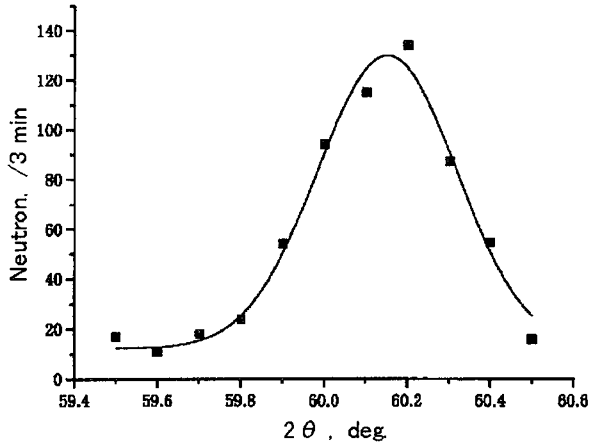

Fig. 3 Diffraction pattern of Cu film (ϕ =0).

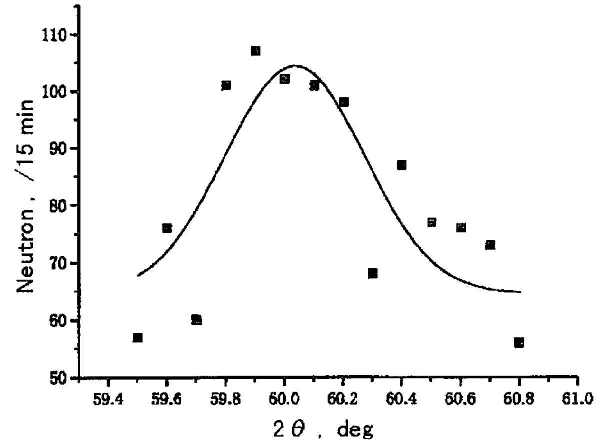

Fig. 4 Diffraction pattern of Cu film (ϕ =70.53°).

Figures 3 and 4 show the neutron diffraction patterns measured from the Cu 111 at the angles ϕ =0° and 70.53°, respectively. From these diffraction profiles the 2θ values were determined as:

$$2\theta_{(\phi=0^\circ)} = 60.150^\circ$$

$$2\theta_{(\phi=70.53^\circ)} = 60.034^\circ$$

and the stress in the film was evaluated by Eq. (2) as:

$$\sigma = 206\ \text{(MPa)}.$$

Form the above discussion, the neutron stress measurement method can be applied for the stress measurement of thin Cu film.

Reference

[1] T.Matsue et al., J. Soc. Mat. Sci., Japan, Vol. 44, No.504(1995) 1121-1126.

2.6.13 Neutron Phase Strain measurement in SiC Particulate Reinforced Aluminum Alloy during Fatigue

Yoshiaki AKINIWA, Keisuke TANAKA, Hidehiko KIMURA,
Noriaki MINAKAWA[1], and Yukio MORII[1]

Nagoya University, Nagoya 464-8603, Japan
[1]Japan Atomic Energy Research Institute, Tokai, Ibaragi 319, Japan

Aluminum alloys reinforced with silicon carbide particles (SiCp) are currently being considered for use as new structural materials in automobile and aerospace industries because of their low weight, high strength and high wear resistance. In metal matrix composites, the residual stress will be developed due to a mismatch of the coefficients of thermal expansion between the reinforcing particles and the matrix[1]. The thermal residual stress has a significant effect on the mechanical properties and fatigue strength of the composites.

Structural materials fracture when they are subjected to cyclic loading, even if the load is less than the static strength. This phenomenon is known as fatigue failure. For engineering components, clarification of fatigue properties and development in inspection procedures to detect fatigue damage are very important to obtain a good reliability.

In this study, silicon carbide particulate reinforced aluminum alloy was fatigued. The neutron diffraction method was used to measure the change of the phase strains of the composite during the fatigue process.

The experimental materials used were aluminum alloy reinforced by silicon carbide particles (SiCp/Al2024). The volume fraction of SiC particles of the composite is 20% and their average size is 3μm. The composite was fabricated by powder metallurgical processing. An extruded rod of the composite was heat-treated under T6 conditions. The grain size of the matrix is about 5μm. The Young's modulus is E=114 GPa, the 0.2% proof strength is $\sigma_{0.2}$=465 MPa and the tensile strength is σ_B=625 MPa.

The loading axis of the specimen is taken along the extrusion direction. Specimen with a thickness of 3 mm and a height of 6 mm was used.

Fatigue tests were conducted using a specially designed mechanical tensile testing equipped machine under a constant amplitude of stress cycling. The loading frequency was about 4/1000 Hz. The stress ratio is R=0.1. The maximum applied stress and the maximum strain were 465 MPa and 6600×10^{-6}, respectively.

The neutron diffractions from Al 200 and SiC 116 were used for stress measurement with the RESA (REsidual Stress Analyze equipment) at JAERI. The specimen was uniaxially strained with a tensile testing equipment. The wave length used was 2.068140Å. The direction of the lattice strain measured was parallel and perpendicular to the loading axis. The phase strains were measured at σ=46.5, 200 and 465 MPa. The strain was calculated on the basis of the lattice spacing of monolithic aluminum alloy and silicone carbide in stress free condition.

For the case of the first loading, both phase strains of composite increased with applied stress. When the plastic deformation occurred, the measured phase strain of aluminum alloy was less than that evaluated from the elastic relation. The strain decreased with number of stress cycles. On the other hand, the phase strain of SiC particles increased with number of stress cycles. In this fatigue condition, fatigue life expected was 7.5×10^3 cycles. The final number of stress cycles was 450 in this study. Further fatigue loading was necessary to detect the fatigue damage of the composite.

References

[1] Y. Akiniwa, K. Tanaka, T. Takezono, M. Hayashi, N. Minakawa and Y. Morii, J. Soc. Mater. Sci, Japan, 47 (1998), 755-761.

2.6.14

Measurement of Internal Stress Distributions in a High Pressure Cell Cylinder

A. Moriai [1,4], A. Onodera [2], F. Amita [3], A. Ohtomo [1], N. Minakawa [4,1] and Y. Morii [4]

[1] Department of Research Reactor, JAERI, Tokai, Ibaraki, 319-1195
[2] Graduated School of Eng. Sci., Osaka Univ., Toyonaka, Osaka, 560-8531
[3] Graduated School of Science, Kyoto Univ., Sakyo, Kyoto, 606-8502
[4] Advanced Science Research Center, JAERI, Tokai, Ibaraki, 319-1195

High pressure devices are powerful tools for neutron scattering studies to give knowledge of interesting behavior come from changes in interatomic distances in the matters. Of some kinds of the devices, a piston-cylinder cell is most commonly used in the field, but it cannot exceed the pressure of ~3 GPa (high pressure limit, HPL). The HPL of the cell depends on geometry of the cylinder (and its surrounding components) as well as mechanical properties of the materials. While these factors are usually determined through stress analysis, no attempt has been made by experimental methods enabling to detect stress in deep inside the objects.

To newly develop and upgrade piston-cylinder cell with a greater HPL, we have investigated non-destructively internal stress distributions in the cylinder by neutron diffraction method.

A sample is a sintered-Al_2O_3 cylinder of a piston-cylinder type cell [1]. The cylinder has a biconical shape with 20° tip angle in both ends. The dimensions are 50 mm in height, 32 mm in outermost diameter and 8 mm in bore diameter. The cylinder is provided prestress radially by force-fitting two wedge rings into itself to sustain the expansion from inner pressure. Fig. 1 shows a selected region (shaded area) in the sample to take diffraction data.

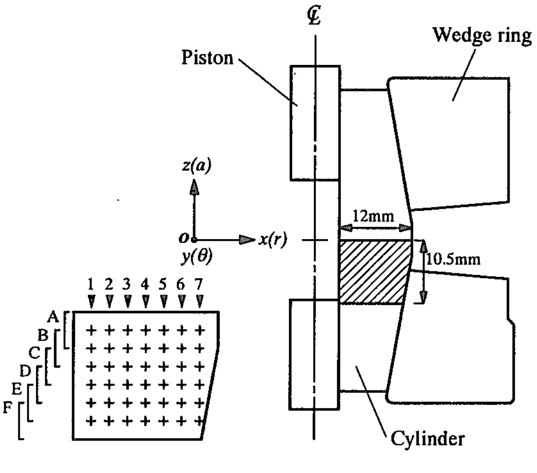

Fig. 1 A cross section for a sintered-Al_2O_3 cylinder of a piston-cylinder high pressure cell. Shaded area in the center of the cylinder was measured to yield neutron diffraction data.

To define small gauge volume inside the region, incoming and diffracted neutrons were limited by setting Cd slits (3×3 mm^2) in front and behind the sample, and then the region was scanned to collect α-Al_2O_3 (113) reflection every 42 gauge volumes of A-1 ~ F-7 in the directions of three principle stresses, x (corresponding to radial stress σ_r), y (hoop stress σ_θ) and z (axial stress σ_a). Measuring the (113) plane spacing, $d_0{}^{113}$ at 0.0 GPa in the cylinder and d^{113} at 0.8 GP, we obtained average strain in each gauge volume by $\varepsilon_i{}^{113} = (d_i{}^{113} - d_{0,i}{}^{113}) / d_{0,i}{}^{113}$, ($i = r$, θ and a). The stresses, σ_r, σ_θ and σ_a were derived from Hook's law as Young's modulus, E, and Poisson's ratio, ν, of the cylinder material kept constant as 372.65 GPa and 0.19, respectively. Radial stress σ_r, for example, is given by following equation

$$\sigma_r = \frac{E}{1+\nu}\left\{\varepsilon_r^{113} + \frac{\nu}{1-2\nu}\varepsilon_r^{113} + \varepsilon_\theta^{113} + \varepsilon_a^{113}\right\}$$

The diffraction measurements were carried out at na incoming neutron wavelength of 0.21 nm using the diffractometer for residual stress analysis, RESA, at JRR-3M guide hall in JAERI. The inner pressure in the cylinder was calibrated by measuring change in lattice parameter of NaCl single crystal placed into the cylinder. The wedge rings were forced into the cylinder at a load of 7845 N (0.8 ton) before generating pressure.

Unfortunately, the results of the stress analysis cannot be shown in the issue, because some gauge volumes remain unmeasured and the first operating cycle of JRR-3M in this fiscal year has been discontinued due to its unforeseen trouble. A complete data set giving the three principal stresses will be able to acquire within early time of the year, and then we will report the results of the study in the first international symposium on advanced science research (ASR-2000) to be held at Tokai in the year's autumn.

References

[1]A. Onodera *et al.*, Jpn. J. Appl. Phys. **26** (1987) 15

2.7 Fundamental Physics

2.7.1 Neutron Interferometric Measurement of the Scattering Lengths of ^{202}Hg, Hg, ^{63}Cu, ^{65}Cu, Cu and W

Hiroshi TOMIMITSU[a], Yuji HASEGAWA[b] and Kazuya AIZAWA[a]

[a]Advanced Science Research Center, JAERI, Tokai-mura, Ibaraki-ken, 319-1195 Japan
[b]Department of Applied Physics, University of Tokyo, Hongo, Bunkyo-ku, Tokyo113-8656, Japan

We successfully determined the coherent neutron scattering lengths for ^{202}Hg, first in the world, and for several elements and isotopes, with very high accuracies.

Measurements were carried out with a Si LLL-type interferometer at the special apparatus "PNO" implemented at JRR-3M. Temperature at the interferometer was kept around the RT +/-0.005deg. Wavelength, 0.15784nm, was selected so as to realize the best visibility of the interference oscillation curve of a reference Al plate, in combination with the position of the interferometer. The best visibility, thus surveyed, was more than 50%, while it was around 40% in the previous experiment[1].

Every sample was set so as to receive only the reflected beam only between the 1'st(splitter) and the 2'nd(mirror) reflecting plate of the interferometer, as shown in Fig.1.

Compared with the previous experiment[1], samples in the present experiment were rotated much wider, which also improved the quality of the final data.

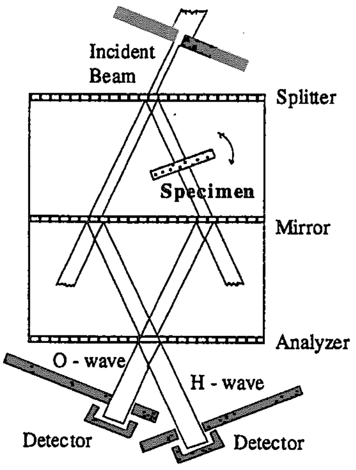

Fig. 1. Drawing of the experiment with the beam paths.

With the fitting parameters A~E, the intensity I for O-wave is analyzed by the following function[1];

$$I = A*\cos(B/(\cos(\alpha + C)) + D) + E. \quad .....(1)$$

The coherent scattering length, b, is then derived through the relation below, with N: atomic number density, t: thickness and λ: wavelength;

$$B = N*b*\lambda*t. \quad .....(2)$$

Example of the interference oscillation is shown below (Fig.2); for the case of ^{202}Hg, with a least squares fit.

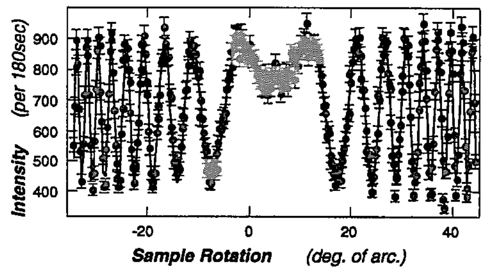

Results for b's are summarized below, comparing with the tabulated values[2].

Specimen	b(derived, fm)	b(Table, fm)
nat. W	4.7300(0.0271)	4.77~5.1
^{63}Cu	6.5033(0.0103)	6.40, 6.72
^{63}Cu	10.1694(0.0167)	10.57, 11.09
nat. Cu	7.7093(0.0044)	7.35 ~7.90
^{202}Hg	11.0019(0.0440)	*none*
nat. Hg	12.5951(0.0461)	12.66~13.10

References

[1] H.Tomimitsu, Y.Hasegawa, K.Aizawa and S.Kikuta: Nucl. Instr. Meth. in Phys.Res. **A420** (1999) 435.

[2] L.Koester, H.Rauch and E.Seymann: *Atomic Data and Nuclear Data Tables* 49 (1991), pp 65-120.

2.8 Instrumentation and Methods

2.8.1 APPLICATION OF A STACKED ELASTICALLY BENT PERFECT SI MONOCHROMATOR WITH IDENTICAL CRYSTALLOGRAPHIC PLANES AT A DIFFRCATOMETER FOR BIO-MACROMOLECULES (BIX-3)

I. Tanaka[1], F.U. Ahmed[1,2], N. Niimura[1]

[1]ASRC, Japan Atomic Energy Research Institute, Tokai, Ibaraki 319-1195, Japan
[2]On leave from Inst. of Nucl. Science and Tech., Atomic Energy Res. Est., Bangladesh Atomic Energy Commission, Dhaka-1000, Bangladesh

Neutrons have a great potential as a probe to investigate soft and hard materials, but the low intensity of incident neutrons is always a big obstacle compared to the intensity of X-rays. In order to overcome this, elastically bent perfect silicon(EBP-Si) monochromator was used to increase the flux. The merit of using EBP-Si has been already reported by authers and by others. The high-transmission property of EBP-Si for 1-3 Å thermal neutrons is specially noted here. Up to the present some investigators installed stacked identical crystal planes of EBP-Si as a monochromator and an analyzer in a TAS machine at ILL, France to increase the supplementary gains in intensity.

The intensity at the sample position of a diffractometer for studies of biological macromolecules (BIX-3) for two identical (*hkl*) planes stacked EBP-Si monochromator was compared with that for single EBP-Si. A single plate of EBP-Si with 250 x 40 mm^2 surfaces of (111) and 5 mm in thickness, was setup in the monochromator housing of a TAS at JAERI, Japan (TAS-2). The optimum curvature of this monochromator was determined using a neutron imaging plate (NIP), by placing it at the same distance as MtoS (2.3 m) of BIX-3, in open geometry (no soller slits) when the maximum peak intensity was observed at -350 μ deformation strain on the scale of a strain gauge connected to the concave side of the monochromator crystal, which corresponded to a radius of curvature of 10 m. It should be noted that the difference in the peak intensity of EBP-Si for the deformation strain from -350 to -400 μ was within 2%, i.e. intensity gain was almost saturated. Then, two 5 mm thick identical Si (111) plates, the total 10 mm, were stacked, bent and aligned. When the deformation strain reached to -350 μ, the peak intensity increased by a factor of 1.61 compared to that of a single plate. The aligning step sizes for ω, Rx and X were 0.1°, 0.2° and 1.0 mm, respectively.

The optimized EBP-Si was installed in the monochromator housing of BIX-3 without any modification. The experiments were carried out for the single plate EBP-Si (5 mm thickness) and the stacked plates EBP-Si (2 times 5 mm thickness) with a strain of -400 and -350 μ, respectively. The neutron wavelength was 2.35 Å with $2\theta_M = 44°$ for these experiments. The flux measurements were carried out by using an NIP at the sample position of BIX-3. The improved ratios of peak and integrated intensities were 1.60 and 1.59, respectively, when a single EBP-Si (5 mm thick) plate was replaced with stacked EBP-Si plate (2 times 5 mm thick). Fig. 1 shows the result of the profiles at each peak. The abscissa is the position on the NIP and the ordinate is the linear intensity. The diffraction spots on the detector were found well separated to determine the indices of protein diffraction[1].

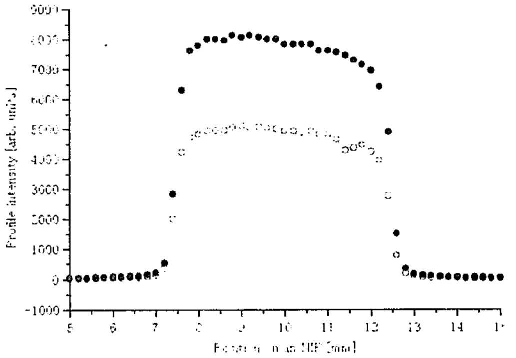

Fig.1. Profile intensity comparison between the two (111) planes stacked EBP-Si monochromator (solid circles) and a single one (open circles).

Reference

[1] I. Tanaka, F. U. Ahmed and N. Niimura, Physica B **283** (2000) 295.

2.8.2

An Attempt to refrigerate Si-crystal optical component on a Double Crystal Diffractometer

K. Aizawa and H. Tomimitsu
Advanced Science Research Center, Japan Atomic Energy Research Institute, Tokai,Ibaraki 319-1195, Japan

It is well known that a deviation from the theoretical rocking curve in the region where intensities are less than ~1/100 of peak is observed in a double crystal diffractometer using perfect Si single crystals of non-dispersive setting. There are several possibilities to explain this situation. For example, imperfections of the lattice planes or roughness of surface of Si crystals are conceivable. On the other hand, another possible explanation would be the influence of thermal diffuse scattering of Si crystals. For this reason we attempted to refrigerate the Si crystals to reduce thermal diffuse scattering to compare with the theoretical rocking curve.

Experiments were performed at the PNO apparatus at the JRR3-M research reactor in JAERI. The configuration of the double crystal diffractometer was (5,-5) setting of (111) symmetrical reflection. The wavelength used of this study was 0.25nm. Because of the difficulty of setting up a double crystal diffractometer refrigerating both first and second crystals, we started by refrigerating only the second crystal. Because the lattice constant of Si is almost constant to temperature under 50 K and it is better to refrigerate to lower temperature to remove thermal diffuse scattering, we attempted to refrigerate the second crystal about 10 K. We used CRYODYINE® REFRIGERATION SYSTEM produced by CTI-CRYOGENICS Helix Technology Corporation. The second crystal was isolated from vibration generated by a compressor. Figure 1 shows rocking curves at room temperature and 14.78K together with theoretical curve (Ewald curve) in log-log scale. Peak intensities for both refrigerated and theoretical rocking curves are scaled to peak intensity of rocking curve at room temperature. Broadening of the full width at half maximum (FWHM) of the second crystal rocking curve was observed in Fig.1. We think that this effect may be attributed to the breaking of non-dispersive condition due to small lattice-parameter change in the second crystal at 14.78K. Calculation of this effect is in progress. As for tail of the rocking curve, it seems to be reduced. Now, we are planning to refrigerate both 1st and second crystals.

From the viewpoint of very small-angle neutron scattering (VSANS) method, the broadening of FWHM of rocking curve of second crystal corresponds to extend to measurable q-range toward higher q-values. So, refrigerating a second crystal seems to be useful option for VSANS.

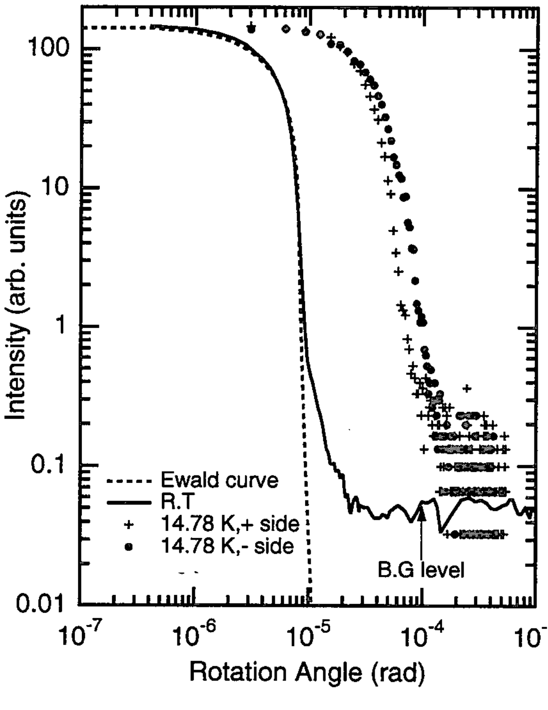

Fig. 1 Ewald curve, rocking curve at room temperature and 14.78K

2.8.3

Development of Compound refractive optics and evaluation of a quadrupole magnet as a neutron prism.

T. Oku, S. Morita, S. Moriyasu, Y. Yamagata, S. Ohmori, H.M. Shimizu, T. Hirota[1],
Y. Kiyanagi[1], T. Ino[2], M. Furusaka[2], and J. Suzuki[3]

RIKEN, 2-1 Hirosawa, Wako, Saitama 351-0198, Japan
[1]Hokkaido University, Sapporo 060-8628, Japan
[2]Inst. of Mater. Struct. Sci., High Energy Accel. Organ., 1-1 Oho, Tsukuba, Ibaraki 305-0801, Japan
[3]Japan Atomic Energy Research Institute, Tokai, Ibaraki 319-1195, Japan

Neutron scattering method is essential in a study of internal structure and dynamics of material due to the exclusive nature of a neutron. However, owing to the extremely low intensity of the neutron beam compared with the synchrotron-radiation photoemission, it can be restrictedly applied. To improve this situation, we have been developing neutron optical devices based on neutron refractive optics, such as a neutron lens and a neutron prism. In this study, we have developed compound refractive lens for cold neutrons and evaluated the function of a quadrupole magnet as a neutron prism.

So far, the result of a neutron beam focusing experiment using MgF$_2$ compound refractive lens (CRL) which has symmetric concave shape was reported 1). In their experiment, the neutron intensity gain of over 30 was obtained. However, the neutron transmission is drastically decreased with increasing the neutron beam size due to the lens shape, i.e., the effective lens thickness increases with the neutron beam size. To overcome this problem, we have developed a fresnel lens for neutrons which is made from vitreous silica with effective potential of (90.1–2.7x10^{-4}i) neV. This lens was grinded out from a vitreous silica disk using Electrolytic In-Process Dressing (ELID) Grinding Technique 2). The cross section of the lens is depicted in Fig.1. The surface roughness R$_y$ of the lens was measured to be less than 0.1μm. The lens was investigated with cold neutrons using a neutron spectrometer SANS-J installed at JRR-3M of JAERI. The experimental setup is shown in Fig.2. To evaluate performance of the lens accurately, the neutron beam collimated by a slit with 1mmφ pinhole was employed, and the neutron intensity distribution on the surface of the 2d-PSD was measured with shifting the lens position, X$_{lens}$, perpendicular to the neutron beam. Fig.3 shows the intensity distribution along the x-axis on the surface of 2d-PSD. The peak shifts of the intensity distribution was observed as the lens shifts away from the center position. This indicates that the neutron beam is refracted by the passage through the lenses, and

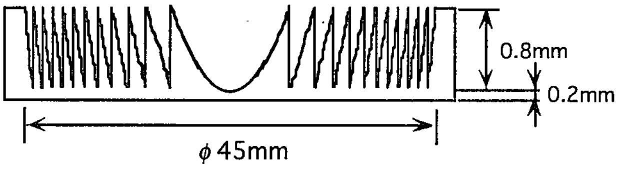

Fig. 1 Cross section of vitreous silica fresnel lens.

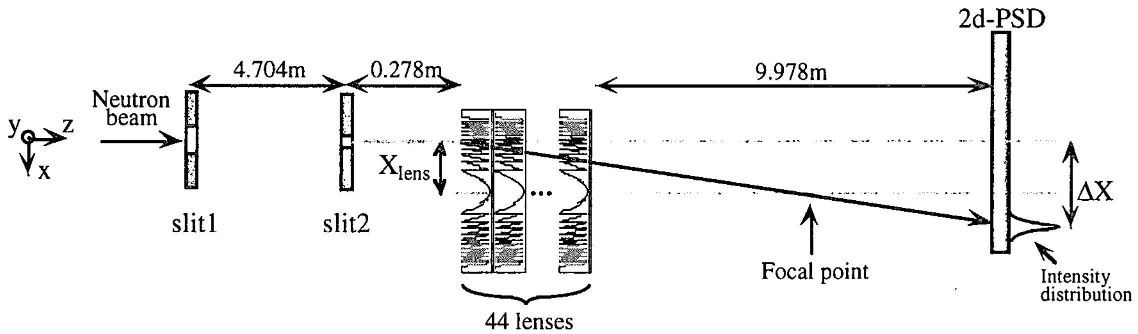

Fig. 2 Experimental setup: Slit 1 and 2 have pinholes with 7 and 1 mmφ, respectively.

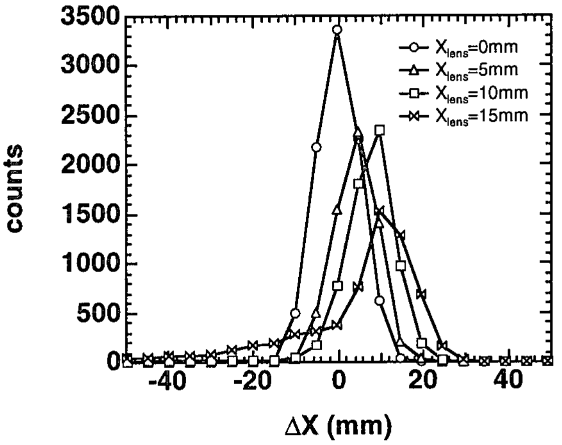

Fig.3. Horizontal intensity distribution on the surface of the 2d-PSD.

the focal length was estimated to be 14m for 10Å neutrons. Also, relatively large neutron transmission of 64% is obtained even for 40mm beam size at neutron wavelength λ=10Å resulting from the shape. It is expected that the compound refractive lens which has aperture and refracting power large enough for practical use can be realized by selecting the lens shape and material.

In the quadrupole field given by $|\boldsymbol{B}|=C_Q(x^2+y^2)^{1/2}$, neutrons are accelerated following the equations: $d^2x/d\theta^2=\mp x\rho_0/(x^2+y^2)^{1/2}$, $d^2y/d\theta^2=\mp y\rho_0/(x^2+y^2)^{1/2}$ for positive and negative spin polarity, where $\theta=\omega t$, $\omega^2=|C_Q\mu/m|/\rho_0$ and ρ_0 is the radius of the quadrupole magnet aperture. In the special case of y=0, the equation is simplified as $d^2x/d\theta^2=\mp\rho_0$, which clearly visualizes a prism function according to the constant acceleration.

We have constructed a permanent quadrupole magnet with ρ_0 = 3.5 mm 3). The strength of the magnetic field was $\omega\sim$ 480 s^{-1}. We measured the prism function of the quadrupole magnet using cold neutrons from a reactor neutron source JRR-3M of JAERI. The neutron has the wavelength resolution of $\Delta\lambda/\lambda=0.129$. The length of the quadrupole magnet was L_1 = 0.45m and the distance between the magnet and the position sensitive detector (PSD) was L_2 = 9.7 m as shown in Fig.4. A two-dimensional neutron image obtained by the PSD is shown in Fig.5 (a) and (b). The neutrons are split into two regions due to the spin selectivity of the prism. The experimental image was well reproduced by the numerical calculation with a collimator misalignment of (x, y)=(-1.0 mm, -0.45 mm) as shown in Fig.5(c) and (d).

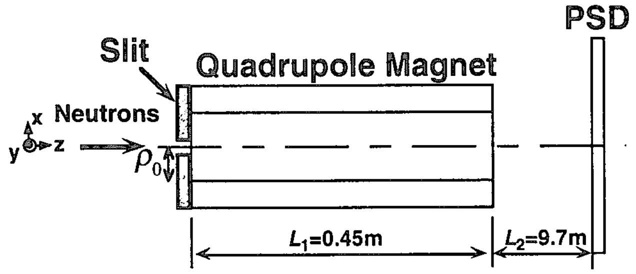

Fig.4. The experimental setup for the study of the neutron prism.

The prism with PSD is capable to analyze the neutron energy and is applicable to inelastic scattering instruments using pulsed neutrons. With a non-monochromatic neutron beam, all components of incident and scattered momentum vectors can be measured by tracing back the arrival time of incident neutrons from the timing of PSD signals. A favorable energy resolution can be achieved in a wide range of energy transfers using a highly collimated incoming beam and a PSD with good position and time resolution.

References

[1] M.R. Eskildsen et al., Nature 391 (1998) 563.

[2] H. Ohmori, Int. J. Japan Soc. Prec. Eng., Vol.26, No.4 (1992) 273.

[3] T. Oku et al., Physica B, 276-278 (2000) 112.

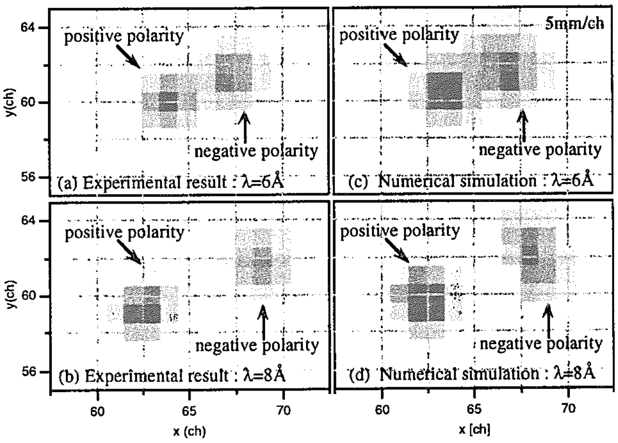

Fig.5. Two-dimensional distribution of neutron intensity at the surface of the 2d-PSD:(a),(b):experimental result, (c),(d):numerical simulation

2.8.4 Cold neutron imaging detector with two scintillator

F. Tokanai, T. Oku, K. Morimoto, H. M. Shimizu, J. Suzuki[1], T. Ino[2], T. Ikeda,
W. Ootani, C. Otani, H. Sato, Y. Kiyanagi[3], T. Hirora[3], K. Kuroda[4], A. Riazantsev[3]

RIKEN , Hirosawa, Wako, Saitama 351-0198, Japan,
[1]Japan Atomic Energy Research Institute, Shirane, Tokai, Naka, Ibaraki 319-1195, Japan
[2]Institute of Materials Structure Science High Energy Accelerator Research Organization
KEK, Oho, Tsukuba, Ibaraki 305 -0801, Japan
[3]Faculty of Engineering, Hokkaido University, Sapporo 060-8628, Japan
[4]CERN Div. EP, 1277 Geneva 23 Switzerland

Recently, the project of spallation neutron source has been started in Japan, Europe and the United States aiming at starting operations at the beginning of the 21st century. Neutron imaging detector for the spallation neutron source will be required large area with good position information, high detection efficiency, and fast response for timing information on individual neutron signals or for counting neutrons at a high counting rate. We are currently developing two cold neutron imaging detector based on GSO scintillator and ZnS scintillator coupled to wave-length shifting fiber. In this report, the progress of these detector will be presented.

Cerium-doped Gd_2SiO_5 (GSO) [1)] contains Gd in the compound and has potential application as an efficient neutron detector due to the very large neutron absorption cross section of Gd amounting to 49700 b. The absorption cross section of Gd comprises 61100 b for ^{155}Gd (14.8% abundance) and 259000 b for ^{157}Gd (15.7%). The neutron absorption reactions by ^{155}Gd and ^{157}Gd produce conversion electrons with energy ranging from 30 keV to 250 keV and γ-rays up to 2 MeV through the cascade of deexcitation of the excited ^{156}Gd and ^{158}Gd. Thus, Gd and the its compounds have been applied to neutron radiography as a versatile neutron converter for neutron imaging plates and as a Si-based neutron detector. Therefore, a thin GSO crystal is sufficient to absorb slow neutrons which enables the influence of background γ-ray signals to be suppressed. In addition, GSO has a short decay time constant of 60 nsec which are suitable for measuring the arrival time of individual neutrons from a pulsed neutron source at a high counting rate and with a good signal-to-noise ratio. However, only a few attempts have been reported on the detection of cold neutrons with a GSO scintillator.

We investigated the characteristics of a GSO scintillator by using a cold neutron beam at the C3−2 beamline of the JRR-3M research reactor of JAERI. The wavelength of incident cold neutrons was 6 Å with a wavelength resolution of 13.5% (FWHM). A GSO crystal of 50 mm × 50 mm × 0.5 mm was attached with optical grease to a 2 inch diameter Hamamatsu H1949-50 photomultiplier tube (PMT). The GSO crystal had a Ce concentration of 0.5%mol provided by Hitachi Chemical Co. Ltd. The obtained pulse height spectrum of 0.5 mm thick GSO scintillator is indicated as 'Neutron On' in Fig. 1. The 31 keV and 81 keV peaks resulting from neutron absorption by Gd nuclei were identified in the pulse height spectrum by using a photomultiplier tube.

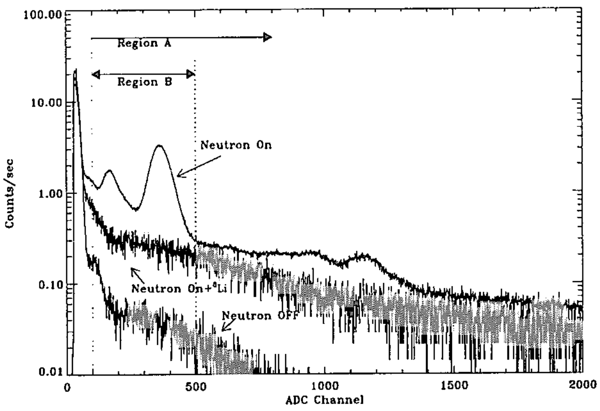

Figure 1: Pulse height spectrum of GSO for 6Å cold neutrons which is labeled as 'Neutron On'. he background spectrum from the beam line and the intrinsic background spectrum are respectively labeled as 'Neutron On + ^{6}Li' and 'Neutron Off'.

Imaging capability was studied by using an image intensifier with a CCD camera H4693FCCD). Figure 2 shows the neutron image obtained for neutron beams defined by LiF collimator of 1 mm with an image intensifier and viewed by a CCD camera. Image of 1.5 mm in diameter were observed for 1 mm diameter incident beams with corresponding to a position resolution of 1.3 mm (FWHM). A better position resolution can be achieved by employing a thinner GSO scintillator (see more detail reference 2).

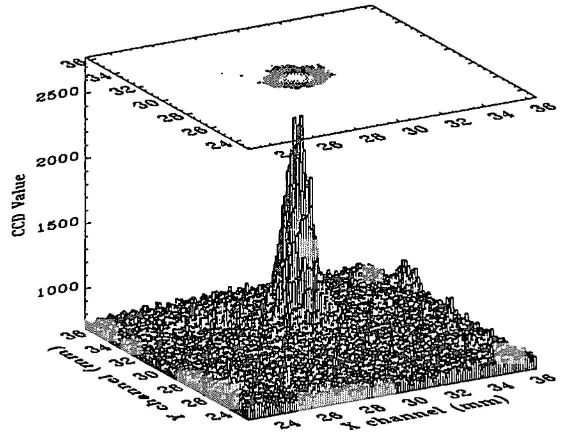

Figure 2: Two-dimensional image of the 1 mm diameter neutron beam obtained with a 0.5 mm thick GSO and an image intensifier with a CCD camera.

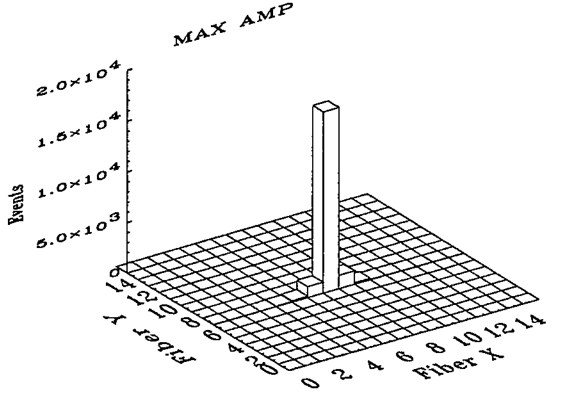

Figure 4: Two-dimensional image of the 1 mm diameter neutron beam obtained with a WLS fiber + ZnS scintillator detector. 1 bin is corresponding to 1mm.

Other neutron imaging detector was firstly developed by Kuroda[3]. It consists of a ZnS(Ag)^{6}Li scintillator of 20 mm × 20 mm × 0.5 mm (Bicron BC-704) and 16 wave-length shifting (WLS) fibers optically glued onto the up- and down-sides. The arrays were placed in orthogonal directions to supply two dimensional readout. The WLS fibers (Kuraray Y11) cross-section are 1 mm × 1mm , far ends were covered with Al mirror. The WLS fibers were attached with optical grease to a Hamamatsu H6568 16-channel multi-anode photomultiplier tube (MAPMT). Figures 3 shows the imaging detector.

The performance of the neutron imager was investigated by using a cold neutron beam at the C3−2 beamline of the JRR-3M research reactor of JAERI. The wavelength of incident cold neutrons was 10 Å with a wavelength resolution of 12.9% (FWHM). The last dynode signals from MAPMTs in X and Y planes were sent to standard discriminators with a threshold low enough to recored single photoelectrons. The total charge of the individual output signals from the MAPMT was analyzed with a charge-sensitive ADC device (LeCroy 2249W) with a logic gate of 400 nsec width, and data were accumulated event by event through a CAMAC bus in a personal computer. Total number of the readout channels was 34 (X:16 anodes, Y:16 anodes, 2 last dynodes). The dead time of the data acquisition system was 400 μs on average.

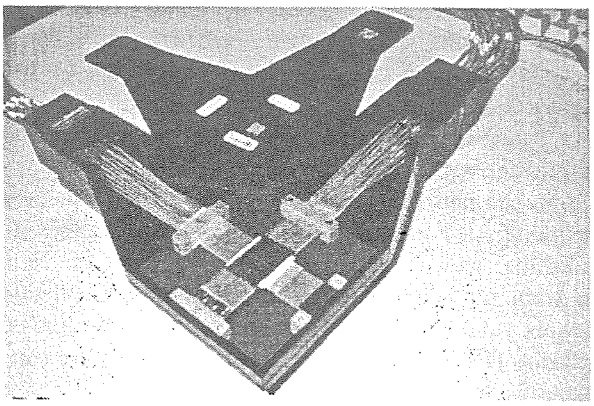

Figure 3: Neutron imaging detector with WLS fiber + ZnS scintillator.

Figure 4 shows the neutron image obtained for neutron beams defined by a 1 mm diameter cadmium collimator. Hit position of a cold neutron was determined by the applying the maximum amplitude algorithm on the anode signals. We obtained the position resolution of 1 mm (FWHM). The measured detection efficiency was about 56%. In order to estimate the neutron absorption in a fiber array, we measured the count rates with and without the fiber layer in front of a conventional ^{3}He proportional counter. The measured neutron absorption was about 38%. Taking into account the neutron absorption, the measured detection efficiency is almost consistent with the calculated efficiency.

We are developing a very large neutron imaging detector with a ZnS(Ag)^{6}Li scintillator of 100 mm × 100 mm × 0.5 mm and 256 WLS fiber (cross sectuion of 0.5 mm × 0.5 mm).

References

1) K. Takagi and T. Fukazawa, Appl. Phys. Lett., 42, (1983), 43

2) F. Tokanai, K. Morimoto, T. Oku, J. Suzuki, T. Ino, W. Ootani, C. Otani, H. Sato, H.M. Shimizu, Y. Kiyanagi, T. Hirota, Nucl. Instr. and Meth. A to be published.

3) K. Kuroda and I. Manuilov., Nucl. Instr. and Meth. A, 430, (1999), 311

2.8.5

PERFORMANCE OF A MULTI-WAVELENGTH MONOCHROMATOR SYSTEM FOR NEUTRON SINGLE-CRYSTAL AND POWDER DIFFRACTION

F. U. Ahmed[1, 2], I. Tanaka[1], N. Niimura[1]

[1]Advanced Science Research Center, JAERI, Tokai, Ibaraki 319-1195, Japan
[2]On leave from Inst. of Nucl. Science and Tech., Atomic Energy Res. Est., Bangladesh Atomic Energy Commission, Dhaka-1000, Bangladesh

Elastically bent Si crystals have been developed and used in diffractometers to increase the neutron flux density at the sample position. It was reported by authers that the intensity gain for a bent crystal was about 30 times that of a flat perfect crystal. This result must encourage the use of low/medium flux reactors for diffraction experiments by developing bent monochromators with optimum curvature. The focusing principle enables diffraction experiments with a signifcantly higher angular resolution and a broader wavelength distribution without using flux-reducing Soller collimators. Recently, it is reported that a two-wavelength sandwich monochromator to investigate stress/strain of polycrystalline materials had successfully been used. Previously, one of the authers also proposed using a curved monochromator assembly composed of several different types and segments of crystals to diffract and focus neutrons of different wavelengths onto the sample. When multi-wavelength and quasi-Laue methods are applied to crystallography dealing with larger unit cells (for example, proteins), the multi-wavelength methods produce better quality data, although data collection times are a little longer. Higher signal to background ratios can be achieved with multi-wavelength methods than with quasi-Laue methods owing to the different way of scanning the lattice points in reciprocal space. It is therefore preferable to obtain better quality data though expending a little more time in the case of multi-wavelength methods. Major aims of the present study were to employ the neutron imaging plate (NIP) detector and elastically bent perfect crystals for a multi-wavelength monochromator system to improve the data collection efficiency and improve the reliability of the experiments.

In order to improve significantly data collection efficiency, the advantages of using multi-wavelengths in single-crystal neutron diffraction as well as in powder neutron diffraction were established by experiments using a stacked monochromator assembly of two elastically bent perfect Si(111) and Si(220) crystals. Each crystal was elastically bent in order to increase the flux density at the sample position. Two wavelengths, λ_1 = 1.80 Å for Si(220) and λ_2 = 2.94 Å for Si(111), were selected. The alignment of the stacked monochromator was successful and a well defined rocking curve of approximately 0.3° full width at half-maximum (FWHM) was obtained. Diffraction patterns of Si powder were collected using the TAS-2 point detector as well as a neutron imaging plate (NIP) detector to compare the relative performance of the two detector systems (Fig.1). With the NIP detector, it was possible to acquire multiple reflections simultaneously with better intensity, better statistics and higher spatial resolution with an open geometry. The NIP detector was used to obtain the diffraction pattern of a single crystal of the organic compound piperidine cobaloxime. For the systems investigated in this study, it was possible to assign unambiguously rings or spots to diffraction by λ_1 or by λ_2 in the case of powder and single-crystal diffraction [1].

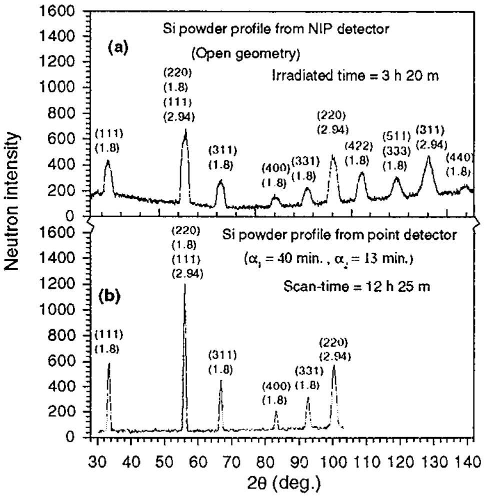

Fig.1. The powder diffraction profiles of Si powder for the multi-wavelength monochromator system obtained using (a) the NIP detector, (b) the point detector of TAS-2.

Reference

[1] F. U. Ahemd, I. Tanaka and N. Niimura, J. Appl. Cryst. **33** (2000) 291.

2.8.6 Development of Double-Focused Si Monochromator

H. Kimura[1], A. Kojima[1], R. Kiyanagi[1], Y. Noda[1], N. Minakawa[2], Y. Morii[2], N. Takesue[3], and Y. Yoshizawa[3]

[1]*Research Institute for Scientific Measurements, Tohoku University*
[2]*Advanced Science Research Center, Japan Atomic Energy Research Institute*
[3]*Institute for Solid State Physics, the University of Tokyo*

We have developed Four circle Off-centered Neutron DiffractometER (FONDER) at T_{2-2} beam port to carry out single crystal structural studies. Since before the incident neutron wavelength was fixed at 2.435 Å by using PG(002) monochromator, measurements at high-Q region had not been available. In order to obtain much shorter wavelength, a double-focused monochromator using Si single crystals has been developed. As shown in Figure 1, nine-Si single crystal plates are aligned vertically, and they can be rotated by the horizontal rod with a pulse motor. In addition, the each single crystal can be bent horizontally on the monochromator. Thus the monochromatized beam can be focused vertically and horizontally at a sample position.

In the present work, we optimized the amplitude of horizontal bend and assembled the Bragg reflection planes as a nine-vertically aligned crystal. (4 2 2) reflection was chosen as a monochromator in order to obtain $\lambda = 1.5$ Å neutrons at $2\theta_M = 90°$. The experiments were carried out with TAS-2 spectrometer at T_{2-4} beam port. Incident neutron wavelength was fixed at 1.567 Å where the flux of neutron in T_2 thermal guide is maximum. (4 2 2) peak intensity as a function of strain inside the bent crystal is shown in Figure 2. The peak intensity increases with increasing the strain because the extinction effect is reduced. The intensity starts saturating around 300 μ strain (indicated with an arrow in the Figure 2), of which value corresponds to 70 % of strain where the Si single crystal was broken. Therefore we applied the same strain (300 μ) for nine crystals. All the bent crystals mounted in the monochromator (Figure 1) was assembled along $< 4\ 2\ 2 >$ axis. As shown in Figure 3, rocking curves of (4 2 2) reflections for all the crystals are perfectly identical, which means that all of the vertically aligned crystals have the same line-widths, intensities, and peak positions.

At this moment, the double-focused monochromator tuned at the present work is installed at T_{2-2} port for further tuning at this beam port. The neutron intensity monochromatized by the new monochromator is a half comparing with that by PG(002) monochromator.

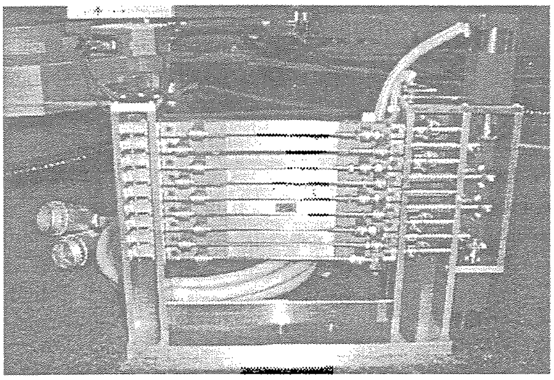

Figure 1: Horizontally and vertically focused monochromator.

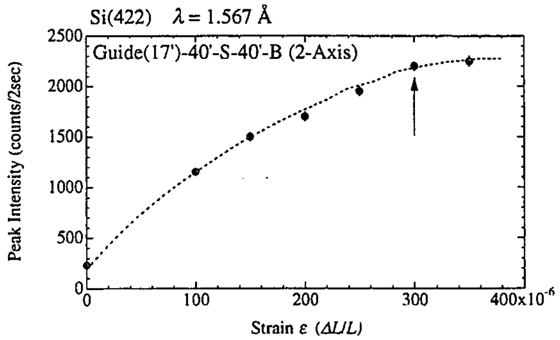

Figure 2: Strain dependence of the (4 2 2) Bragg peak intensity.

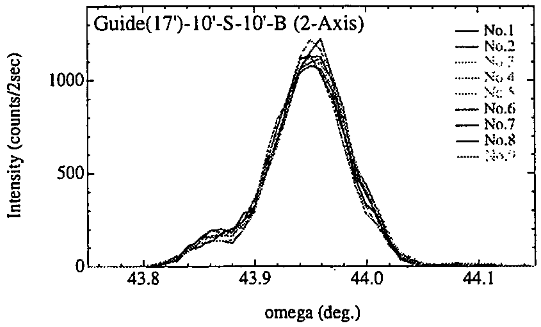

Figure 3: Rocking curves of (4 2 2) Bragg peak for vertically aligned crystals.

2.8.7

Characterization Study of a troidal bent pyloric graphite Neutron Condenser lens

N. Nishiki, N. Metoki[1], Y. Koike[1], K. Soyama[3], S. Fujiwara[1], Y. K. Haga[1], S. Koizumi[1]

Matsushita Electric Industrial Co., Ltd. 1006 Kadoma, Kadoma 571, Japan
[1]ASRC-JAERI, Tokai, Naka, Ibaraki 319-1195, Japan
[2]Japan Science and Technology Corporation, Kawaguchi, Saitama 332-0012, Japan
[3]Center for Neutron Science, JAERI, Tokai, Naka, Ibaraki 319-1195, Japan

There is strong demand to obtain high flux neutron which is an inevitable probe for the fundamental research as well as industrial use. Especially neutron imaging attracts strong interest in addition to the traditional method like scattering technique or activation analysis. For these purposes sophisticated neutron optical device has to be developed and used with a high-density neutron storage media like neutron image plate.

Very recently double bent pyloric graphite (PG) along the troidal surface is developed in Matsushita electric Industrial Co. A very good focusing with large flux gain more than 200 times as strong as primary intensity has been reported using Cu-$K\alpha$ radiation. The purpose of this study is to characterize the imaging and magnification of the neutron flux of this troidal PG crystal as a neutron condenser lens.

The troidal double bent pyloric graphite is made of polyimide sheets. The glassy carbon sheets obtained from the polyimide sheets annealed at 1000 ℃ can be easily bent along any two-dimensionally curved surface. After the forming an ideal troidal surface, the carbon sheet is annealed about 2800℃ under pressure in order to crystallize graphite, then heated at 3100 ℃ in argon atmosphere to improve the quality of the graphite crystal. This cylindrical PG has a large size typically 60 mm in diameter and 80 mm in length with 120 mm focal length.

The characterization study with neutron has been carried out using triple axis spectrometer TAS-2. The incident beam was monochromated at the wave length of 1.54 Å with a flat PG monochromator. The small sample rod was exposed , and the incoherent scattering from the sample was collimated and stored on a neutron image plate. A Cd disk was mounted on the optical axis to prevent the incoherent scattering from hitting directly onto the image plate. The forcus was roughly adjusted by minimizing the image size of a polyethylene disk with 3 mm diameter with changing the distances between sample tube, double troidal PG, and image plate. After that focusing was finely tuned with 1mm diameter paraffin tube. This sample was also used to check the imaging and the magnification of the neutron flux. The experimental set up is schematically shown in Fig. 1.

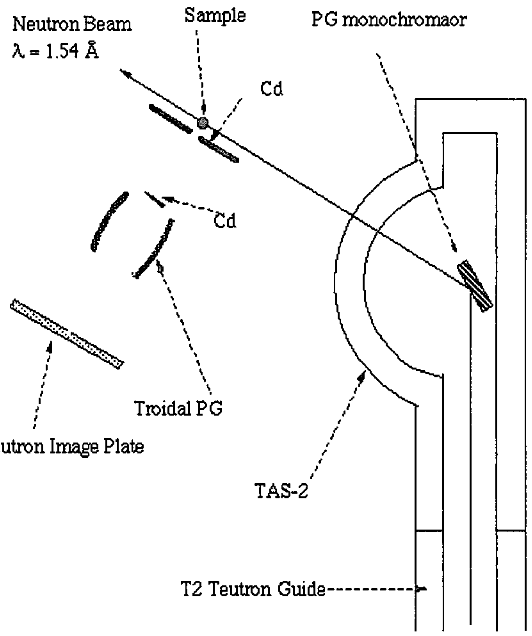

Fig. 1 The experimental set up for characterization of the troidal PG.

Figure 2 shows the profile of the image of polyethylene disk (3 mmϕ) as a function of the distance between the troidal PG and image plate. The linewidth of the profile changes with distance and shows a minimum at the focusing point. This result indicates that the neutron stored on the image plate is diffracted and collimated by troidal PG.

After determined the focusing point, the image from a paraffin tube has been stored. Figure 3 is the image of the sample. Surprisingly we obtained well collimated image on image plate which is 250 mm apart from the sample. Figure 4 shows the profile of the image. We found that the width of the profile was about 1.5 mm which is very sharp compare to the size of the sample, 1 mm in diameter. In addition we estimated magnification of the flux by comparing the intensity of the collimated beam and the background due to direct incoherent scattering. We found that the magnification would be 150, which is in our knowledge, the world record for the magnification of a neutron flux by reflective neutron optical device. Therefore we conclude that this double bent PG has an ideal troidal surface and it can be used as a condenser lens for high flux neutron beam. By improving the mosaic spread and the error of the curvature, we hope that the increase of the flux of the troidal PG, which is a powerful tool as a neutron device for imaging as well as focusing of neutron

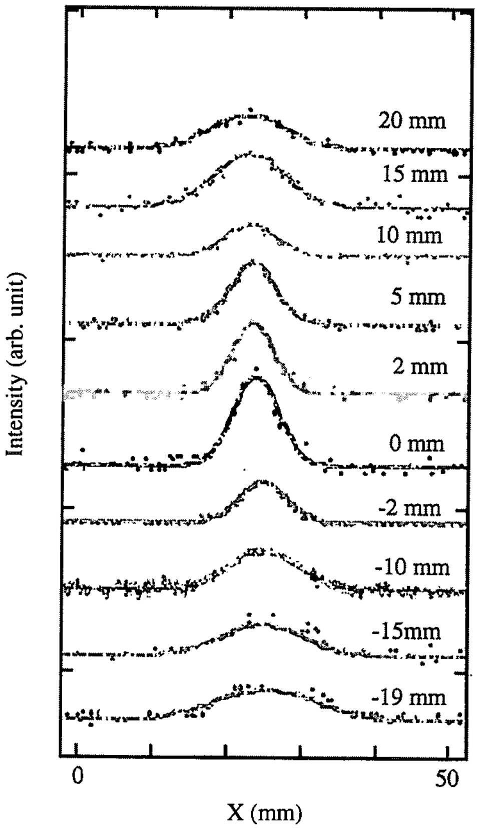

Fig. 2 The image profile of a polyethylene disk (3 mmϕ) as a function of the distance between the troidal PG and image plate.

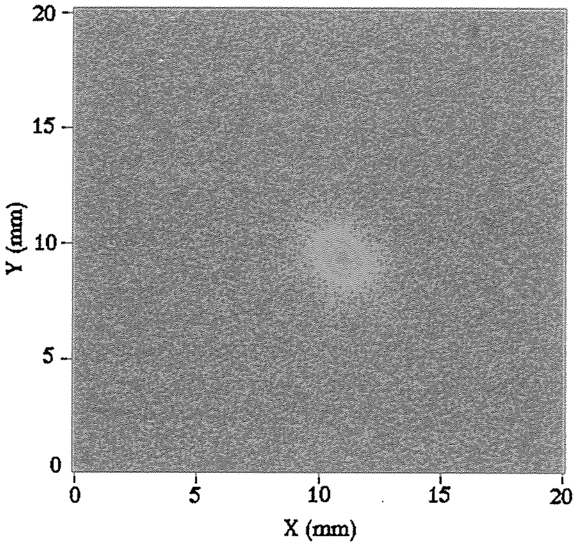

Fig. 3 The image of a paraffin tube with 1 mm diameter.

2.8.8 Reflectivity enhancement of Ni/Mn multilayer neutron mirrors by ion polishing in combination with sputter deposition

K.Soyama, W.Ishiyama[1] and K.Murakami[1]

Japan Atomic Energy Research Institute, Tokai, Naka, Ibaraki 319-11
[1] Nikon Corporation, Nishi-ohi, Shinagawa, Tokyo 140

A multilayer mirror with smaller *d*-spacing is desirable to lead greater angles of reflection for most applications. One of the most important problems in producing the small *d*-spacing multilayers is the reduction of the interface roughness which becomes larger with the number of bilayers deposited.

We have applied ion polishing in combination with ion beam sputtering deposition to smoothen the layer. We have carried out the investigation on Ni/Mn multilayers from the viewpoint of ion polishing time, ion acceleration energy and incident angle, in order to optimize the Ar^+ ion beam parameters.

Ni/Mn multilayers (d=100Å, N=10bilayer) with either Ni layers or Mn layers ion-polished were deposited. The ion polishing was applied immediately after the deposition of a layer to smoothen the layer. The condition of sputtering deposition were fixed for all multilayer mirrors, and conditions of the ion polishing were scanned. The reflectivity profiles were measured using C2-1 reflectometer. The incident neutron has a wavelength of 3.8 Å. Figure 1 shows specular reflectivity profiles of 1st Bragg peak of Ni/Mn multilayers ion-polished with various conditions. The maximum reflectivity of non-polished multilayer is 14.4%. On the other hand, that of multilayer with Ni layers ion-polished at a polishing time of 69 sec and that of multilayer with Mn layers ion-polished at a polishing time of 30 sec are respectively increased. The maximum reflectivity increased to 18.3% when both layers are ion-polished at a polishing time of 69 sec and 30 sec .

The interfacial roughness σ of multilayer was also evaluated with X-ray reflectivity measurement in a θ-2θ mode using Cu K_α radiation (λ=1.54Å). In case of ion-polishing Ni layers, σ value of 5.6Å decreases to a minimum value of 3.6Å by an ion polishing of 69 sec. On the other hand, a constant reduction of σ value of 4.5Å is observed over every polishing time in cases of ion-polishing Ti layers. The minimum σ value of 3.6Å is obtained when both layers were ion-polished at a polishing time of 69 sec and 30 sec.

It was observed that the neutron reflectivity and the interface roughness of multilayers are clearly improved.

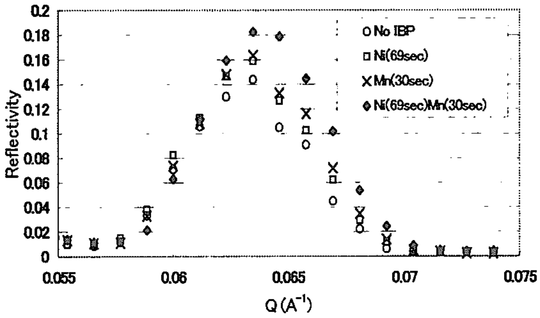

Fig.1 Reflectivity profiles of Ni/Mn multilayers with d=100Å and N=10bilayer for various ion polishing times.

Appendix A

Program Committee for Neutron Beam Utilization in JFY 1999 of the Advisory Council for JAERI'S Research Facilities

(Chairman)	Yasuhiko	Fujii	Professor, The Institute for Solid State Physics, The University of Tokyo
(Vice-Chairman)	Hisao	Kobayashi	Professor, Institute for Atomic Energy, Rikkyo University
	Kazuyoshi	Yamada	Professor, The Institute for Chemical Research, Kyoto University
	Susumu	Ikeda	Professor, National Laboratory for High Energy Physics
	Masafumi	Kohgi	Professor, Department of Physics, Tokyo Metropolitan University
	Takeji	Hashimoto	Professor, Graduate School of Engineering,Kyoto University
	Mamoru	Sato	Professor, Interdisciplinary Graduate School of Sciences, Yokohama City University
	Makoto	Hayashi	Department Manager, Mechanical Engineering Research Laboratory, Hitachi Ltd.
	Mitsuru	Ebihara	Assistant Professor, Faculty of Science, Tokyo Metropolitan University
	Yoichi	Sakai	Professor, Chemical Class, Daido Institute of Technology
	Nobuo	Niimura	Principal Scientist, Advanced Science Research Center
	Yasusada	Yamada	Invited Researcher, Advanced Science Research Center
	Naoto	Metoki	Senior Scientist, Advanced Science Research Center
	Yukio	Oyama	Head, Center for Neutron Science
	Shinshiyou	Kobayashi	General Manager, Office of Safety and Control
	Kazuo	Watanabe	Principal Scientist, Department of Environmental Sciences
	Hideo	Nakamura	Principal Scientist, Department of Reactor Safety Research
(Secretary)	Tadanori	Yamada	Deputy General Manager, Department of Research Reactor
	Yukio	Morii	Principal Scientist, Advanced Science Research Center
	Susumu	Katano	Principal Scientist, Advanced Science Research Center
(Observer)	Hiroshi	Maekawa	Head, Division of Collaborative Activities, Office of Planning
	Chushiro	Yonezawa	Senior Scientist, Department of Environmental Sciences
	Masahito	Matsubayashi	Research Scientist, Center for Neutron Science

Appendix B

Themes of Cooperative Research Projects with Universities in JFY 1999

1.	Study of Structural Phase Transition in Dielectric Compounds at Low Temperature	Y. Noda	Tohoku Univ.
2.	Magnetic Properties and Crystal Structures of Semi Magnetic Conductors	T. Kajitani	Tohoku Univ.
3.	Evaluation of Residual Stress and Fatigue Damage in Structural Materials	K. Tanaka	Nagoya Univ.
4.	Structural Disorder and the Dynamical Properties of Superionic Conductors	H. Takahashi	Ibaraki Univ.
5.	Study of Neutron Optics by Dynamical Effects	T. Takahashi	Tokyo Univ.
6.	Lattice Dynamics of Relaxor PZN	Y. Tsunoda	Waseda Univ.
7.	Development of a Temperature-Controller for Ultra-Small-Angle Scattering	Y. Izumi	Yamagata Univ.
8.	Magnetic Structure and Structural Transformation at Strong Magnetic Field in La-based Oxides Superconductors	T. Fukase	Tohoku Univ.
9.	Mechanism of slow Dynamics in Concentrated Spin-Glasses	K. Motoya	Science Univ. of Tokyo
10.	Structural Formation of Biological Polymer System under Magnetic Field	M. Hirai	Gunma Univ.
11.	Studies on Pattern Formation in Multicomponent Polymer Alloy	T. Hashimoto	Kyoto Univ.
12.	Exotic Magnetic Phases of Ce-compound-strongly-correlated-electron-systems	M. Kohgi	Tokyo Metropolitan Univ.
13.	Magnetic Structure of Rare Earth Dodecaborides	F. Iga	Hiroshima Univ.
14.	Magnetic Long Range Ordering in Haldane (1D,S=1) Systems under Magnetic Field	T. Kobayashi	Osaka Univ.
15.	Direct Observation of Vortex Lattice Structure and Corrlation between Magnetic order and Superconductivity in $Bi_2Sr_2CaCu_2O_{8-y}$	K. Kadowaki	Tsukuba Univ.

16.	Neutron Scattering Study of the "17.5 Transition" in URu_2Si_2	H. Amitsuka	Hokkaido Univ.
17.	Hydrogen Transfer in Photoisomerization of Cobaloxime Complexes	Y. Ohashi	Tokyo Inst.of Tech
18.	Neutron Diffraction Studies of Muscles	K. Wakabayashi	Osaka Univ.
19.	Magnetic Structure of Complex Oxides Containing f and d Electrons	Y. Hinatsu	Hokkaido Univ.
20.	Constraction of Air-Water Interaface Neutron Reflelctometer with Two-Dimensional Imaging Plate	H. Matsuoka	Kyoto Univ.
21.	Crystal Electric Field Excitation on Metallic Uranium Compounds	H. Aoki	Tohoku Univ.
22.	Magnetic Properties of the Ladder Compound $(Sr,Ca)_{14}Cu_{24}O_{41}$	J. Akimitsu	Aoyama Gakuin Univ.
23.	Structural Fluctuations and Transport Properties in Oxides Conductors	K. Kohn	Waseda Univ.
24.	Study on Helium-defect Clustering in Fusion Reactor Materials	T. Yamamoto	Tohoku Univ.

Appendix C

Themes of Cooperative Research Projects with Private Enterprises and National Laboratories in JFY 1999

1.	Modeling and Precise Experiments of Diffusion Phenomena in Melts under μg	T. Itami	NASDA
2.	Characterization of Ni-base Superalloy Single Crystal by Precise Neutron Optics	Y. Aono	Hitachi Ltd.
3.	Residual Stress Measurment by Neutron Diffraction	M. Hayashi	Hitachi Ltd.
4.	Magnetic Optics for Cold Neutron Beam	H. Shimizu	RIKEN
5.	Neutron Sacttering Experiments of $S=1$ Heisenberg Antiferromagnet	M. Hagiwara	RIKEN
6.	Study on the Relation Between Unusual Formation of High-ordered Protein Structures and Abnormal Apoptosis	S. Naito	L'ORÉAL Tsukuba Center
7.	Nano-level Analysis of Boron in Bio-systems Using Neutron Standing Waves	Y. Sasaki	Spring-8

Appendix D

Publication List in the Period of JFY 1999

1. Polar Structure of Lysozyme Aggregates in Unsaturated Solution Determined by Small Angle Neutron Scattering Contrast Variation Method
   N. Niimura, Y. Minezaki, I. Tanaka, S. Fujiwara and M. Ataka
   J. Crystal Growth **200** (1999) 265-270

2. The Classical Structure of $TaCp_2(H)(SiMe_2H)_2$
   I. Tanaka, T. Ohhara, N. Niimura, Y. Ohashi, Q. Jiang, D. H. Berry and R. Bau
   J. Chem. Research (S) **1999** 14-15
   J. Chem. Research (M) **1999** 0180-0192

3. An Elastically Bent Silicon Monochromator for a Neutron Diffractometer
   I. Tanaka, N. Niimura and P. Mikula
   J. Appl. Cryst **32** (1999) 525-529

4. Neutron Structural Biology
   N. Niimura
   J. Phys. Chem. Solids. **60** (1999) 1265-1271

5. Structural Study of HEW-lysozyme by Neutron Crystallography
   Y. Minezaki, T. Nonaka and N. Niimura
   J. Phys. Chem. Solids. **60** (1999) 1387-1391

6. An Upgradede Neutron Diffractometer (BIX-IM) for Macromolecules with a Neutron Imaging Plate
   I. Tanaka, K. Kurihara, Y. Haga, Y. Minezaki, S. Fujiwara, S. Kumazawa and N. Niimura
   J. Phys. Chem. Solids. **60** (1999) 1623-1626

7. Neutron Protein Crystallography: Hydrogen Hydration and Function of Tetragonal Hen Egg-White Lysozyme
   N. Niimura and Y. Minezaki
   In 'Perspectives in Structural Biology' A volume in honour of G N Ramachandran
   Edited by M Vijayan, N Yathindra, A S Kolaskar (1999) Indian Academy of Science 714-732

8. Neutrons Expand the Field of Structural Biology
   N. Niimura
   Curr. Opi. Struct. Bio. **9** (1999) 602-608

9. Gamma-ray Sensitivity and Shielding of a Neutron Imaging Plate
   Y. Haga, S. Kumazawa and N. Niimura
   J. Appl. Cryst. **32** (1999) 878-882

10. Mechanism of Deuterium - hydrogen Exchange in the Photoisomerization of Cobalt Complex

Y. Ohashi, T. Ohhara, J. Harada, I. Tanaka, S. Kumazawa and N. Niimura
J. Phys. Chem. Solids. **60** (1999) 1515-1517

11. The Optimization and Gamma-ray Effects of the Neutron Imaging Plate
    Y. K. Haga, S. Kumazawa and N. Niimura
    J. Phys. Chem. Solids **60** (1999) 1619-1621

12. The Structural Information on the DNA Binding Protein HU in Solution Obtained by the Small Angle Neutron Scattering Experiments
    S. Fujiwara and Y. Yonezawa
    J. Phys. Chem. Solids **60** 1393-1395 (1999).

13. Neutron Scattering Study of the Antiferromagnetic Ordering in UPt_3 at mK-temperatures
    Y. Koike, N. Metoki, N. Kimura, Y. Yamamoto, Y. Haga, Y. Onuki and K. Maezawa
    Physica B **259-261** (1999) 662-663

14. Pressure Effects on Spin-gap and Antiferromagnetism in the Hole-doped Spin Ladder System $Sr_{2.5}Ca_{11.5}Cu_{24}O_{41}$
    S. Katano, T. Nagata, Y. Fujino, J. Akimitsu, M. Nishi and K. Kakurai
    Physica B **259-261** (1999) 1046-1047

15. Neutron Scattering Study on Heavy Fermion Superconductors
    N. Metoki, Y. Koike, Y. Haga and Y. Onuki
    Physica B **259-261** (1999) 660-661

16. Magnetic Properties of $R_3Pd_{20}Ge_6$(R=Pr and Nd)
    N. Kimura, N. Tateiwa, M. Nakayama, H. Aoki, T. Komatsubara, T. Sakon, M. Motokawa, Y. Koike and N. Metoki
    Physica B **259-261** (1999) 338-339

17. New-Type 10T Split-Pair Superconducting Magnet for Neutron Scattering
    S. Katano, N. Minakawa, N. Metoki, T. Osakabe, J. Suzuki, K. Oikawa and Y. Matsuoka
    4th Int.Symposium on Advanced Physical Fields:Quantum Phenomena in Advanced Materials at High Magnetic Fields (1999) 315-318

18. Antiferromagnetic Ordering in the Spin Singlet State of the Ladder / Chain Material : $Sr_{2.5}Ca_{11.5}Cu_{24}O_{41}$
    T. Nagata, H. Fujino, J. Akimitsu, M. Nishi, K. Kakurai, S. Katano, M. Hiroi, M. Sera and N. Kobayashi
    J. Phys. Soc. Japan vol.68 **7** (1999) 2206-2209

19. Short-range Spin Order and Magnetic Excitations in Diluted Magnetic Semiconductor $Zn_{0.568}Mn_{0.432}Te$
    Y. Ono, S. Shamoto, K. Sato, T. Kamiya, T. Sato, Y. Oka, Y. Yamaguchi, K. Oyama, Y. Morii and T. Kajitani
    J. Phys. and Chemistry of Solids **60** (1999) 1253-1255

20. New Aspects of the b*-LA Phonon of $CuGeO_3$

M. Nishi, K. Kakurai, Y. Fujii, S. Katano, J. Akimitsu, M. Yethiraj and J. A. Fernandez-baca
J. Phys. and Chemistry of Solids **60** (1999) 1109-1111

21. Reinvestigation of the Structure of $(ND_4)_3D(SO_4)_2$ and $(NH_4)_3H(SO_4)_2$ at Room Temperature
I. Tamura, Y. Noda and Y. Morii
J. Phys. and Chemistry of Solids **60** (1999) 1411-1414

22. Remarkable Improvement of the Structural Data in h-$BaTiO_3$ with Short Wavelength Neutrons
Y. Noda, K. Akiyama, T. Shobu, Y. Morii, N. Minakawa and H. Yamaguchi
J. Phys. and Chemistry of Solids **60** (1999) 1415-1418

23. [110]TA_1 Phonon Dispersion Relation of the β_1-phase in Ni-Co-Al Alloys
M. Yamada, A. Nagasawa, Y. Ueno and Y. Morii
J. Phys. and Chemistry of Solids **60** (1999) 1427-1429

24. Coexistence of the Spin Liquid State and the Magnetic Ordering in the Spin Ladder Compound ; $Sr_{14-x}Ca_xCu_{24}O_{41}$
T. Nagata, H. Fujino, K. Ohishi, J. Akimitsu, S. Katano, M. Nishi and K. Kakurai
J. Phys. and Chemistry of Solids **60** (1999) 1039-1043

25. A Dilution Refrigerator using the Pulse Tube and GM Hybrid Cryocooler for Neutron Scattering
Y. Koike, Y. Morii, T. Igarashi, M. Kubota, Y. Hiresaki and K. Tanida
Cryogenics **39** (1999) 579-583

26. Crystal Structures and Magnetic Properties of $Ca_{2-x}Sr_xMnO_4$
K. Tezuka, M. Inamura, Y. Hinatsu, Y. Shimojo and Y. Morii
J. Solids State Chemistry **145** (1999) 705-710

27. Intrinsic Luminescence from Li_2O Crystals Excited in the Exciton-Band Region
M. Itoh, J. Murakami and Y. Ishii
p. stat. sol. (b) **213** (1999) 243-251

28. Neutron Scattering Experiments at High Pressure on a Heavy Fermion Superconductor UPd_2Al_3
T. Honma, Y. Haga, E. Yamamoto, N. Metoki, Y. Koike, T. Osakabe and Y. Onuki
(reprinted from) J. Phys. Soc. Japan vol.68 **12** (1999) 4047-4048

29. Diffuse Neutron Scattering from AgBr: Application to Rietveld Refinements
T. Sakuma, Y. Nakamura, M. Hirota, A. Murakami and Y. Ishii
Solid State Ionics **127** (2000) 295-300

This is a blank page.

国際単位系 (SI) と換算表

表1　SI基本単位および補助単位

量	名称	記号
長さ	メートル	m
質量	キログラム	kg
時間	秒	s
電流	アンペア	A
熱力学温度	ケルビン	K
物質量	モル	mol
光度	カンデラ	cd
平面角	ラジアン	rad
立体角	ステラジアン	sr

表2　SIと併用される単位

名称	記号
分, 時, 日	min, h, d
度, 分, 秒	°, ′, ″
リットル	l, L
トン	t
電子ボルト	eV
原子質量単位	u

$1\ eV=1.60218\times10^{-19}J$

$1\ u=1.66054\times10^{-27}kg$

表3　固有の名称をもつSI組立単位

量	名称	記号	他のSI単位による表現
周波数	ヘルツ	Hz	s^{-1}
力	ニュートン	N	$m\cdot kg/s^2$
圧力，応力	パスカル	Pa	N/m^2
エネルギー,仕事,熱量	ジュール	J	N·m
工率，放射束	ワット	W	J/s
電気量，電荷	クーロン	C	A·s
電位，電圧，起電力	ボルト	V	W/A
静電容量	ファラド	F	C/V
電気抵抗	オーム	Ω	V/A
コンダクタンス	ジーメンス	S	A/V
磁束	ウェーバ	Wb	V·s
磁束密度	テスラ	T	Wb/m^2
インダクタンス	ヘンリー	H	Wb/A
セルシウス温度	セルシウス度	℃	
光束	ルーメン	lm	cd·sr
照度	ルクス	lx	lm/m^2
放射能	ベクレル	Bq	s^{-1}
吸収線量	グレイ	Gy	J/kg
線量等量	シーベルト	Sv	J/kg

表4　SIと共に暫定的に維持される単位

名称	記号
オングストローム	Å
バーン	b
バール	bar
ガル	Gal
キュリー	Ci
レントゲン	R
ラド	rad
レム	rem

$1\ Å=0.1nm=10^{-10}m$

$1\ b=100fm^2=10^{-28}m^2$

$1\ bar=0.1MPa=10^5Pa$

$1\ Gal=1cm/s^2=10^{-2}m/s^2$

$1\ Ci=3.7\times10^{10}Bq$

$1\ R=2.58\times10^{-4}C/kg$

$1\ rad=1cGy=10^{-2}Gy$

$1\ rem=1cSv=10^{-2}Sv$

表5　SI接頭語

倍数	接頭語	記号
10^{18}	エクサ	E
10^{15}	ペタ	P
10^{12}	テラ	T
10^{9}	ギガ	G
10^{6}	メガ	M
10^{3}	キロ	k
10^{2}	ヘクト	h
10^{1}	デカ	da
10^{-1}	デシ	d
10^{-2}	センチ	c
10^{-3}	ミリ	m
10^{-6}	マイクロ	μ
10^{-9}	ナノ	n
10^{-12}	ピコ	p
10^{-15}	フェムト	f
10^{-18}	アト	a

（注）

1. 表1－5は「国際単位系」第5版，国際度量衡局 1985年刊行による。ただし，1 eV および1 uの値はCODATAの1986年推奨値によった。
2. 表4には海里，ノット，アール，ヘクタールも含まれているが日常の単位なのでここでは省略した。
3. bar は，JISでは流体の圧力を表わす場合に限り表2のカテゴリーに分類されている。
4. EC閣僚理事会指令では bar，barnおよび「血圧の単位」mmHgを表2のカテゴリーに入れている。

換　算　表

力	$N(=10^5dyn)$	kgf	lbf
	1	0.101972	0.224809
	9.80665	1	2.20462
	4.44822	0.453592	1

粘　度　$1\ Pa\cdot s(N\cdot s/m^2)=10\ P$(ポアズ)$(g/(cm\cdot s))$

動粘度　$1m^2/s=10^4St$(ストークス)(cm^2/s)

圧力	MPa(=10bar)	kgf/cm^2	atm	mmHg(Torr)	$lbf/in^2(psi)$
	1	10.1972	9.86923	7.50062×10^3	145.038
	0.0980665	1	0.967841	735.559	14.2233
	0.101325	1.03323	1	760	14.6959
	1.33322×10^{-4}	1.35951×10^{-3}	1.31579×10^{-3}	1	1.93368×10^{-2}
	6.89476×10^{-3}	7.03070×10^{-2}	6.80460×10^{-2}	51.7149	1

エネルギー・仕事・熱量	$J(=10^7\ erg)$	kgf·m	kW·h	cal(計量法)	Btu	ft·lbf	eV
	1	0.101972	2.77778×10^{-7}	0.238889	9.47813×10^{-4}	0.737562	6.24150×10^{18}
	9.80665	1	2.72407×10^{-6}	2.34270	9.29487×10^{-3}	7.23301	6.12082×10^{19}
	3.6×10^{6}	3.67098×10^{5}	1	8.59999×10^{5}	3412.13	2.65522×10^{6}	2.24694×10^{25}
	4.18605	0.426858	1.16279×10^{-6}	1	3.96759×10^{-3}	3.08747	2.61272×10^{19}
	1055.06	107.586	2.93072×10^{-4}	252.042	1	778.172	6.58515×10^{21}
	1.35582	0.138255	3.76616×10^{-7}	0.323890	1.28506×10^{-3}	1	8.46233×10^{18}
	1.60218×10^{-19}	1.63377×10^{-20}	4.45050×10^{-26}	3.82743×10^{-20}	1.51857×10^{-22}	1.18171×10^{-19}	1

1 cal= 4.18605J（計量法）

= 4.184J（熱化学）

= 4.1855J（15℃）

= 4.1868J（国際蒸気表

仕事率　1 PS(仏馬力)

= 75 kgf·m/s

= 735.499W

放射能	Bq	Ci
	1	2.70270×10^{-11}
	3.7×10^{10}	1

吸収線量	Gy	rad
	1	100
	0.01	1

照射線量	C/kg	R
	1	3876
	2.58×10^{-4}	1

線量当量	Sv	rem
	1	100
	0.01	1

(86年12月26日現在)